EXPERIMENTELLE PHYSIK

Performance of Online Tracklet Reconstruction with the ALICE TRD

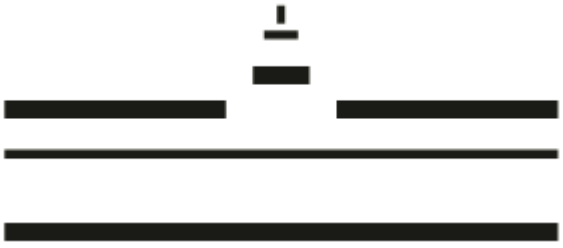

Westfälische Wilhelms-Universität Münster
Institut für Kernphysik

Diplomarbeit
von
Matthias Walter

– Februar 2010 –

Contents

1. Introduction

With an entire budget of about 3 billion euros the Large Hadron Collider (LHC) located at CERN[1] is one of the most expensive machines built for research. After the long shutdown since September 2008, due to a helium leak that caused the superconducting magnets to heat up to 100 °C, the largest particle accelerator of the world was successfully restarted in November 2009 and resumes its quest for the secrets of modern particle physics. In 2010 proton-proton collisions are at the top of the agenda, whereas at the end of this year first heavy ion collisions are planned. ALICE[2] is one experiment at the LHC which focuses on heavy ion collisions to learn more about the early universe. It concentrates on measuring a hot dense matter called 'Quark-Gluon-Plasma' (QGP) that is expected to have existed shortly after the Big Bang. This medium was already explored by other accelerators like SPS[3] at CERN or RHIC[4] at BNL[5]. They contributed to a much better understanding of the QGP matter but a decisive proof of it is still missing. With the considerably larger energies created by the LHC, the ALICE experiment is intended to confirm the results obtained so far and to provide new insights of the QGP.

ALICE is composed of a sub detector system that is optimized to measure physical observables by detection of photons, leptons and hadrons produced in the QGP phase. One detector of this system is the Transition Radiation Detector (TRD). Its purposes are both, particle identification and tracking. Because of the large amount of data in heavy ion collisions the produced information of the TRD is used to trigger other detectors in case of interesting events that include electrons or hadrons with high transverse momentum. In this thesis parts of the trigger performance of the ALICE TRD are explored by the investigation of online tracklet efficiency and resolution. The calculation of these track segments is the first step of the online tracking procedure inside the TRD.

After this introduction chapter 2 summarizes theoretical basics of particle physics as of today. Among these are the Standard Model of elementary particles and the production of a QGP medium. Chapter 3 describes the setup of the LHC and the ALICE experiment. In chapter 4 the functionality of the Transition Radiation Detector is described in detail. An introduction to the online tracking procedure, which is the basis of the subsequent analysis, is depicted in chapter 5. In this context a short overview of the cosmic test setup used for data taking is shown. Chapter 6 deals with efficiency measurements. In this chapter a method is developed to determine the efficiency of online tracklets using cosmic rays. The efficiency is then optimized for different parameter settings of the electronics. In chapter 7 the position resolution of online tracklets in the direction of the transverse momentum is investigated. In doing so, different methods are used which are based on cosmic ray data as well as Monte Carlo simulations. Chapter 8 depicts angular resolution measurements of online tracklets which are obtained by a comparison to Monte Carlo

[1] European Organization for Nuclear Research
[2] A Large Ion Collider Experiment
[3] Super Proton Synchrotron
[4] Relativistic Heavy Ion Collider
[5] Brookhaven National Laboratory

tracks. At the end of this chapter tail cancellation is discussed to improve the resolution. Finally, a short summary of the results is presented in chapter 9.

2. Theoretical Background

2.1 The Search for Elementary Particles

For a long time scientists have been searching for the fundamental building blocks of matter. As early as 400 BC the concept of 'atomos'[1] was introduced, but it took centuries to find elementary particles experimentally. A large part of this work has been done in the first half of the 20th century, starting with several outstanding ideas of Albert Einstein about the relativity principle, the particle wave dualism, and a famous suggestion equalizing energy and mass.

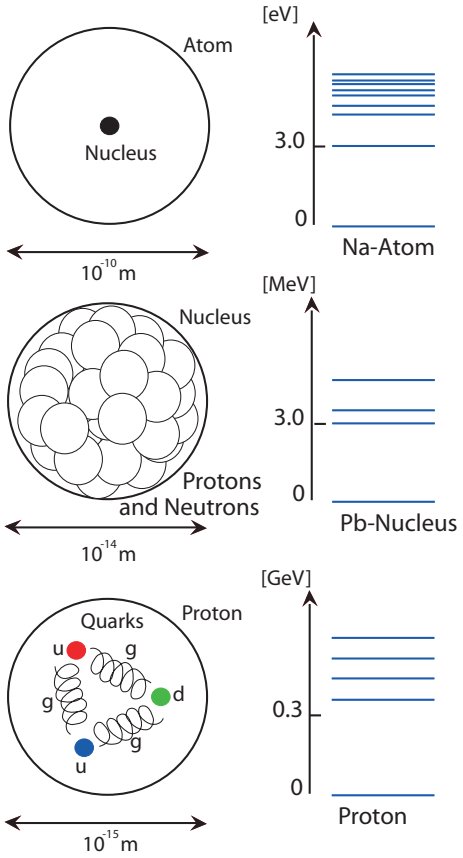

Figure 2.1: *Hierarchical structures, length scales, and typical excitation energies of the atom and its constituents [P+09].*

The first elementary particle was found in 1898, when Sir Joseph John Thompson measured the electron and proposed his 'plum pudding' model of an atom. This implies an equal distribution of electrons and – for neutrality reasons – positively charged particles inside the atom. In 1911 Ernest Rutherford deduced from scattering experiments of α radiation on a gold foil that the positive part of an atom, now called nucleus, takes only a little fraction of the whole volume but most of its mass. In 1919 and 1931 the constituents of the nucleus, proton and neutron, were discovered by Rutherford and James Chadwick, respectively. As the positive charge of a proton should lead to a repulsive effect in the nucleus, the necessity emerged to introduce another, stronger attractive force that holds the nucleons together. This was done by Hideki Yukawa who described the nuclear force for the first time[2] [P+09].

Another elementary particle called neutrino was postulated in 1930 by Pauli to satisfy both, energy and momentum conservation in the β decay. Due to its small interaction probability a proof of the existence was very challenging, but eventually accomplished by Clyde L. Cowan and Frederick Reines in 1956 via the inverse β decay [P+09].

[1] Atomos ($\alpha\tau o\mu o\varsigma$) is Greek and means individable.
[2] The nuclear force is a residual interaction of the strong force and mediated by a pion.

With the development of particle accelerators in the second half of the 20^{th} century it was possible to study nuclear matter more precisely which resulted in ever increasing numbers of new 'elementary' particles. These were sorted by their fundamental origin (see section 2.2). In 1967 the **S**tandford **L**inear **A**cceleration **C**enter (SLAC) started an agenda to explore the nature of the proton. In inelastic scattering processes of electrons (about 5 GeV) on a fixed proton target the invariant mass spectra showed in addition to the elastic scattering peak new resonances which were attributed to excited states of the nucleons. This implied that nucleons have a substructure of particles, later called quarks [WW06]. The structure function of nucleons and properties of quarks were studied in deep inelastic scattering experiments by Friedmann, Kendall and Taylor (nobel price 1990) [nob10]. These experiments have shown that quarks are point-like spin 1/2 particles. Today quarks are still considered elementary particles. Lots of particles containing quarks have been produced in various experiments and classified by an own particle group called hadrons. As they occur in an extremely rich amount they are often called a 'hadron Zoo' with the most prominent representatives being proton and neutron.

Quarks have interesting properties that are under investigation until today. One striking aspect is their so-called confinement – a phenomenon that forces a group of 2 or 3 quarks to be bound inside a hadron. Properties of quarks are described in the following section.

2.2 Standard Model of Elementary Particles

The **S**tandard **M**odel of particles (SM) summarizes all known elementary particles, their interactions, and the associated theories. The SM contains 12 fermions[3] which are arranged in a family structure and the gauge bosons[4]: photon, $W^{\pm}$-bosons, Z^0-boson, and gluons. The fermions can be subdivided into leptons of three families: $\begin{pmatrix} e^- \\ \nu_e \end{pmatrix}$, $\begin{pmatrix} \mu^- \\ \nu_\mu \end{pmatrix}$, $\begin{pmatrix} \tau^- \\ \nu_\tau \end{pmatrix}$ and quarks which occur in the 'flavors': $\begin{pmatrix} u \\ d \end{pmatrix}$, $\begin{pmatrix} c \\ s \end{pmatrix}$, $\begin{pmatrix} t \\ b \end{pmatrix}$. The bosons are deduced from gauge field theories and act as mediators of the 3 fundamental forces. Table 2.1 summarizes all known elementary particles.

The Electromagnetic Force

Quantum **E**lectro**D**ynamics (QED) is the most precisely reviewed theory and predominantly known from investigation on atomic length and energy scales. The coupling constant is given by the fine structure constant $\alpha_e = \alpha = 1/137$ and the interaction is described by the maxwell equations. The photon takes the role of the mediating boson. As it is massless and does not carry electric charge, the field shows long-range behavior. Each particle mentioned above is subject to the electromagnetic force, except for neutrinos, gluons, and Z^0.

[3] Each particle has a dedicated anti-particle which arises from Quantum Field Theory to maintain the symmetry. For example, the assigned anti-particle of the electron e^- is the positron e^+ carrying the opposite charge but the same mass.

[4] The graviton which is expected to mediate the gravitation is not embedded in the SM. Its existence has not been proved till today. Since the gravitation is very weak on atomic length scales, its influence can be neglected in the further discussion.

	Particle	Name	Interaction	Charge (e)	Mass (MeV/c^2)
leptons	e^-	electron	e.m., weak	-e	0.511
	μ^-	muon		-e	105
	τ^-	tau		-e	1777
	ν_e	electron neutrino	weak	0	$< 0.2 \cdot 10^{-6}$
	ν_μ	muon neutrino		0	< 0.19
	ν_τ	tau neutrino		0	< 18.2
quarks	u	up-quark	e.m., weak, strong	+2/3 e	1.5 - 4
	d	down-quark		-1/3 e	4 - 8
	c	charm-quark		+2/3 e	≈ 1800
	s	strange-quark		-1/3 e	80 - 130
	t	top-quark		+2/3 e	≈ 175000
	b	bottom-quark		-1/3 e	≈ 4500
bosons	γ	photon	e.m.	0	0
	$W^{+/-}$	charged W-boson	weak	+/- e	80403 ± 29
	Z^0	neutral Z-boson		0	91188 ± 2
	g	gluons	strong	0	0

Table 2.1: *Elementary particles of the Standard Model [A$^+$08b], [Ams07]. For bosons the column 'Interaction' indicates the force which is mediated and not the one they underlie. Actually, the massless gluons interact with a strong color field. Confinement is then a consequence of the property of gluons to interact with each other.*

The Weak Force

The weak force applies to interactions that involve neutrinos as e.g. the β decay, but also scenarios like a neutral current in which the Z^0 boson is exchanged between two electrons are possible. The strength of the interaction is small as its name implies[5]. This results from the large masses of the mediating bosons W^-, Z^0 and W^+. Based on the similarity to the electromagnetic force, a unifying electroweak interaction was introduced in which γ and Z^0 are two orthogonal states created by mixing the singlet and triplet states of the weak isospin by rotation of the Weinberg angle [P$^+$09]. Nowadays, one special task of the great collider experiments is to detect the Higgs boson which has theoretically been predicted to assign mass to particles. This discovery could possibly explain the enormous mass of the neutral Z^0 boson.

The Strong Force

The strong force is responsible for interactions between quarks by mediating gluons. It is described by the theory of **Q**uantum **C**hromo**D**ynamics QCD. In addition to the fractional electromagnetic charges, all quarks carry a strong charge which comes in three different

[5]The coupling constant $\alpha_w \approx \frac{q^2}{m_w^2 c^2} \cdot \alpha << \alpha$ is inversely proportional to the mass of the heavy bosons [Ams07].

values. QCD describes the formalism of these so-called color charges as red, blue and green[6].

The potential of the strong force as a function of the distance r can be expressed by [WW07]:

$$V(r) = \frac{-4\alpha_s}{3r} + kr \tag{2.1}$$

where α_s denotes the strong coupling constant [P+09]:

$$\alpha_s(Q^2) = \frac{12\pi}{(32 - 2n_f) \cdot \ln\frac{Q^2}{\Lambda^2}} \tag{2.2}$$

In this formula n_f stands for the degrees of freedom of quarks and Λ is a scale parameter which can be determined in lattice QCD ($\Lambda \approx 250$ to 300 $\left(\frac{\text{MeV}}{c}\right)^2$). Unlike the electromagnetic case the strong coupling constant substantially depends on the momentum transfer Q^2. As displayed in equation 2.2 the coupling constant decreases with increasing momentum transfer. This phenomenon is called asymptotic freedom. Considering a momentum transfer of 100 GeV/c, α_s yields a value of about 0.12 which exceeds the fine structure constant by two orders of magnitude. At small distances the potential is associated with an exchange of one gluon and therefore coulomb like. At larger distances the linear term of equation 2.1 dictates the potential, which implies a stronger coupling and results in the phenomenon of confinement. As a consequence quarks do not appear isolated in nature but always combine to bound states of hadrons. These are named mesons, composed of quark and anti-quark, and baryons, made of three quarks. By combination of the different quark flavors and considering the excited states, a rich amount of baryons and mesons can be created[7]. Many of them have been found experimentally.

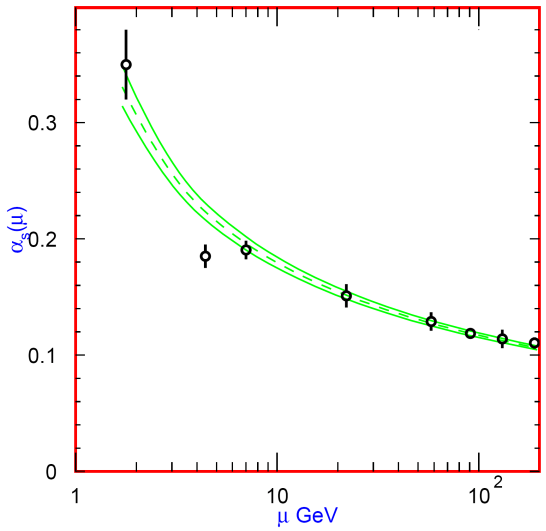

Figure 2.2: *The strong coupling constant as a function of the momentum transfer [alp10].*

To approach the properties of the strong force theoretically two common possibilities are perturbation theory and lattice QCD. The perturbation approach delivers reasonable results with the requirement of a small coupling constant α_s. Thus, physics of small distances and high momentum transfer are included. However, perturbation theory fails for small momentum transfers ($\alpha_s \geq 0.3$ at ≈ 2 GeV, see figure 2.2) as the higher order corrections can no longer be neglected. In recent years QCD on the lattice has become a

[6] The color charges of quarks that are bound in a hadron have to add up to a white color due to confinement. The white color is obtained either by red+blue+green (baryons) or by color plus anti-color (mesons).

[7] e.g. the proton is a baryon made of u, u, d and the pion π^+ is a meson composed of u and $\bar{\text{d}}$.

powerful tool since it allows to calculate important observables on a time-space discretized lattice numerically. With this feature it is possible to cover and investigate the properties of confinement and chiral symmetry breaking being of great importance in this context.

Chiral symmetry breaking is another interesting part of QCD. Generally spoken, it implies that quarks confined in hadrons do not appear as nearly massless constituents. In the theoretical part the Lagrangian that describes the part of the quarks is invariant under group transformation concerning the chiral symmetry with the assumption of zero quark masses. Actually, quarks confined in hadrons of ordinary matter carry mass[8], thus the symmetry is broken [HM96].

2.3 The Quark-Gluon-Plasma

The density of ordinary nuclear matter can be approximated by [SPR90]:

$$\rho_0 = 0.14 \frac{\text{nucleons}}{\text{fm}^3} \tag{2.3}$$

which leads to the following energy density:

$$\epsilon \approx 130 \frac{\text{MeV}}{\text{fm}^3} \tag{2.4}$$

Increasing either the temperature or the density, QCD predicts that hadrons undergo a phase transition at certain critical values to a new state of matter called **Q**uark **G**luon **P**lasma (QGP). In this state quarks are deconfined. Additionally, the chiral symmetry is expected to be restored. The degrees of freedom intimately connected to this system are no longer the quantum numbers of the hadrons but those of the deconfined quarks. Measured particle yields and ratios lead to the conclusion that equilibrium is reached in the early time of the collision ($t_0 < 1$ fm/c) [YHM05]. Therefore, well defined observables like temperature, energy, pressure, or entropy allow to treat the system as an ideal gas or fluid [BMS07].

In the simplest approach the system can be described with two free parameters: temperature and baryon chemical potential. The latter quantity implies the energetic costs to add one more baryon or anti-baryon to the system. In the case of an equal amount of baryons and anti-baryons ($\mu_B = 0$) it is easy to add one more baryon. If the baryon number is much higher than that of anti-baryons large energetic efforts have to be made to add a further baryon to the system and vice versa.

Figure 2.3 schematically shows what a phase transition could look like by plotting the temperature against the baryon chemical potential μ_B. The blue dot shows the classification of nuclear matter in this context. The curve separates the hadron gas phase and the expected QGP. In the limit of low net baryon densities (equal amounts of quarks and anti-quarks) the phase transition is expected to be the same as in the early universe. The value for the transition temperature predicted by QCD is around 173 ± 10 MeV [BMS07]. This especially is the limit in which the LHC contributes its measurements since in high energetic particle collisions quarks and anti-quarks are produced almost equally. According to the standard cosmological model the temperature of the universe amounts to 200 MeV

[8] e.g. the constituents of a proton (u and d quarks) carry a mass of ≈ 300 MeV.

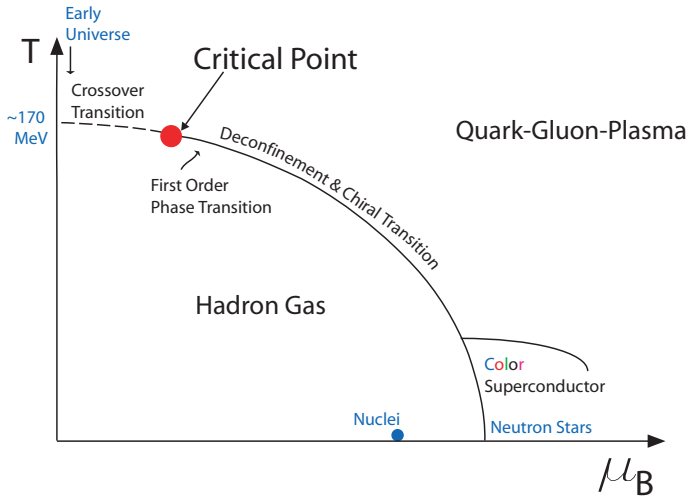

Figure 2.3: *The phase diagram shows the relation between temperature T and baryon chemical potential μ_B [rhi09].*

at a time of 10^{-6} seconds after the Big Bang. Hence, while studying the properties of the QGP crucial information about the early universe can be obtained [HM96].

Another possibility to reach high energy densities is at intermediate beam energies. In this case the incoming protons are stopped and thus contribute to large baryon densities. This area will be explored by the **C**ompressed **B**aryonic **M**atter experiment (CBM) at the **F**acility for **A**ntiproton and **I**on **R**esearch accelerator (FAIR) in Darmstadt. Among other physics goals, CBM is intended to search for the critical end point as its existence and exact location is not known. In this context CBM will study for example non statistical fluctuations of particle yields [S+06].

Looking at the confinement curve, the dashed line indicates a smooth cross-over from hadronic matter to the plasma at low net baryon densities, whereas the solid line describes a first-order phase transition at higher baryon net densities. In a first-order phase transition the order parameter changes discontinuously at the transition temperature and therefore some latent heat is produced. The two lines intersect in a critical end point. In addition, a scenario like a Color Superconductor has to be taken into account at large densities and small temperatures which is comparable to the electromagnetic case. This region is currently not accessible in the laboratory, but may be present in neutron stars. During the transition to a phase of Color Superconductivity it is expected that quarks leave the 'Fermi-liquid' to form correlated cooper pairs which now have bosonical properties. This transition is accompanied by a symmetry breaking in the underlying theory [rhi09].

2.4 QGP in the Laboratory

The only possibility to create hot dense matter in the laboratory is to collide two heavy nuclei with relativistic energies. Depending on the size of the created system different properties of the medium can be studied. In recent years larger and larger accelerator complexes were built to enhance the energy of the colliding particles. Since higher energies contribute to larger volumes of the dense medium and a longer existence of the QGP phase, properties of the QGP were investigated increasingly throughout the past 30 years. Starting in 1985, two accelerators that prepared protons and light ions for fixed target experiments contributed to the future development of heavy ion collisions. These are the **S**uper **P**roton **S**ynchrotron (SPS) at CERN which provided particles of about $\sqrt{s_{NN}} = 20$ GeV using oxygen or sulfur as a target and the **A**lternating **G**radient **S**ynchrotron (AGS) at the **B**rookhaven **N**ational **L**aboratory (BNL) with a center of mass energy per nucleon of $\sqrt{s_{NN}} = 5$ GeV using silicone as a target. In the early 90's these experiments used heavier ions (gold or lead) and gave first insights in the QGP matter about collective behavior as well as thermal and chemical equilibrium. Further on, important signatures like J/Ψ suppression or direct photons were explored [YHM05]. Nowadays, the examination of the QGP takes place at large collider experiments to make use of the full center of mass energy. In 2000 the **R**elativistic **H**eavy **I**on **C**ollider (RHIC) at BNL was put into operation. The main types of particle combinations used at RHIC are proton-proton, deuteron-gold, copper-copper and gold-gold with a typical center of mass energy of $\sqrt{s_{NN}} = 200$ GeV (for Au+Au). At this accelerator the quenching and correlation of particle jets was studied carefully. Moreover, the elliptic flow could be measured precisely [YHM05]. In 2009 the **L**arge **H**adron **C**ollider (LHC) at CERN that provides energies up to 14 (5.5) TeV in p-p (Pb-Pb) started its research. The LHC enhances the number of rare events including charm and bottom quarks so that an expected suppression of the Υ particle can be measured for the first time. The signatures of the QGP mentioned in this section are explained more precisely in section 2.5.

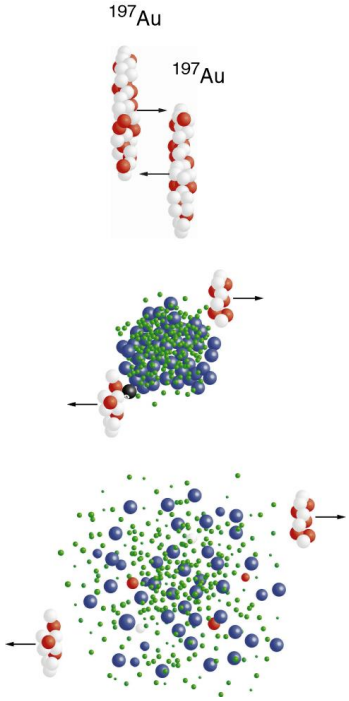

Figure 2.4: *Evolution in a heavy ion collision. Top: two gold nuclei are shot on one another. Middle: the nucleons that participate in the interaction (participants) produce partons (green and blue). Spectators fly along without taking part. The number of participants and spectators determines the centrality of the collision. Bottom: the fireball reaches hadronization and new hadrons are created [rhi09].*

Figure 2.4 shows the collision of two gold nuclei. In the top of figure 2.4 these two Lorentz contracted nuclei are moving nearly with the speed of light. In the primary collisions the hard partons are created. Re-scattering processes of the quarks and gluons lead to thermalization ($t_0 < 1$ fm/c): at this point, if the energy density is high enough, a QGP can be formed. In other words: because of the high energy densities of the order of 1 GeV/fm^3 (compare to ordinary matter) the wave functions of the generated hadrons will overlap so that they become indistinguishable particles. The quarks are now regarded as quasi free and and can be described by the QGP after thermalization. The fireball quickly builds up a very large pressure gradient which leads to the expansion of the system. Consequently collective behavior of particles can be observed (for example elliptic flow).

After a certain time the system reaches a critical temperature and undergoes a phase transition in which hadrons are formed again. This is called hadronization. By the time inelastic scattering processes are extinguished the so-called chemical freeze-out happens. From now on the composition of hadrons is determined. The thermal freeze-out leaves the cold hadron gas behind and is finally reached when no elastic scattering occurs anymore. After this freeze-out the particle spectra of momentum will not change. The particles which experienced the evolution of the QGP carry crucial information about this delicate state.

2.5 Signatures of the QGP

In order to manifest the existence of the QGP, it is intended rather to look for several indicators than for one decisive proof. Therefore, quite a few signatures linked to this medium are under current investigation. The most crucial ones are depicted in the following.

Jet Quenching

Hard parton-parton scattering processes take place in the initial phase, prior to the formation of the QGP. Thereof produced (richly) energetic quarks and gluons can fragment into particle jets of hadrons emitted in a narrow cone. Mathematically they are described by fragmentation functions that include the probability for a parton to fragment into a hadron. This hadron then carries a fraction of the parton's energy.

As the jet has to traverse the QGP medium, which consists of dense and strongly interacting matter, it is plausible that it looses energy. Some jets may loose so much energy that they cannot be detected anymore. This phenomenon is termed jet quenching. Moreover, jet correlation in a two jet event emitted back to back can be explored. First, a trigger particle with a certain p_t threshold defines an angle of 0°. Thereafter, a search for correlated particles related to this angle takes place. Based on the Jet Quenching model the correlation should be weak in central collisions. This was shown in [A$^+$03] with central Au+Au at RHIC.

J/Ψ Suppression and Enhancement

The J/Ψ particle is the triplet ground state of charmonium, a meson that consists of charm and anti-charm (c,$\bar{\text{c}}$) with a rest mass of 3.0969 GeV/c^2. The J/Ψ as well as the first excited state Ψ' are narrow states with a relatively long lifetime of $\tau \approx 7.2 \cdot 10^{-21}$ s. The

reason for this is that the decay into D-Mesons[9] is not possible since the exciting energy is not sufficient to create them. So for the decay the c-quark has to change flavor which results in a long lifetime. However, the higher excited states like $\Psi(4040)$ have enough energy to form new D-mesons. That is why they are called broad states [Bar06]. In context of the QGP, particle yields in the electron and muon decay channel of the J/Ψ are explored and compared to p-p collisions. In case a QGP is created, an analog effect to debye screening[10] in the strongly interacting matter prevents the $(c,\bar{c})$-pair to form charmonium so that after freeze out, the c-quarks preferentially combine with lighter quarks as these are much more abundant [HM96]. Therefore, a J/Ψ suppression is expected in heavy ion collisions[11]. At LHC the cross section to produce $(c,\bar{c})$-pairs is ten times larger than at RHIC. Thus, it is expected that at LHC this production superimposes the suppression so that finally a J/Ψ enhancement can be observed. The particle yields at LHC for bottonium $(b,\bar{b})$ with its three narrow states Υ, Υ', and Υ'' is even 100 times larger than at RHIC. Due to the sufficient particle yields at the LHC a suppression of Υ can be studied for the first time [RS09].

Elliptic Flow

The elliptic flow is a signature of the QGP from the soft physics part. It is based on the assumption of collective behavior while treating the QGP medium as an ideal fluid. In a peripheral collision the region of participants forming the QGP is outlined in figure 2.5. Due to this anisotropic geometry, different pressure gradients are created. Therefore, the evolution of the fireball is anisotropic, too. The stronger pressure gradients pointing in horizontal direction contribute to a larger momentum along this axis. The elliptic flow v_2 was measured at AGS, SPS and RHIC to examine its dependence on the centrality and the eccentricity of the initial almond shape [YHM05].

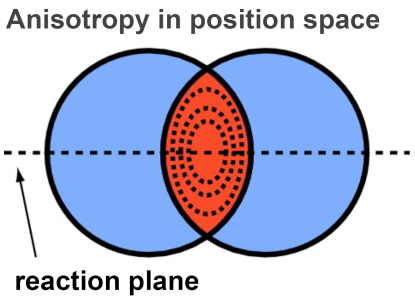

Figure 2.5: *Anisotropy in a peripheral collision. The red area marks the overlapping region in the interaction plane. The anisotropy in position space contributes to an anisotropy in momentum space [RS09].*

Direct Photons

Direct photons are produced throughout the stages of the reaction and thus carry crucial information about all phases. In general prompt and thermal photons are distinguished.

The prompt photons originate from hard scattering processes like the quark-Compton scattering. The special about photons is that they are only subject to the electromagnetic force (see section 2.2). Therefore, they can travel through the dense and strongly

[9] Mesons that consist of a charm quark and a light quark.

[10] Debye screening originally comes from electrodynamics. In this context screening is the damping of electric fields by the presence of mobile charge carriers.

[11] SPS already found this suppression [YHM05].

interacting matter without much deterioration. In contrast to jets, the quenching effect should not occur in this case. One special purpose of the PHOS detector in the ALICE experiment described in section 3.3 is to measure the prompt photons. These have to be separated from the rich photon background from π^0 decays.

The thermal photons are emitted, analogous to black body radiation, by the QGP in equilibrium. The detection of these photons is quite sophisticated due to several other sources of decay photons that lead to an enormous background [RS09].

Degrees of Freedom

As outlined in section 2.3 the degrees of freedom in the QGP phase are those of the deconfined quarks. This number is much larger than in the hadron gas phase. Figure 2.6 illustrates the increase of the degrees of freedom at the critical temperature for different kinds of flavor based on QCD calculations. The energy density is divided by the temperature to the fourth due to the Stefan-Boltzmann law in order to obtain the exclusive dependence on the degrees of freedom. While SPS energies are near the border of the phase transition, at RHIC and LHC the formation of a QGP should be ensured. As stated before the transition temperature is around 170 MeV to 180 MeV.

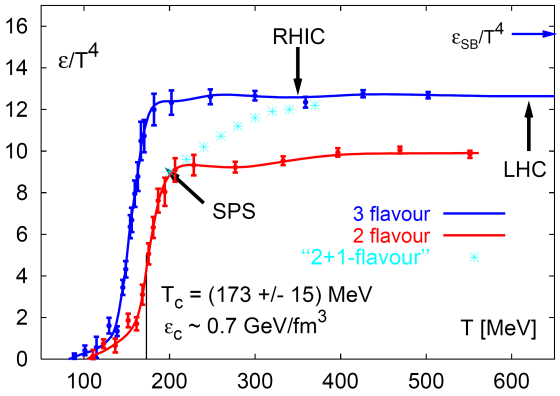

Figure 2.6: *The diagram shows the abrupt increase of the degrees of freedom during the phase transition to the QGP [KL03].*

3. The Experiment

3.1 The Large Hadron Collider

As far back as in the early 80's while the **L**arge **E**lectron **P**ositron Collider (LEP) was designed and built at CERN, the idea was born to use such a large accelerator for heavy ion and proton-proton collisions, too. This idea finally became true when in 1994 the CERN Council accepted the request to construct one of the bravest projects in science – **The Large Hadron Collider (LHC)**.

The LHC comprises a ring of 27 km circumference, between Lake Geneva and the Jura mountains, installed in a tunnel at an average depth of 100 meter underground beneath the Franco-Swiss border near Geneva. This machine is supposed to collide two beams injected in opposite directions, of either protons or lead ions in the heavy ion mode, with a top energy of 7 TeV and 574 TeV respectively, at four intersection points where the four large experiments ATLAS, CMS, ALICE and LHCb are located [cer09].

As the particles are accelerated to nearly the speed of light a strong counterpart has to compensate the centrifugal force to put and keep them on their circular path. Therefore, the collider ring is equipped with a total of 9593 magnets that include dipoles, quadruples, sextupoles, octupoles and decapoles. The 1232 dipole magnets are the most significant but at the same time the limiting constituent parts of the magnet system since they have to create large magnetic fields. Their main duty is to keep the particles on their trajectory. The 392 quadrupole magnets are used to focus the beam. Additionally, 8 RF (Radio Frequency) cavities per beam guarantee the tight coherence of the 2808 proton bunches per beam to reach the luminosity design value of 10^{34} $cm^{-2}s^{-1}$. This yields about 600 million collisions per second, where a single proton bunch contains about $1.1 \cdot 10^{11}$ particles. The cavities provide an accelerating field of 5 MV/m at 400 MHz.

An efficient vacuum system is absolutely necessary, at first for the beam not to have any unintentional interactions between the injected particles and some air contamination, moreover for the insulation of the helium line. Pumping the super fluid helium into the magnet systems allows to operate at a temperature of 1.9 K (-271.25 °C) to exploit the properties of superconductivity. Consequently, the dipole magnets can use high currents to produce a large magnetic field of 8.3 T. The cavities can use the helium insulation, too as they run with a temperature of 4.5 K (-268.7 °C) [lhc09].

The LHC is just the last part of a complex system of pre-accelerators which are fed either with protons or lead ions to increase their energy and transfer them to the next larger accelerator. A setup of the LHC ring that includes its pre-accelerators and the location of the four experiments is given in figure 3.1. The procedure for both, protons and lead ions, is to be inserted in the **P**roton **S**ynchrotron (PS), then to be transferred to the **S**uper **P**roton **S**ynchrotron (SPS), and finally to be injected clockwise and counterclockwise in the LHC. A summary of the injection energies is given in table 3.1.

After the protons are produced by stripping the electrons from hydrogen atoms, they are transferred from Linac2 at an energy of 50 MeV to the PS Booster where they are accelerated to an energy of 1.4 GeV and finally reach the PS. The production of lead ions is

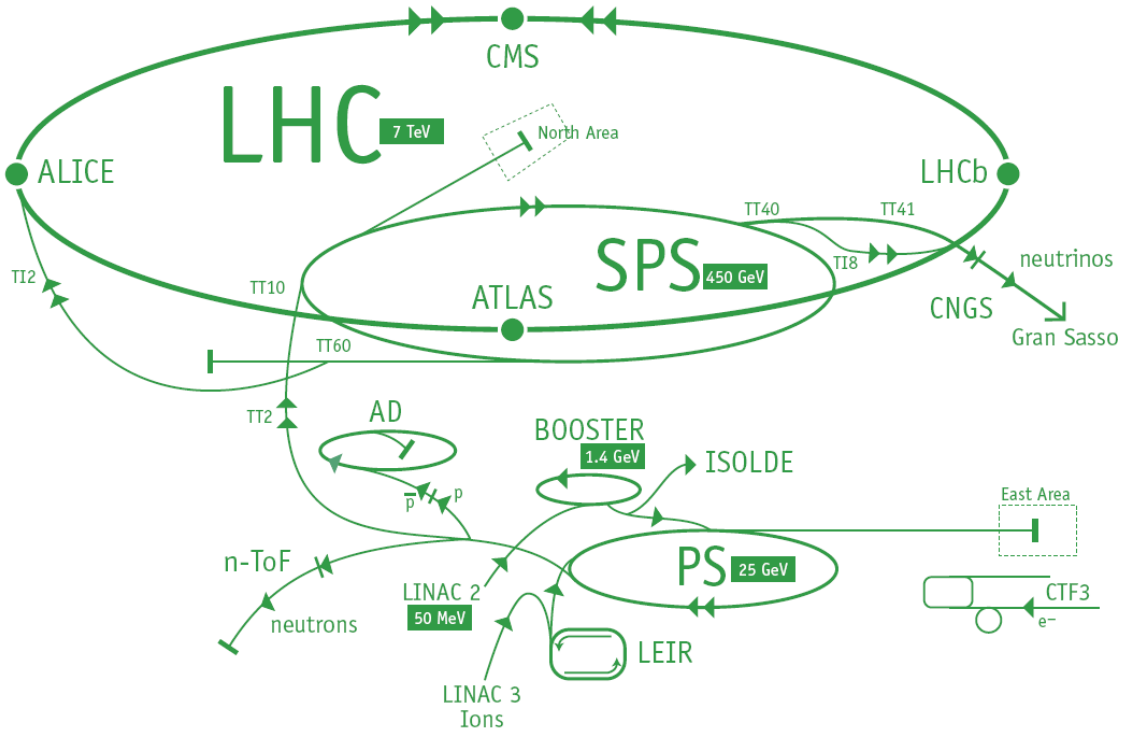

Figure 3.1: *LHC and pre-accelerator system [lhc09].*

	Injection Energy	
Machine	Protons	Lead Ions
PS	1.4 GeV	72 MeV/u
SPS	25 GeV	5.9 GeV/u
LHC	450 GeV	177 GeV/u

Table 3.1: *Injection energies of the accelerator system feeding the LHC [lhc09].*

somewhat more complicated. They are obtained by heating a purified lead sample. After the Pb^{29+}-ions have been stripped twice, selected and pre-accelerated to 5.9 GeV/u in the **L**ow **E**nergy **I**on **R**ing (LEIR), Pb^{54+}-ions are sent to the PS. A last stripping happens after the injection into the SPS where fully ionized Pb^{82+} is obtained [lhc09].

The LHC is intended to research curiosities of modern particle physics, among others to test the theories beyond the SM. One of the main goals is to discover the Higgs boson, but also the search for supersymmetric particles for a grand unifying theory, the exploration of dark matter, and with respect to this thesis the investigation of the QGP. With a total energy available of 14 TeV for protons and 1150 TeV for lead ions (CMS) this gigantic accelerator offers the possibility to study the primordial soup which is expected to have existed shortly after the Big Bang. A summary of important facts concerning the capabilities of the LHC is given in table 3.2.

Quantity	Number
Circumference	26 659 m
Dipole operating temperature	1.9 K (-271.3 °C)
Number of magnets	9593
Number of main dipoles	1232
Number of main quadrupoles	392
Number of RF cavities	8 per beam
Nominal energy, protons	7 TeV
Nominal energy, ions	2.76 TeV/u
Peak magnetic dipole field	8.33 T
Min. distance between bunches	7 m
Design luminosity	10^{34} cm^{-2}s^{-1}
Number of turns per second	11 245
Number of collisions per second	600 million
No. of bunches per proton beam	2808
No. of protons per bunch	$1.1 \cdot 10^{11}$
No. of bunches per ion beam	592
No. of ions per bunch	$7 \cdot 10^{7}$

Table 3.2: *LHC in numbers. The center of mass energy per nucleon pair $\sqrt{s_{NN}}$ of 5.5 TeV at the LHC is about 30 times larger than at RHIC, which allows a preciser investigation of the fireball than before [lhc09], [B+ 04].*

3.2 Experiments at the LHC

Between 1996 and 1998 four large projects ATLAS, CMS, LHCb and ALICE were approved by the CERN Council. Shortly after, these were joined by two smaller experiments LHCf and TOTEM. In the following their experimental setup and physical purpose is briefly described.

A Toroidal **L**HC **A**pparatu**S** (ATLAS)

With its enormous physical dimensions (length: 46 m, diameter: 25 m, weight: 7000 t) the ATLAS experiment is the largest detector system of this kind that was ever built. It can be intersected into 4 sub detectors: an inner detector used for high resolution tracking, calorimetry, a muon spectrometer and a magnet system. These are arranged as concentric cylinders around the interaction point. The ATLAS experiment is intended to detect a broad range of particles and is particularly focused to find the Higgs Boson, the existence of which could possibly explain the spontaneous symmetry breaking in the electroweak interaction. Simply put, ATLAS inspects the origin of mass.

Compact **M**uon **S**olenoid (CMS)

The CMS is a general-purpose detector which essentially pursues the same goals as ATLAS, but with a completely different design. Almost the whole detector volume is covered by a gigantic solenoid that generates a magnetic field of 4 T. Three different sub detector systems can be distinguished inside the magnet. The innermost is a 27 layer silicon tracker system followed by a scintillating crystal electromagnetic calorimeter whose main task is to detect electrons and photons. Finally, to measure the energy of single hadrons a hadronic calorimeter forms the outermost part. Outside the solenoid large muon detectors are installed in the return yokes of the magnet.

Large **H**adron **C**ollider **b**eauty (LHCb)

LHCb is intended to investigate decays of hadrons which contain bottom (beauty) quarks known as B-mesons. In a proton-proton collision most of the B-mesons will be emitted in a very small angular range around the beam line. That is why the LHCb experiment is designed as a forward spectrometer with planar sub detectors stacked behind each other to cover especially this region. The most important sub detectors are a Vertex Locator directly surrounding the interaction point, followed by a Ring Imagining Cherenkov Detector (RICH-1) for particle identification and a low momentum tracking device. Behind the large Dipole Magnet the main tracking device is installed followed by another Ring Imagining Cherenkov Detector (RICH-2) for high momentum particle identification and an electromagnetic as well as a hadronic calorimeter. LHCb studies the CP violation in reactions that include B-mesons to find out more about the imbalances between matter and antimatter in the universe.

A **L**arge **I**on **C**ollider **E**xperiment (ALICE)

ALICE is a project with a dedicated heavy ion program. The main task of this experiment is to verify the existence and to study the properties of the QGP, an extremely transient state of matter which has shortly existed after the Big Bang (see section 2.3). The concept for the detector system is composed of a central barrel with an onion-like structure of sub detectors arranged cylindrically around the beam line and a muon forward spectrometer. The detector system of ALICE is described in more detail in section 3.3.

Large **H**adron **C**ollider **f**orward (LHCf)

LHCf is a small experimental setup (two detectors, length: 30 cm, height: 10 cm, width: 10 cm) which is located 140 m away from ATLAS. It is designed to study the origin of ultra high-energy cosmic rays by a measurement of particles close to the beam line.

TOTal Cross Section, **E**lastic **M**easurement (TOTEM)

TOTEM is a detector to measure the effective cross section in a central proton-proton collision. It is situated near the collision point at CMS.

3.3 A Large Ion Collider Experiment - The ALICE Project

The ALICE experiment studies heavy ion collisions at the LHC. In lead-lead collisions with a center of mass energy of $\sqrt{s_{NN}} = 5.5$ TeV, the intention is to create a fireball with a long lifetime which was not possible before. ALICE (length: 26 m, height: 16 m, width: 16 m, weight: 10 000 t) is built up on a complicated detector system and to some extent newly invented complex technologies. The international collaboration includes more than 1000 members from 111 institutes in 31 countries[1] [ali09].

Figure 3.2 shows the general design of the ALICE experiment which is composed of the central barrel, and the muon arm. In the central barrel, sub detectors are arranged in a cylindrical symmetry around the beam line. In the following some special features of the sub detectors are presented, where focus is put on the essential facts and physics purposes. An all-embracing description would go beyond the scope of this thesis.

For every heavy ion experiment it is important to determine the centrality of the collision. This is accomplished by the **Z**ero **D**egree **C**alorimeter (ZDC) and the **F**orward **M**ultiplicity

[1] as of July 2009.

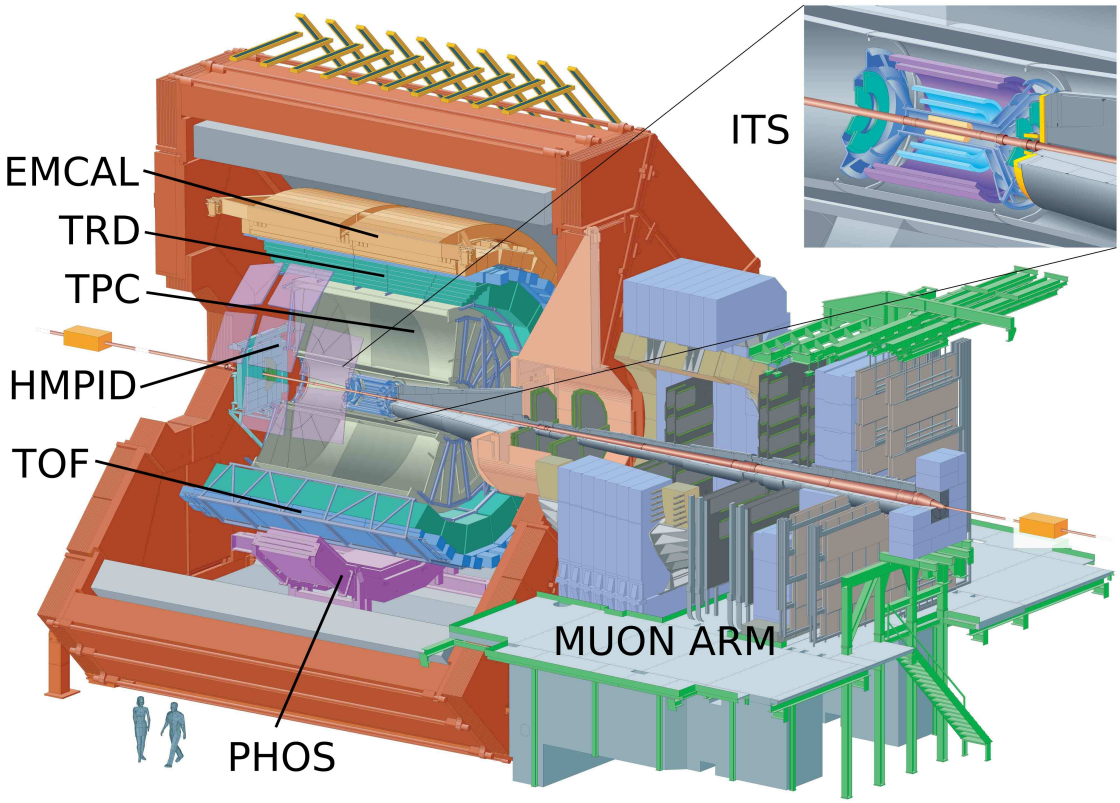

Figure 3.2: *Experimental setup of the ALICE project. The left part of the setup consists of the large L3 magnet enclosing the detectors of the central barrel. In the right part the muon arm is shown.*

Detector (FMD). The ZDC is intended to detect the energy of spectator nucleons[2] in order to make a statement on the centrality of the collision. This detector is located 115 meters away from the collision point along the beam line and largely made of so called 'spaghetti calorimeters' that serve as passive material to create particle showers. These showers can be detected via the Cherenkov effect and transformed into an electric signal which is directly proportional to the energy of the incoming protons and neutrons. The FMD, together with V0 and T0, records the number of produced particles in forward direction and their spatial distribution. T0 and V0 additionally provide precise information about the collision time and the primary vertex. FMD is essentially made of 5 rings of silicon semiconductor detectors with 51 200 individual strips that measure the total energy deposit of charged particles [ali09].

Going to the next detector level, focus is put on particle tracking detectors that cover the full azimuth. From inside out these are the **I**nner **T**racking **S**ystem (ITS), the **T**ime **P**rojection **C**hamber (TPC), and the **T**ransition **R**adiation **D**etector (TRD). Their purpose is to measure the trajectory of charged particles with high precision. A magnetic field created by the large L3 magnet (made of 8500 tonnes of iron) contributes to a deflection of charged particles due to the Lorentz force. This allows to measure the momentum p.

The ITS itself consists of three sub detectors. The **S**ilicon **P**ixel **D**etector (SPD) forms the innermost two layers As many as 50 charged particles per cm^2 and event are expected for the inner layers in heavy ion collisions. The detector is capable to map trajectories perpendicular to the beam direction with a resolution of 50 μm ($p_t > 1.2$ GeV/c). This allows to detect fast decaying particles like D- or B-mesons by a secondary vertex reconstruction. The SPD hosts about $9.8{\cdot}10^6$ Silicon Pixel Sensor Cells arranged on 1200 readout chips. The following two layers are made of **S**ilicon **D**rift **D**etectors (SDD). In this region the charged particle density is expected to be about 7 per cm^2. The SDD with a sensitive area of $70.17(r\phi) \times 75.26(z)$ mm^2 has good multi track capabilities and provides two dE/dx samples for the particle identification measurements of the ITS. The outermost two layers, where the charged particle density is predicted to be below 1 per cm^2, consist of double-sided **S**ilicon-micro **S**trip **D**etectors (SSD). The SSD is important for track matching between ITS and TPC [A$^+$08a].

The TPC, with an inner radius of 0.9 m, an outer radius of 2.5 m, and an effective length of 5.1 m, is the main tracking device and supposed to gather precise information about the evolution of the fireball and its observables in combination with the ITS and the TRD. It is composed of a 88 m^3 gas filled cylinder operated as a large drift chamber divided into two separate parts by the central electrode. The read-out is via Multi Wire Proportional Chambers (MWPC) located at the end caps.

Apart from serving as a tracking device the major task of the TRD is to separate pions from electrons by exploiting the effect of transition radiation, and thus to trigger on rare events. 540 drift chambers, arranged in 18 supermodules, create a measurable signal. A detailed description of the TRD is given in chapter 4 [ali09].

Two additional detectors are necessary for a precise particle identification. These are a **T**ime **O**f **F**light (TOF) and a **H**igh **M**omentum **P**article **ID**entification detector (HMPID).

[2] In a collision the overlapping region of the nuclei is an indicator for the centrality. Participants are directly involved in the particle production, whereas spectators do not participate in the collision but rather fly further without being affected.

TOF identifies particles in the intermediate momentum range by a measure of the time each particle requires to travel from the vertex to the detector with a precision better than 100 pico seconds. It is cylindrically shaped by covering a polar angle from 45° to 135° and the full azimuth. It is subdivided in 18 sectors with 5 modules each. These contain 1638 Multi gap Resistive Plate Chamber (MRPC) stripes with a total area of 160 m^2 and 157 248 readout channels. The HMPID is located at the two o'clock position in azimuth and only covers 5 % of the solid angle. This device is supposed to identify high momentum particles in the range of 1 GeV/c to 6 GeV/c with help of Ring Imagining Cherenkov Detectors. These are supposed to detect photons which are created by a high momentum charged particle that traverses a thin layer of C_6F_{14} [ali09].

The **PHO**ton **S**pectrometer (PHOS), with a pseudo-rapidity[3] range of $|\eta| \leq 0.12$ and an azimuthal angle of 100°, is intended to perform high resolution measurements of photons that come from π^0 decays. It is composed of 17 920 lead-tungstate crystals which are as dense as lead but as transparent as glass. Furthermore, the **E**lectro**M**agnetic **Cal**orimeter (EMCal) and the **P**hoton **M**ultiplicity **D**etector (PMD) are supposed to explore photons with a wider phase space acceptance. Especially EMCal is designed to find particle jets that carry information about the initial hard collisions. PMD provides information on photon production at forward rapidities [ali09].

The Muon Spectrometer, which consists of an absorber, five tracking stations, two detector planes, and two trigger stations, investigates charm and bottom quarkonia (J/Ψ, Ψ',Υ,Υ',Υ'') in the dimuon decay channel with an invariant mass resolution of 50 MeV to 100 MeV. The preceding absorber serves as filter to obtain a clean muon sample. The spectrometer covers the range of -4.0 $\leq \eta \leq$ -2.5 in pseudo-rapidity [ali09].

Combining the information from all sub detectors will give the possibility to study in detail the properties of the QGP within the ALICE project.

[3] In relativistic particle physics the quantity pseudo-rapidity is a measure for the angle from particle to beam axis. It is calculated via the formula: $\eta = -\ln\left[tan\left(\frac{\theta}{2}\right)\right]$. θ is the angle to the beam axis.

4. The Transition Radiation Detector

4.1 Dimensions, Capabilities, and Physical Purpose

As briefly described in section 3.3 the main task of the ALICE **T**ransition **R**adiation **D**etector (TRD) is charged particle tracking and identification. The detector is built up out of 18 supermodules cylindrically arranged around the beam axis with a coverage of $|\eta| < 0.9$ in pseudo-rapidity and 2π in azimuthal direction. It is located between the TPC and the TOF detector with an inner radius of 2.90 m, an outer radius of 3.68 m and a length in z-direction of 7 m. The whole detector is endowed by an active area of 694 m^2 distributed on a total number of about $1.18{\cdot}10^6$ readout channels to process the signals created in the active volume. Moreover, a radiator for the possible production of **T**ransition **R**adiation (TR) by electrons is attached to each drift chamber [Ems10].

The TRD is the main electron detector of the ALICE experiment providing the necessary electron identification for momenta exceeding 2 GeV/c. In this case the pion rejection measurement via energy loss in the TPC is no longer satisfactory. In addition to the research of heavy vector meson resonances in the di-electron channel and the investigation of semi-leptonic decays of hadrons with open charm and open beauty in the single electron channel[1], the TRD can be used as a jet trigger. Furthermore, by coincidence measurements with respect to the muon decay channel, the TRD can enhance the yields of J/Ψ and Υ particles [trd01].

The design goal for the pion rejection is a factor 100 for momenta that exceed the value of 1 GeV/c in lead-lead collisions at 90 % electron efficiency. In conjunction with the TPC, the TRD is indented to map the J/Ψ and Υ continuum. For this purpose an overall mass resolution of 100 MeV/c^2 at the Υ mass is necessary. In order to obtain this resolution the TRD has to achieve a momentum resolution of about 175 MeV/c for 5 GeV/c electrons. As a result of this, the average pad area was chosen to be about 6 cm^2 allowing for a tracking efficiency of 90% for single tracks. This contributes to an occupancy of 34% at the highest simulated multiplicity density of $\frac{dN_{\mathrm{ch}}}{d\eta} = 8000$. This multiplicity density arose from an extrapolation at SPS energies (17 GeV). At the much higher RHIC energies this number was extrapolated again and qualified to about $\frac{dN_{\mathrm{ch}}}{d\eta} = 3000$ [A$^+$08a].

4.2 Transition Radiation

Relativistic charged particles crossing the interface between two media with different dielectric constants can create **T**ransition **R**adiation (TR). Descriptively spoken, a particle approaching the boundary interacts with the field of its self-induced charge that is mirrored at the boundary to form a time varying dipole field which emits radiation. The

[1] This proceeds in conjunction with the high resolution secondary vertex reconstruction of the ITS.

double differential energy spectrum concerning the solid angle Ω and the frequency ω of this radiation can be expressed by [Adr]:

$$\frac{d^2W}{d\omega d\Omega} = \frac{\alpha}{\pi^2} \cdot \left(\frac{\theta}{\gamma^{-2} + \theta^2 + \xi_1^2} - \frac{\theta}{\gamma^{-2} + \theta^2 + \xi_2^2} \right)^2 \tag{4.1}$$

This equation is only valid for $\gamma >> 1$ and ξ_1, $\xi_2 << 1$, where $\gamma = \frac{E}{m_0 c^2}$ denotes the Lorentz factor. This is an important quantity in the context of detector physics. It stands for the ratio of total energy to rest mass of the traversing particle. The variable α stands for the fine structure constant as introduced in section 2.2 and θ is the angle of the emitted radiation. ξ_1 and ξ_2 are functions of the dielectric constants ϵ_1 and ϵ_2 as well as the plasma frequencies for an electron $\omega_p = \sqrt{\frac{4\pi\alpha m_e}{n_e}}$; with the electron mass m_e and density n_e. The relation between these variables is given by:

$$\xi_i = \frac{\omega_{p_i}^2}{\omega^2} = 1 - \epsilon_i(\omega) \tag{4.2}$$

The angular distribution of the TR is peaked at a value of $\theta = \frac{1}{\gamma}$. By increasing the particle energy, θ becomes sufficiently small so that almost the whole part of the radiation is emitted in the direction of the incident particle [Kle02]. Based on this assumption equation 4.2 can be integrated over the solid angle which results in [Adr]:

$$\frac{dW}{d\omega} = \frac{\alpha}{\pi} \cdot \left(\frac{\xi_1^2 + \xi_2^2 + 2\gamma^{-2}}{\xi_1^2 - \xi_2^2} \cdot \ln \left\{ \frac{\gamma^{-2} + \xi_1^2}{\gamma^{-2} + \xi_1^2} \right\} - 2 \right) \tag{4.3}$$

To obtain the energy range of the TR photons, equation 4.3 has to be calculated by considering the composition of the radiator material of the TRD (section 4.5.2). The result is that TR is produced in the X-rays domain with a threshold of $\gamma > 1000$ [A$^+$08a]. Bearing in mind that the TRD investigates particles in an energy range of 1 GeV to 100 GeV, electrons will provide TR in the keV range, while the massive pions of 140 MeV/c^2 are not able to produce TR. That offers an effective tool to discriminate between these particles. Therefore, TR is a powerful tool for particle identification even in momentum ranges between 1 GeV/c and 100 GeV/c where Cherenkov and ionization loss measurements do not provide adequate resolution.

4.3 Principle of Multi Wire Chambers

Multi Wire Proportional Chamber (MWPC)

A MWPC serves as an instrument to detect ionizing radiation. Based on its principle the energy of this radiation can be determined. A simplified construction of a MWPC is given in figure 4.1. It is composed of an anode wire plane situated between two cathode planes that mostly consists of metal foils or stripes for the signal induction. The volume is filled with a gas of low electron affinity as Argon (Ar) or Xenon (Xe).

The gas is ionized by the radiation or the particle which shall be detected. By this process electrons are produced and they are accelerated by the electric field of the anode wires. In the vicinity of the wire plane extreme fields are created that grow with 1/r. Due to

the strong acceleration in this region electron avalanches are created through multiple-ionization of electrons. These are collected at the anode wires and produce a current that is amplified and transformed into a voltage signal. The signal height is proportional to the previously deposited energy in the chamber. The Townsend coefficient α_T describes the multiplication of ionization and depends on the electric field as well as on the gas density. For α_T a general expression is not available, that is why it has to be determined experimentally. Based on this coefficient, an important quantity to describe the yields of the amplification process is the gain factor G defined as [BRR08]:

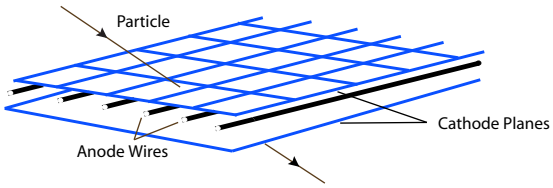

Figure 4.1: *Simple illustration of a MWPC.*

$$G = \exp\left\{\int_{r_0}^{r_1} \alpha_T(s)ds\right\} \tag{4.4}$$

In this formula r_0 depicts the place where the avalanche process starts and r_1 denotes the radius of the amplification wire.

In addition to the counting gas (as Ar or Xe) a gas quencher is admixed to control the avalanche process. By electron production an avalanche of positive gas ions is created which can decay in their ground state by emission of photons. These photons can release further electrons (e.g. at the cathode planes) so that the avalanche process self sustains and the detector becomes insensitive to further particles. The quencher is intended to absorb the photons in order to interrupt the signal.

Typical wire chambers provide fast signals with a rise time of about 0.1 ns, a width of 20 ms, and a resolution of ≈ 600 μm [Ams07].

Extension to Drift Chamber

The wire chamber can be extended by another volume with a homogeneous electrical field. This composition is termed drift chamber. With the additional measurement of the drift time a 2 dimensional trajectory of the incident particle can be traced. An external magnetic field that is perpendicular to this plane contributes to a deflection by the Lorentz force on which basis the momentum of a particle can be determined. In combination with the energy-loss measurement in the chamber, the particle can be identified by calculating its mass. The detectors of the TRD are composed of drift chambers as depicted in figure 4.2. In the drift region a homogeneous field is created by the potential difference between the electrode at the entrance window and the cathode wires. The uniformity of the drift velocity, which depends on the gas quality and the electric field, has the main impact on the position resolution of the detector in drift direction.

The so-called amplification region located between cathode wire plane and cathode pad-plane works just like the MWPC as introduced above.

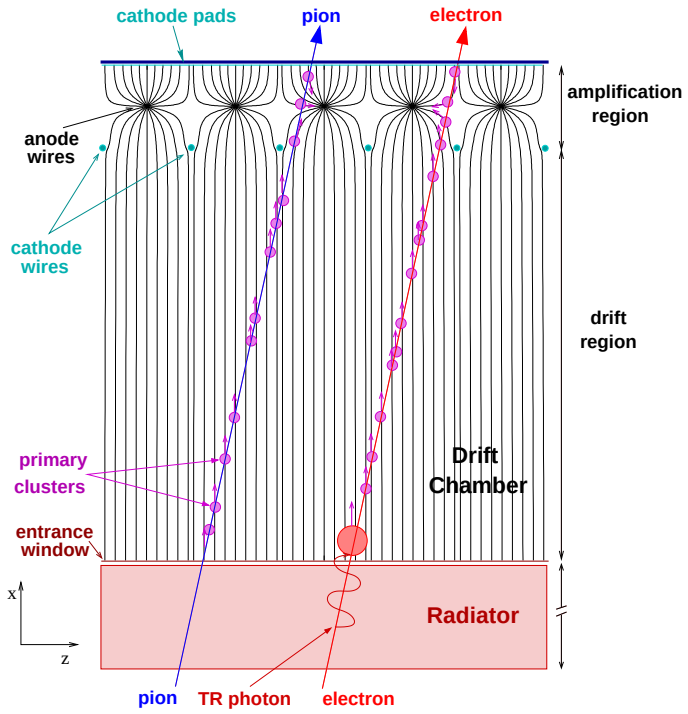

Figure 4.2: *Cross section of the drift chamber setup used in the TRD. The chamber is composed of a drift region, an amplification region, and a padplane for readout. Moreover, a radiator is attached to the bottom for production of TR. The black field lines are parallel in the drift region and indicate a homogeneous field. In the amplification region the field lines are much denser [trd01].*

Signal Generation in the Drift Chamber

The readout of the ALICE TRD is via the padplane. Electrons produced during the avalanche process move to the nearest anode wire in in less than 1 ns. The positive ions are about 1000 times slower when traveling back towards the cathode wires. The signal is induced by an image charge on the cathode plane of the slow moving ions, whereas the fast moving electrons do not influence this signal. This is due to the relatively large capacity of the cathode pads. The padplane is subdivided into stripes with a width of about 7 mm so that charge sharing between adjacent pads occurs in order to improve the position resolution (see section 4.5.4). The induced signal is then further processed by the readout electronics.

4.4 Structure and Design of the TRD

Figure 4.3 shows the hierarchic organization of the detectors starting from the whole TRD as a hollow cylinder down to single channels of the readout plane. The TRD is made of 18 individual supermodules which are arranged in φ-direction with respect to cylinder coordinates to fill the entire azimuth. Each supermodule consists of 30 individual tracking detectors that are equipped with additional radiator material to produce TR. These detectors are organized in 5 stacks (in z-direction) and 6 layers (in r-direction).

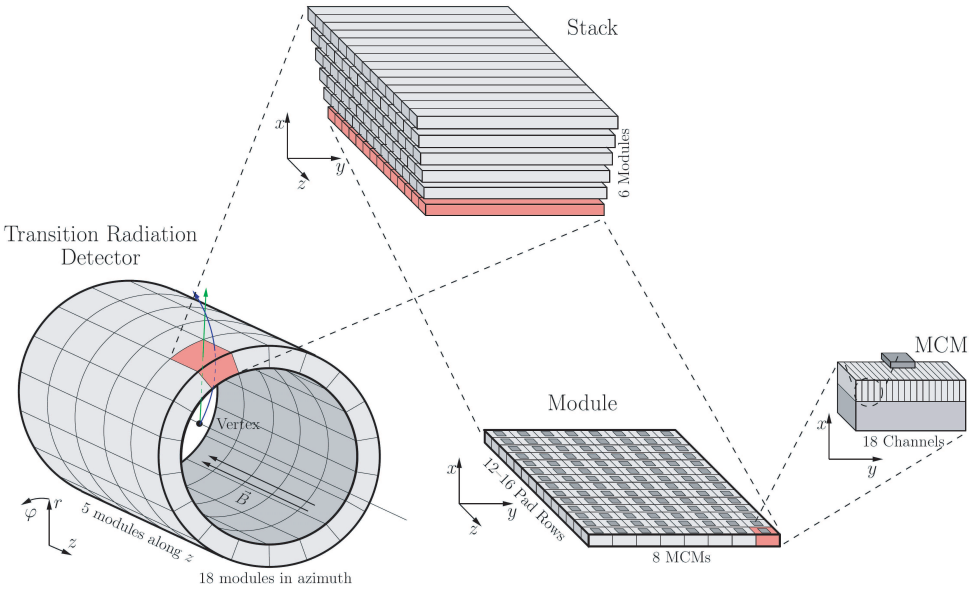

Figure 4.3: *The TRD consists of 18 supermodules, each hosting 30 individual drift chambers arranged in 5 stacks and 6 layers. In a single chamber 8 MCMs are placed in φ-direction and 12 or 16 pad rows are mounted in z-direction. A MCM consists of 21 channels that provide readout for 18 pad columns. The 3 channels left over are exchanged between neighboring MCMs for tracklet processing (see section 5.2.2).*

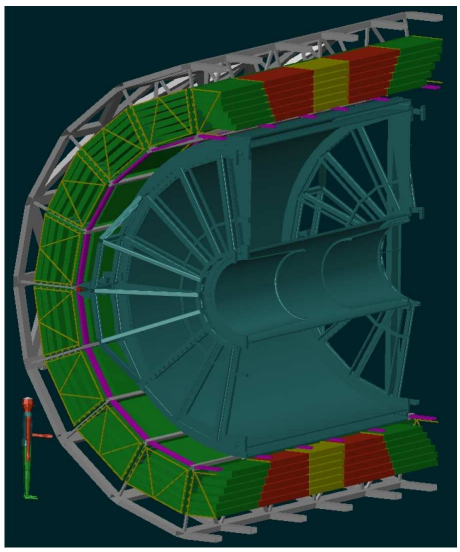

Figure 4.4: *Illustration of supermodules inserted in the space frame. The empty blue frame at the inner part depicts the place where the TPC is located, whereas at the outer part of the supporting frame the TRD is enclosed by the TOF [ali09].*

Each detector is equipped with a padplane of copper stripes arranged in 12 to 16 rows[2] (z-direction) and 144 columns (φ-direction). On the top of each detector 96 -128 **M**ulti **C**hip **M**odules (MCMs)[2] with 18 channels are placed to readout the signals induced on the padplane. The MCMs are arranged on 6-8 **R**ead **O**ut **B**oards (ROBs)[2] and are controlled by a **D**etector **C**ontrol **S**ystem board (DCS board).

The total mass of the detectors in the central barrel sums up to 75 t, with the TRD carrying nearly one half of this weight (29.7 t). For stability reasons the TRD supermodules are inserted in a space frame (see figure 4.4).

4.5 Readout Chamber

4.5.1 General Design

The detectors that were introduced in section 4.4 are composed of a 48 mm thick radiator, a 30 mm drift region, a 7 mm multi-wire proportional chamber section, followed by a 23.16 mm honeycomb carbon fibre sandwich back panel to support the padplane. Finally, the front-end electronics are mounted directly on top of the back panel. Figure 4.5 shows a profile of this setup. The general term for this assembly is **R**ead**O**ut **C**hamber (ROC). Its main purposes are to identify electrons through high energy deposit because of TR and particle tracking.

4.5.2 Radiator

The task of the attached radiator is to produce TR photons that contribute to the overall signal produced in the drift chamber. Photon emission from a single boundary is very

[2]This depends on the chamber type. The chambers in stack 2 are shorter with respect to the z-axis.

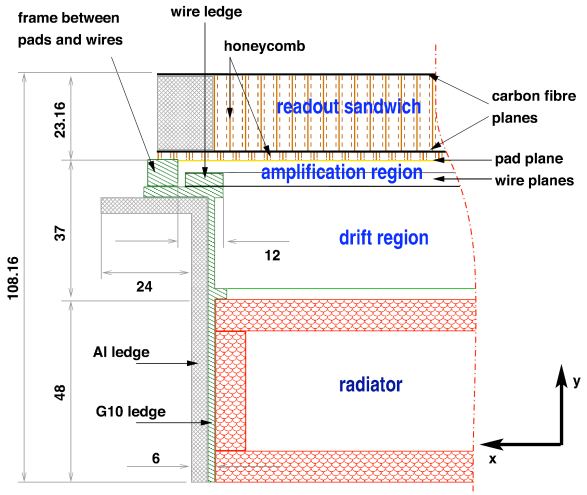

Figure 4.5: *Profile of the ROC consisting of a radiator, a drift and amplification region, the padplane and the front-end electronics. The PCB voltage divider is equipped with a 11.7 MΩ resistor that permits a current of 165 μA. Consequently, the current of back drifting ions (0.5 μA) will not affect the drift voltage significantly. With each single ROC both, particle identification and tracking is possible [Ems10].*

small, hence the radiator material has to consist of many boundaries to acquire a reasonable efficiency. Contrary to this, its length had to be minimized to prevent substantial energy loss due to bremsstrahlung.

Ideally, foils placed equidistantly one above the other in a distance to create constructive interference are used as radiator material. Not only the fact that it is nearly impossible to align the foils uniformly for 540 single chambers, but also the necessity of strong metal frames[3] for the support of the numerous foils suggests another choice of the radiator material. That is why the radiator of the drift chamber is designed in a sandwich structure considering both, high TR efficiency and as little absorption as possible. Fibre mats and special foams of randomly-orientated boundaries, which are mechanically superior although less TR efficient, were investigated. The final results led to a sandwich construction of both, foam and fibres, with a supporting structure of **Rohacell HF 71** foam with acceptable TR properties to ensure mechanical stability and **Polypropylene** fibres for a good signal efficiency [trd01].

With regard to this design the radiator with a thickness of 48 mm creates on average 1.45 X-ray photons in a range of 1 to 30 keV per incident particle [A$^+$08a].

4.5.3 Drift and Amplification Region

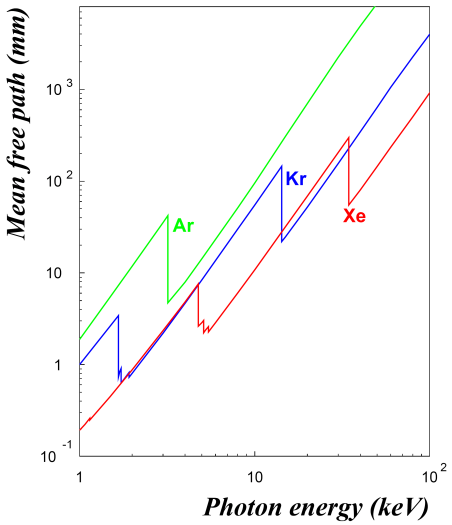

Figure 4.6: *Mean free path of photons in different noble gases.*

The drift electrode is put on a potential of -2.1 kV. This leads to a drift field of 700 V/cm between the entrance window of the drift region and the cathode wire plane. To guarantee the homogeneous distributed electrical field, a series of copper strips in a voltage divider chain is attached to the inner wall of the drift volume. For photo-absorption in the energy range of 1 to 30 keV a high Z-counting gas is necessary. It is required that the produced TR photons are stopped in the early phase after entering the drift region (see section 4.5.4). As depicted in figure 4.6, Xenon (Xe) fulfills this requirement best. The drift volume is filled with a gas-mixture of 85 % Xe (counting gas) and 15 % CO_2 (quencher) operated at a slight overpressure of 0.1 mbar to avoid air contamination that would contribute to unintentional absorption of the drifting electrons. The gas tightness of the chamber is extremely important as Xe is rare in nature and therefore an expensive gas.

The dimensions of the amplification region are illustrated in figure 4.7. The anode wires (diameter of $d_0 = 20$ μm) are put on a potential of +1.5 kV, whereas the cathode wires and the padplane are grounded. The signal is induced on the padplane which consists of nearly rectangular copper stripes with an average length and width of about 7 cm and 7 mm, respectively (see section 4.5.4). The gas gain is expected to reach values of $G \approx 5{\cdot}10^3$ to $5{\cdot}10^4$ [trd01].

[3] An unintended side effect of the massive metal frames would be a shadowing of other detectors.

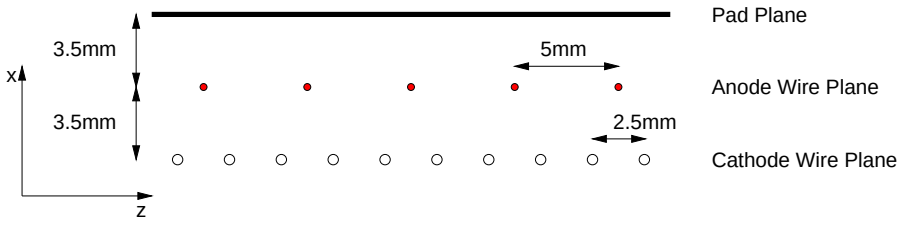

Figure 4.7: *Wire geometry of the amplification region in the local coordinate system (see section 5.1.1). The anode wires are located between the padplane and the cathode wire plane (both of which are on ground potential) [trd01].*

4.5.4 Signal Formation

Small cables soldered to the padplane transfer the signal to the MCMs. Figure 4.8 offers a summary of the whole signal formation process. The left panel shows the evolution of the signal allocated on multiple pads. By the assumption of a constant drift velocity, this signal can be transformed into a particle track that traverses the r-φ-plane. The inclination of the track in the bending direction φ of this profile provides a direct measurement of the transverse momentum if a primary track is assumed. This quantity is of great importance in terms of particle tracking and the trigger system.

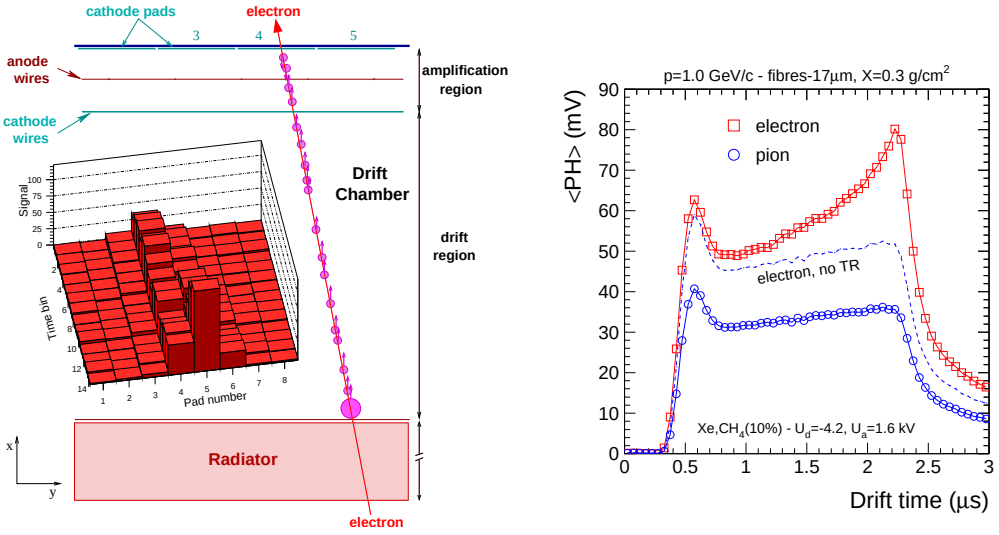

Figure 4.8: *Schematic illustration of the signal formation process in local coordinates (see section 5.1.1). Left panel: View of the induced signal in the drift region with respect to the x-y-plane including 14 time bins. Right panel: Average pulse height plot of the induced signals over 3 µs. On average, electrons (red squares) deposit more energy than pions (blue circles). The peak at the end of the drift plateau is due to TR, whereas the dashed line represents the case if no TR is produced by an electron. It looks similar to the pion signal yet with an increased average pulse height [trd01].*

Essentially, the TRD is used to discriminate between electrons and the much heavier pions in the momentum range above 1.5 GeV/c. Looking at the right panel of figure 4.8, the average pulse height of all pads accumulated over a range of 3 μs is depicted. Two properties lead to an efficient discrimination of pions and electrons: One is the increased average energy deposit of the electrons in the drift volume, the other is the additional induced signal at the end of the drift time because of TR.

By closer examination of the pulse height plot different regions can be distinguished. The conspicuous peak at the beginning appears because of electrons that move from both sides of the amplification towards the anode wires. Afterwards, a plateau is reached describing the electrons produced in the drift region. The probability for TR photons to be absorbed decreases exponential with the distance passed in the drift region [Ams07]. Therefore, it is likely that the majority of the photons deposits its energy shortly after the entrance to the drift region. This deposition can proceed by the Photo-effect and the Compton-effect. The electrons produced by these mechanisms reach the amplification region just at the end of the drift plateau and thus contribute to a superposition of energy deposit by ionization and TR. As pions do not produce TR the drift plateau stays flat without showing a peak at large drift times.

Pad Response Function

The ions created in the avalanche process induce a positive charge on the cathode pads in a certain time bin. At first it seems that the φ resolution is limited by the pads with an average width of 7.25 mm arranged in 144 columns per ROC. With an optimized gap of the wire planes (see figure 4.7) charge is induced on two to three adjacent pads[4], which offers a possibility to reconstruct the φ coordinate with a finer resolution as imposed by the pad geometry using the **P**ad **R**esponse **F**unction (PRF). With regard to the signal distribution on adjacent pads, also-called 'hit', the PRF can be approximated by the ratio

[4]These so-called two-pad-clusters and 3-pad-clusters deliver the optimal signal-to-noise ratio.

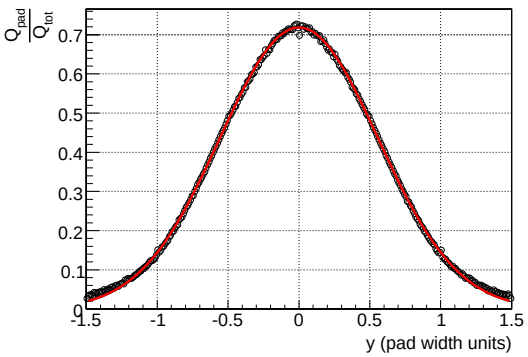

Figure 4.9: *Visualization of the PRF (pad width W = 6.95 mm) [Wul09].*

of the charge induced on a single pad Q_{single} and the total charge induced on all pads Q_{tot} in one time bin. It is given by [BRR08]:

$$\text{PRF}(y) = \frac{Q_{\text{tot}}}{Q_{\text{single}}} \approx Ae^{-\frac{y^2}{2\sigma^2}} \tag{4.5}$$

In this formula y denotes the local position in pad units and σ^2 indicates the variance of the Gaussian distribution (see figure 4.9). In this context the position resolution was investigated in [Wul09] using cosmic ray data and yields values between 389 μm and 418 μm that depend on the supermodule layer[5]. This is a great improvement in comparison to the average pad width.

Tilted Pads

The readout pads have the shapes of parallelograms with an aspect ratio of about 10:1. Therefore, the z-position resolution is limited by the pad length as charge sharing does not occur on this length scale. To improve the z-position resolution the pads are slightly tilted by an angle α in opposite direction in consecutive layers with respect to the z-axis. Let φ be the measured position in azimuthal direction, then the tilted pad aware value φ' is calculated by [trd01]:

$$\varphi' = \varphi + (-1)^L \tan(\alpha) \cdot (z - z_0) \tag{4.6}$$

In this formula L indicates the layer, z_0 represents the center of the pad in z-direction, and z denotes the 'real' track position. Given this formula, φ and z are not independent coordinates any more. With the application of a dedicated tracking tool the z-position resolution can be considerably enhanced without a noticeable loss of the φ-position resolution.

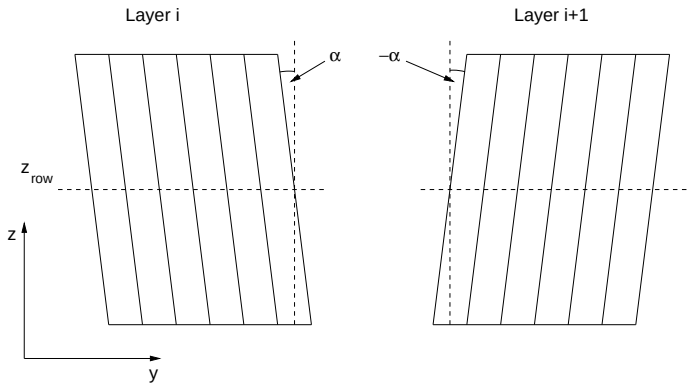

Figure 4.10: *Pad tilting in the y-z-plane (local coordinate system) by an angle of $\alpha = 2°$ to enhance the z-position resolution. The left and the right panel show the opposite tilting in consecutive layers [trd01].*

4.5.5 Front-End Electronics

Because the TRD also serves as a trigger detector, data has to be processed in an early stage after the collision. That is why the first data processing is already performed by the MCMs located on the top of each chamber. This contributes to a minimization of signal loss and deterioration.

Each MCM is connected to 18 pads so that all 144 columns are managed by 8 MCMs per row[6]. Additionally, one or two channels are connected to pads which actually belong to the right-sided and left-sided neighbor MCM to be able to calculate the tracklet position at the border channels, too. The MCM is a composition of the **P**re-**A**mplifier/ **S**h**A**per (PASA) that pre-amplifies the incoming current signals to transform them into a voltage on a pedestal level and the **TRA**cklet **P**rocessor Chip (TRAP-Chip). This Chip itself is composed of an **A**nalog to **D**igtial **C**onverter (ADC), the **T**racklet **P**re**P**rocessor (TPP), an event buffer, and 4 MIMD CPUs. An overview of the front-end electronics is given in figure 4.11.

After an individual shaping of each channel in the PASA, the signals are transmitted to 21 ADC channels where they are transformed to digital values with a sampling rate of 10 MHZ, a resolution of 10 bits, and an input range of ± 1 V [Ang06]. In the next step the data is filtered and stored in the event buffer for further readout. Thereafter, the TPP searches for possible hits and fills the fit registers. The TRAP uses the parametrized clusters to perform a straight line fit over a range of at most 30 time bins in one chamber. This fit is called **tracklet**. Further information concerning TPP and TRAP is given in section 5.2.

[5]These are average values for different angles of the primary particle.

[6]Actually, the MCM has 21 channels, but only 18 are read out. The three rest channels are located at the borders and are important for the tracklet processing (see section 5.2.2).

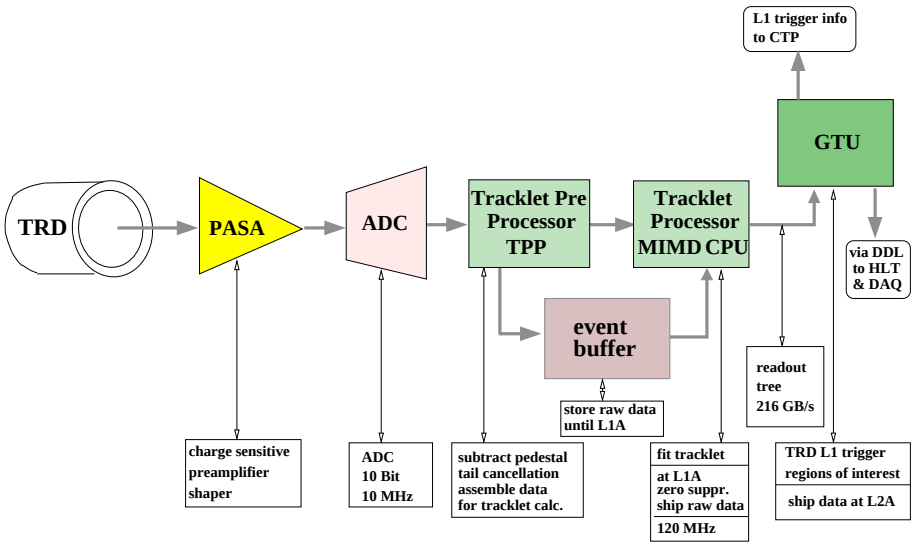

Figure 4.11: *Scheme of the signal processing in the MCM [trd01].*

4.6 Trigger System and Data Flow

4.6.1 ALICE Trigger System

In heavy ion collisions the ALICE experiment produces enormous amounts of data. Therefore, it is necessary to select the most important events, e.g. to search for heavy vector mesons as well as for central collisions and minimum bias events. This task is governed by the ALICE trigger system composed of a **C**entral **T**rigger **P**rocessor (CTP) with 60 parallel inputs to gather information from the trigger detectors by a decision logic and a Trigger Distribution Network to deliver the trigger signals to the detectors. The trigger essentially works on three levels based on the complexity of data analysis. The first decision is made after 1.2 μs via the Level 0 trigger, followed by the Level 1 decision after 6.5 μs, and finally the Level 2 trigger is expected at 88 μs [E$^+$05].

For L0 information of the FMD is required concerning the multiplicity, the forward backward distribution of produced particles, and the the position of the primary vertex. If L0 is accepted, the inner detectors as SSD and SDD start data processing. Furthermore, information about the centrality is gathered from ZDC, FMD, and the Muon Spectrometer. The TRD has already started data taking by the initiation of the pretrigger signal generated right after the collision. This information is provided by V0, T0 and TOF.

Among others the TRD provides information for the CTP to make the L1 decision. The criteria for an accept depend on the transverse momentum of found tracks. If L1 is accepted, the TPC, which produces the largest data volume with a drift time of about 100 μs, is read out. The High Level Trigger is the last phase of the trigger system that requests all detectors for a complete readout of the raw data.

4.6.2 TRD Trigger System

The main task of the TRD within the ALICE trigger system is to trigger on high energy electron positron pairs that possibly originate from a particle jet, J/Ψ and Υ decays, or conversions of direct photons. In addition, the single electron channel of open charm and open beauty can be explored. This trigger decision has to be made within a time interval of 6.5 μs to contribute to the L1 accept.

After the pretrigger signal was received a first acquisition of data is done by the TPP during a drift time of 2 μs. After about 2.2 μs the TRAP starts to calculate the tracklets in four CPUs. Around 1.8 μs later the tracklets are shipped to the **G**lobal **T**racking **U**nit (GTU) for a more precise tracking procedure. While the data is shipped, the GTU already starts the calculations. These are finished after a time-frame of about 6.3 μs starting from the initial interaction. Accordingly, the trigger decision of the GTU is transmitted to the CTP in less than 0.2 μs [trd01]. The trigger timing is visualized in figure 4.12.

4.6.3 Readout Scheme

All electronics on a ROC are controlled by a DCS Board, a small Linux operated computer the central processing machine of which is an Altera EPXA1 FPGA with an embedded ARM Core. One task of the board is to send configurations to the MCMs via the **S**low **C**ontrol **S**erial **N**etwork (SCSN) interface controlled by the FEE-Server [Wes09].

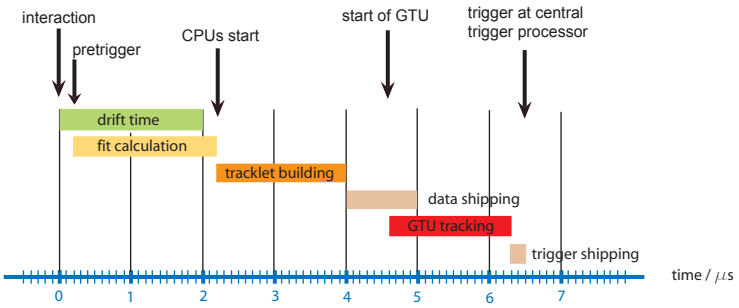

Figure 4.12: *Trigger timing for the TRD.*

Among others, the board is equipped with a TTCrx trigger interface which steers the data readout when receiving a positive signal from the trigger logic. The readout scheme for both L0 and L1 similarly follows a hierarchic tree-like structure. If L0 is initiated, the tracklets information is shipped to the GTU. In the case of a L1 trigger the raw data is read out to make more precise calculations. Assuming that the DCS-Board receives the pretrigger signal and the L0 accept, the MCMs are requested to start the readout procedure. The lowest level of this tree are the column mergers which accumulate data from the three neighbor MCMs on a ROB in one column. The four column mergers of the dedicated ROB send the data to the board mergers. Then four ROBs (three ROBs in stack 2) transfer the data from their board mergers to the half-chamber mergers from where it is transmitted via the network interface of the TRAPs to the **O**ptical **R**eadout **I**nterfaces (ORIs). Therefore, the so far processed data is accumulated half-chamber-wise to ship it to the GTU with the help of optical fibres. Within the GTU **T**rack **M**atching **U**nits (TMUs), each hosting a FPGA for data processing, receive the data from the 12 half chambers of one stack. The transmitted tracklet information is then used to calculate a track by a straight line fit through at least four chambers. If the track fulfills user defined properties, the GTU sends an accept to the CTP.

In the case of an additional L1 accept the readout chain is the same, except the fact that the raw data is stored in the **D**ata **A**c**Q**uisition system DAQ.

5. Online Tracking Procedure in the TRD Test-Setup

5.1 Experimental Setup in Münster

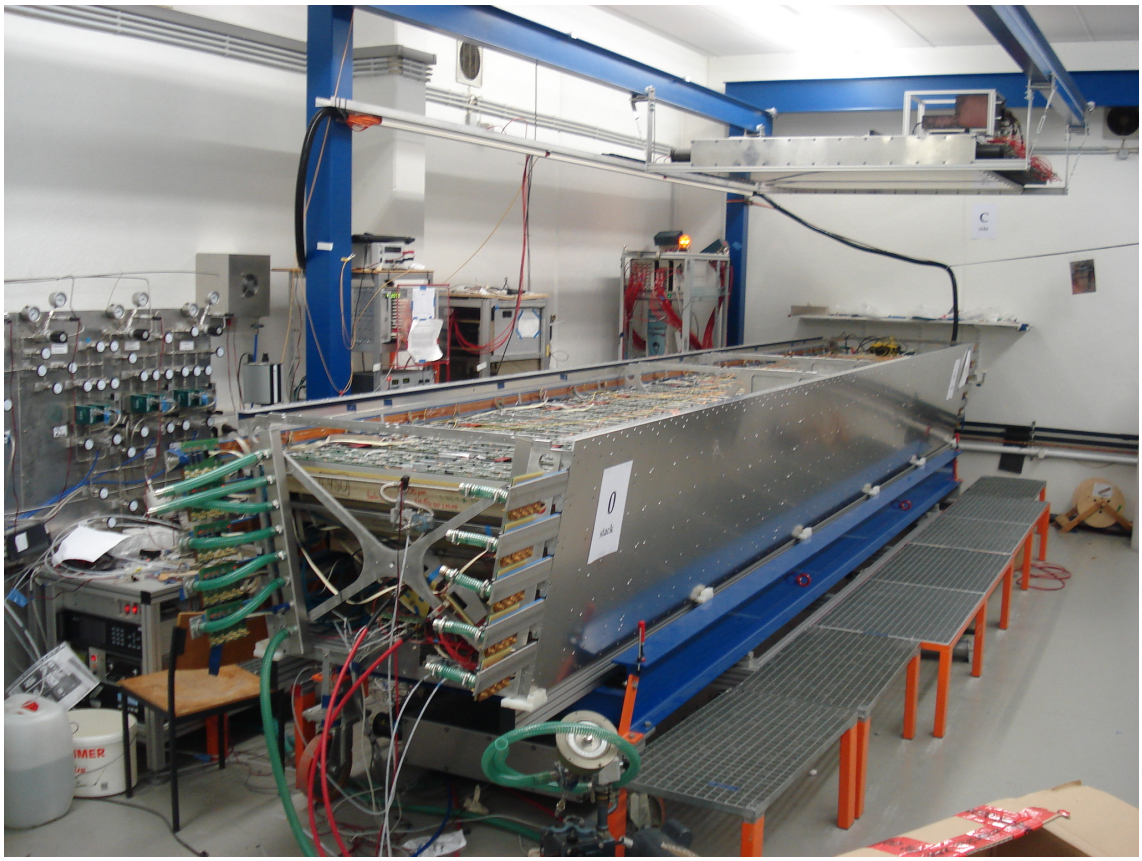

Figure 5.1: *View of supermodule VIII in the assembly hall of Münster. In the upper part the movable device of the cosmic trigger can be recognized.*

Being a part of the ALICE collaboration, the working group at the 'Institut für Kernphysik' in Münster assembles the TRD supermodules. Figure 5.1 shows the assembly hall and a supermodule in the construction phase with 5 layers already installed.

The setup enables to detect particles with the help of a cosmic trigger installed in the assembly hall (see section 5.1.2). Apart from a full functional test of supermodules, this setup allows to study online tracking, alignment of the chambers [Sic09], and the calibration of the gain using cosmic rays. Alignment describes the positioning of the installed chambers relative to each other. Due to deformations and limited accuracy during the assembly, the real positions of the chambers differ from the exact design values. The alignment program corrects these position deviations to improve the resolution of recon-

structed tracks. In addition, it is significant for the PID that amplitudes for signals with the same energy deposit are equal for all pads. Hence, a so-called gain factor for each pad has to be found [Alb10].

In this thesis cosmic tracks are used to investigate resolution and efficiency of online tracklets (see section 5.2).

5.1.1 Local Coordinate System

Unlike the final operation at CERN, the data taking in Münster proceeds in the standalone mode without consideration of other detectors. Therefore, it is helpful to switch from global cylindrical coordinates to a local right-handed Cartesian coordinate system (see figure 5.2, left panel). In this system the z-axis still coincides with the beam axis which is directed opposite to the muon arm. On this axis the longer side of the supermodule covers a range of about -350 cm $\leq z \leq$ 350 cm. However, ϕ and r are substituted by the respective coordinates y and x which are both perpendicular to the beam line. The local coordinates can be transformed into the global radius and the azimuthal angle via the formulas $r = \sqrt{x^2 + y^2}$ and $\phi = \arctan\left(\frac{y}{x}\right)$. The origin of the local coordinate system (0,0,0) refers to the collision point. With regard to the profile of a supermodule concerning the x-y-plane, the local x-axis describes the direction of drifting electrons and it is given by the normal that intersects the module at the global azimuthal positions $\alpha = 10° + 20° \cdot i$ with $i \in$ [0,17] (see figure 5.2, right panel). The y-axis points to the direction of pad columns. The angle in the x-y-plane is termed ϕ, the one of the x-z-plane is labeled θ. The x-coordinate covers a range of about 290 cm $\leq x \leq$ 370 cm. The range of the y-coordinate depends on the layer. A minimal range of -48.7 cm $\leq y \leq$ 48.7 cm and a

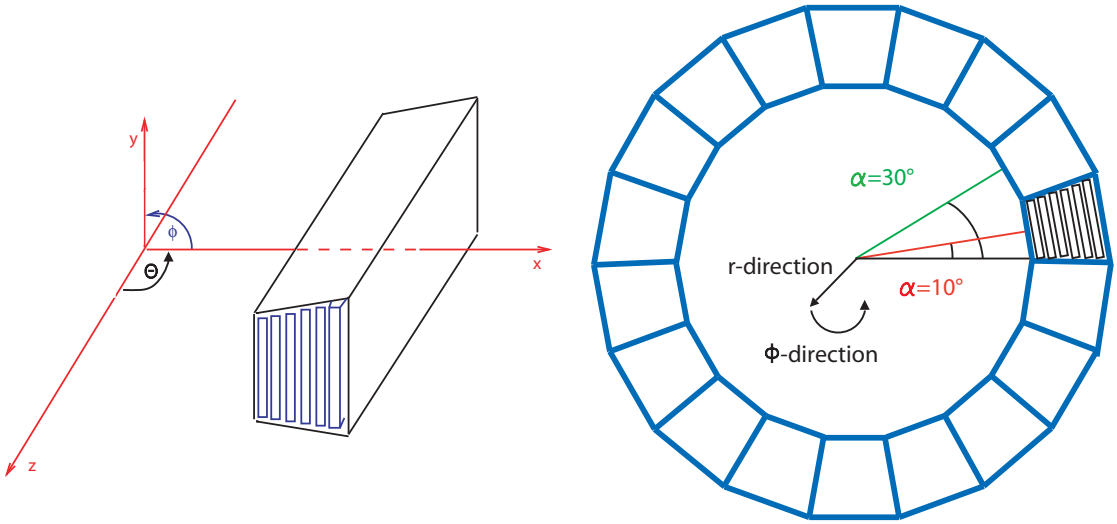

Figure 5.2: *Coordinate systems. Left panel: local coordinate system for the test setup in Münster, right panel: global coordinate system with respect to the r-ϕ-plane. The supermodule under construction in Münster always refers to the global azimuthal position of* $\alpha = 10°$.

maximal range of -58.9 cm $\leq y \leq$ 58.9 cm is given by the bottommost layer (layer 0) and the topmost layer (layer 5), respectively.

The y-coordinate is of particular importance in the context of particle tracking since based on the y-precision the transverse momentum of a particle track is calculated. Almost all resolution calculations made in this thesis concentrate on the local position y and the deflection angle ϕ in the x-y-plane.

5.1.2 Cosmic Trigger

Cosmic Rays

High energy particles from outer space entering the terrestrial atmosphere are named cosmic rays. These 'cosmics' are used as a natural source of particles for the data taking within the TRD test setup in Münster.

The major part of so-called primary cosmics consists of protons ($\approx$ 79 %) and helium ($\approx$ 15 %). Additionally, electrons as well as heavy nuclei like carbon, oxygen or iron form a small fraction. Apart from the rays of the solar flares all primaries arise from outside our solar system. Among other things, they are created by nuclear synthesis of stars and accelerated at astrophysical sources. The energy of primary cosmic rays covers a range of 10^9 eV to 10^{20} eV. A fraction of secondary cosmic rays originates from interactions of primaries with the terrestrial atmosphere. Within the cosmic ray spallation heavy nuclei as carbon or oxygen split up into lighter ones. Therefore, the secondary particles,

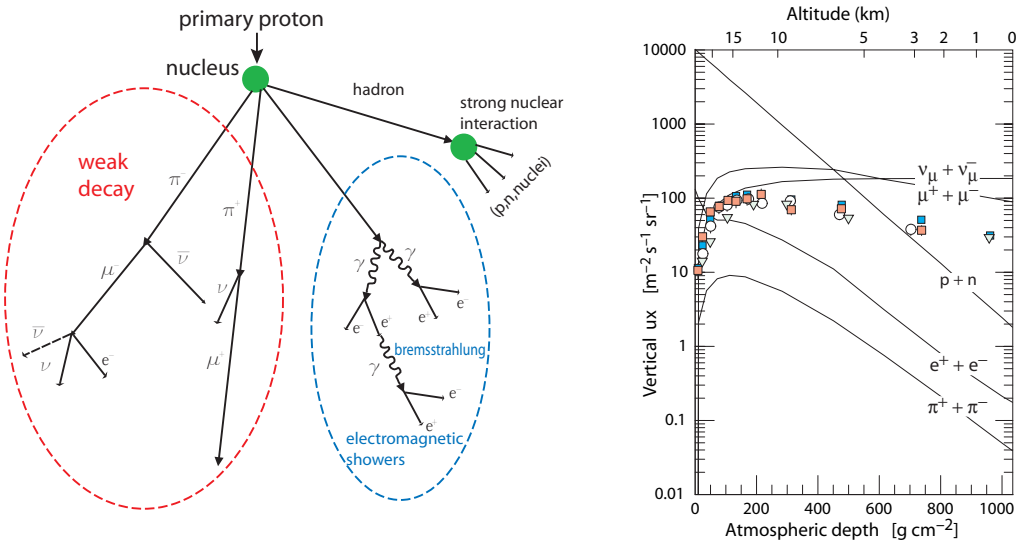

Figure 5.3: *Left panel: electromagnetic showers, weak decay and hadronic showers are responsible for the rich amount of particles produced by the interaction between a primary cosmic ray and an atom of the atmosphere. Right panel: vertical flux of more or less stable particles in the atmosphere [A+08b]. In upper elevations protons and neutrons dominate the spectrum. The composition at sea level mainly consists of muons and neutrinos. Because of their small interaction probability the neutrinos do not play a role in this case of particle detection.*

among others, consist of lithium, beryllium or boron which are not an end product of nuclear synthesis and thus have a larger abundance than in the solar system [A$^+$08b].

Figure 5.3 (left panel) shows the production of secondary cosmic rays in the terrestrial atmosphere. Initially, a primary particle hits an atom of the atmosphere in a nucleon-nucleon interaction to produce further particles. A weak decay, electromagnetic showers and hadronic interactions are three different possibilities to create a great variety of different particles. In the hadronic interaction hadrons like protons, pions, or kaons are produced which can repetitively interact in the same way as the primary particle to create a hadronic shower. Pions and kaons with an average lifetime of 26.0 ns and 12.4 ns, respectively, are produced in a ratio of 10:1. The kaon is a meson that includes a strange quark and hence decays weakly. The dominant channels are: $K^+ \rightarrow \mu^+ + \nu_\mu$ and $K^- \rightarrow \mu^- + \bar{\nu}_\mu$ (63 %). But also a scenario, although less probable (5 % to 21 %), like the decay into the lighter pions is possible. With a probability of more than 99 % charged pions decay almost exclusively in the muon channel: $\pi^+ \rightarrow \mu^+ + \nu_\mu$ and $\pi^- \rightarrow \mu^- + \bar{\nu}_\mu$ [A$^+$08b].

Electromagnetic showers arise from the decay of a neutral pion in two photons each of which can create a new electron-positron-pair. If this pair is still energy-rich, a photon can be emitted via bremsstrahlung. This procedure repeats itself and stops when the low-energy electrons are not able to emit radiation anymore.

A 1 GeV muon with a Lorentz factor of $\gamma \approx 9.4$ possesses a mean free path of about 6 km and an average decay time of 2.2 μs. Most of the muons do not reach the surface of the earth as they decay into the stable leptons electron or positron via the processes $\mu^- \rightarrow e^- + \bar{\nu}_e + \nu_\mu$ and $\mu^+ \rightarrow e^+ + \nu_e + \bar{\nu}_\mu$ [A$^+$08b]. Although the amount of produced electrons is ten times larger than muons, the occurrence of a muon at sea level is much more probable (see figure 5.3, right panel). The reason for this is the small interaction probability that causes muons to penetrate the atmosphere without considerable disturbance, while electrons are easily absorbed. Hence, the cosmic rays used for data taking are mainly composed of secondary muons.

Scintillation Counters

The trigger used for the test setup consists of an array of scintillation counters. Such a counter is used to detect particles (in this case coming from cosmic rays) and is composed of a scintillation material, an optical waveguide, and a photomultiplier. In general, organic and inorganic scintillation counters are distinguished.

Considering inorganic scintillators as NaI, CsI, or $Bi_4Ge_3O_{12}$, electron-hole pairs are produced by ionization of an incident particle that traverses the scintillation material. The energy liberated by the recombination of these pairs produces radiation inside the visible spectrum. Thereafter, this light signal is transmitted via the optical waveguide to the photodiode of the photomultiplier where electrons are produced by the photoelectric effect. These electrons are multiplied by so-called dynodes to contribute to the signal which is measured afterwards. This signal is proportional to the deposited energy of the original particle. Inorganic scintillators possess an excellent light yield, but a relatively long decay-time[1], which results in an increased insensitivity for incoming particles. The most frequently used inorganic scintillation material is NaI [Ams07].

[1] Doped CsI has a decay time of about 1 μs, pure one has a decay time of about 20 ns [Ams07].

In the case of organic scintillators as NE102A, excited molecule states are created by ionization of the original particle. These states decay by fluorescence. An admixed wavelength shifter then produces light in the visible spectrum which is processed as described above. The excellent features of this scintillator type are the fast decay-time of about 2 ns and the extensive manufacturing possibilities at rather low costs. As inorganic scintillators almost exclusively consist of constituents with small Z, the yields for photons are not optimal [Ams07].

Trigger Setup in the Coincidence Mode

In the standalone mode in Münster only a two-stage trigger system is used (compare to section 4.6.1). The trigger levels in this mode consist of a pretrigger that initiates the MCMs to start with data processing and a Level 1 which asks for a complete readout of raw data. In this context the cosmic trigger adopts the part of the pretrigger and initiates the MCMs if a cosmic traverses the supermodule.

The data used in the subsequent discussion was obtained by using the cosmic trigger in the coincidence mode. Two detector layers with compositions of organic scintillator counters, mechanically stabilized by an aluminum frame, are mounted above and below the supermodule. If these two layers deliver a positive response in a small time window, a signal is sent to the trigger logic of the GTU. At the same time the signal is forwarded to the DCS-Bords of the chambers for triggering the start of data readout in the MCMs. The geometry of the lower trigger layers is optimized so that it covers almost the whole active area of the supermodule. The upper layer covers only one stack. The dimensions of the assembly are sketched in the figures 5.4 and 5.5 [Bat07].

The upper trigger consists of two rows with 20 scintillator stripes (length: 86.4 cm, width: 11 cm, thickness: 2 cm) each arranged with a respective gap of 4 mm side by side in z-direction. The scintillators of the particular rows are mounted head to head including a gap of 1 cm in y-direction. This whole composition works as a single movable unit to cover the desired stack where the data taking shall take place. The active area of this unit is given by 2.20 m $\times$ 2.73 m $\approx$ 6.00 m^2. The lower trigger is stationary and

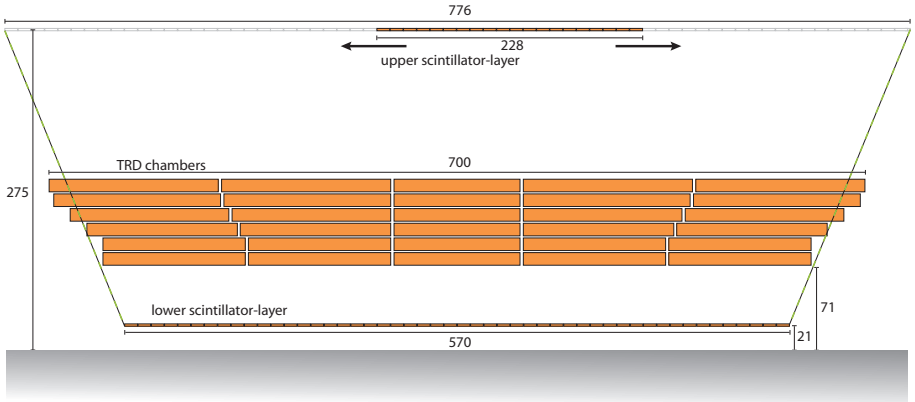

Figure 5.4: *Side view of the TRD-supermodule (x-z-plane, units of cm) [Bat07]. The upper trigger detector layer is movable, the lower one is stationary.*

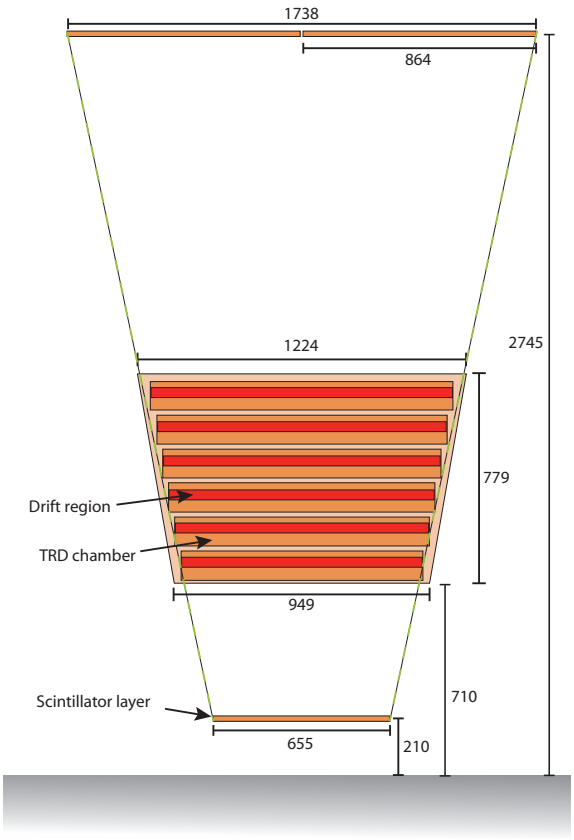

Figure 5.5: *Front view of the TRD-supermodule (x-y-plane, units of cm) [Bat07].*

designed to cover the whole TRD supermodule in z-direction. It is composed of one row of 50 scintillator stripes (length: 65.5 cm, width: 11 cm, thickness: 2 cm) and covers an active area of 5.70 m $\times$ 0.66 m $\approx$ 3.80 m^2 [Bat07].

The organic scintillators (see above) are composed of Polystyrol with 2 % of ParaTerphenyl serving as the primary florescence medium and 0.03 % of Diphenyloxazolylbenzol to perform the wave shifting. Furthermore, an optical gel is added to connect the scintillator stripes and the attached photomultiplier in order to minimize light loss [Bat07].

5.1.3 Settings of the GTU

As a trigger detector the TRD is intended to search for high p_t electrons and electron-positron pairs. To receive the crucial information about an event at an early stage after the collision, calculations are made already during the data taking to gather track properties. This important procedure is called online tracking.

The first level of the online tracking procedure is the tracklet calculation in the TRAP-Chip (see section 5.2.2). These tracklets include all significant information for further calculations: the y-position, the z-position (padrow), the deflection with respect to the y-direction and a measure of the electron probability (PID). However, they are not sufficient for the final trigger decision. As described in section 4.6.3 the tracklet information is sent via the ORIs to the GTU where the data is used to match the tracklets of one

stack to form a track. For this, all tracklets are projected to a virtual y-z-plane with the help of the positions and deflection angles that have been calculated in the MCMs using a primary vertex assumption. If the number of tracklets, which are found in a 2-d window of pre-defined size, exceeds a certain threshold[2], they are assigned to a track that is calculated by a straight line fit through all detected tracklets. Based on the deflection due to the Lorentz force, that originates from the external magnetic field of the L3 magnet, the value of the transverse momentum can be calculated.
In Münster the task of the GTU is somewhat less sophisticated. There are two different operating modes to distinguish: in the first place only the lower cosmic trigger can be used as a pretrigger. In this case the GTU accepts each event containing more than four tracklets in one stack. Second, the trigger can be operated in the coincidence mode to initiate the pretrigger signal. In the latter case each pretrigger signal is accepted by the GTU in order to demand for the complete readout of raw data. This mode is used for the data analysis in this thesis as it ensures both, a sufficient amount of tracklets and a high probability that the calculated tracklets belong to a particle track.

5.2 Online Tracking Procedure

After the pre-amplifying and shaping by the PASA the analog signal of each MCM channel is forwarded to one or two of the ADCs where it is digitized. The filtered data is written to an event buffer and meanwhile processed by the TPP. Then four CPUs calculate the tracklets which are subsequently shipped to the readout network interface of the TRAP chip. From this point they are sent to the readout tree (see section 4.6.3).

5.2.1 Filter Procedure of the Signal

Before the tracklets are processed the shaped and pre-amplified signal has to be filtered. The pathway of the signal can be described by a mapping A created by a series connection of mappings F, which each symbolizes a deterioration of the incoming signal, and the desired value G_{PRF} for the PRF [Gut02]:

$$A = F_{\mathrm{Nonlinear}} \circ F_{\mathrm{Pedestal}} \circ F_{\mathrm{Gain}} \circ F_{\mathrm{Tail}} \circ F_{\mathrm{Crosstalk}} \circ G_{\mathrm{PRF}} \tag{5.1}$$

In order to calculate the PRF in the TPP a filter mapping D has to be utilized:

$$G_{\mathrm{PRF}} = D \circ A \tag{5.2}$$

with

$$D = F^{-1}_{\mathrm{Crosstalk}} \circ F^{-1}_{\mathrm{Tail}} \circ F^{-1}_{\mathrm{Gain}} \circ F^{-1}_{\mathrm{Pedestal}} \circ F^{-1}_{\mathrm{Nonlinear}} \tag{5.3}$$

$F_{\mathrm{Nonlinear}}$ results from the non-linearities of the electronics and the signal amplification. The greater part comes from the PASA and can be corrected by systematically filled **L**ook **U**p **T**ables (LUTs)[3]. F_{Pedestal} stands for possible signal fluctuations. The pedestal filter

[2] Usually four tracklets are required.

[3] The LUTs play an important part in the management of accessible MCM registers. They carry crucial information, e.g. about the PID, the PRF, or the gain factor. They can be accessed during the signal processing.

determines the current baseline of one single channel, subtracts it, and adds a common pedestal value[4] to ensure a polarity aware signal. F_{Gain} is a deterioration caused by fluctuations of the signal gain due to anode wire sag, inhomogeneities of the high voltage as well as of the ambient pressure, and in particular due to the slightly different amplification factors of the PASA and ADC. It is corrected by the investigation of the dE/dx spectrum in an offline analysis [Alb10]. F_{Tail} is corrected by the tail cancellation filter. It considers the time-induced signals that consist of a fast increasing part and a long tail because of slowly moving positive ions. This long ion tail interferes with the signal in subsequent timebins and therefore causes considerable and continuous disturbance of the time resolution. $F_{\text{Crosstalk}}$ is a source of error that originates from the not neglectable capacity of the cathode pad with respect to its neighbors. With an average pad area of about 6 cm^2 the capacity has a value of $\approx$ 20 to 25 pF, which leads to mutual signal induction [Gut02].

The serialized filter D corrects all these deteriorations to improve the quality of the signal. D is designed in a way to consecutively apply the filters, but it also offers the possibility to bypass a filter in order to continue with the next filter step. This procedure contributes to a more variable system.

5.2.2 Tracklet Calculation in the TRAP-Chip

After the filter procedure the data is sent to the TPP where the parametrization of track segments proceeds. The TPP (see Figure 5.6) is composed of a 'Hit-Detection-Unit', a 'Hit-Selection-Unit', four arithmetic units and a **F**it-**R**egister-**F**ile (FRF). The FRF consists itself of four independent read-modify-write ports with a size of 19x119 bits [Gut06].

The Hit-Detection-Unit searches for possible hits - an induced signal on adjacent pads in one timebin. To accept a hit on a given pad two conditions have to be fulfilled: At first the charge Q of channel i in timebin tb must be a local maximum in comparison to its two neighbor pads (see equation 5.4). Moreover, the total charge induced on these three pads has to exceed a defined threshold T_H (see equation 5.5).

$$Q_i(tb) > Q_{i+1}(tb) \qquad \text{and} \qquad Q_i(tb) \geq Q_{i-1}(tb) \tag{5.4}$$

$$Q_{tot} = Q_i(tb) + Q_{i+i}(tb) + Q_{i-1}(tb) \geq \text{T}_\text{H} \tag{5.5}$$

The hit detection is identical for all inner channels except for the borders. These channels only exist to be compared with border channels of neighbor MCMs. The Hit-Selection-Unit marks the detected hits to be sorted, where the maximum number is limited to four per MCM[5]. In the case of more than four found hits they are sorted by their total charge. The hits with the largest total accumulated charges are selected. The values i, $Q_i(tb)$, $Q_{i+1}(tb)$, $Q_{i-1}(tb)$, and $Q_{\text{tot}}(tb)$ of the four hits are forwarded to the four arithmetic units where the fit parameters for a straight line fit of the form $y = ax + b$ are prepared. The TPP calculates the following sums [A$^+$05]:

[4] Usually this value is 10 ADC units.

[5] Reasonable results are only possible for values that do not exceed a value of 6 because of overlapping hits.

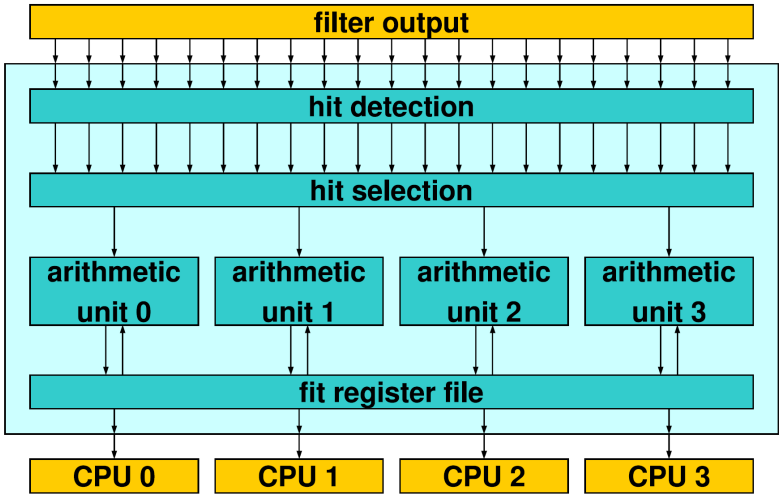

Figure 5.6: *Scheme of the TPP. The filtered data is sent to the TPP where hits are detected, selected, and forwarded to four arithmetic units. Fit parameters are calculated and stored in the FRFs to be accessible for the TRAP which performs a straight line fit based on this data [Gut06].*

$$X = \sum_{n=1}^{N} x_n \qquad Y = \sum_{n=1}^{N} y_n \qquad XY = \sum_{n=1}^{N} x_n y_n \tag{5.6}$$
$$X^2 = \sum_{n=1}^{N} x_n^2 \qquad Y^2 = \sum_{n=1}^{N} y_n^2 \qquad N = \sum_{n=1}^{N} 1$$

N is the number of hits found in the related channel during the period of 30 timebins. x_n and y_n are the positions with respect to the local coordinate system in the particular timebin. Due to the simple dependence on time, x_n can be calculated by the formula $x = v_{\text{drift}} \cdot t$ as long as the drift velocity[6] is known. The calculation of y_n is more complicated and accomplished by using the PRF to obtain a resolution better than imposed by the pad width. In order to determine y_n, the TPP calculates the value

$$\overline{COG} = \frac{Q_{i+1} - Q_{i-1}}{Q_i} \tag{5.7}$$

which differs only systematically from the theoretically predicted shape of the PRF. Parameters stored in the LUTs correct the systematic deviations so that y_n can be obtained by:

$$y_n = \overline{\text{COG}}_n + \text{LUT}(\text{COG}_n) \tag{5.8}$$

The tuple (x,y) calculated in consecutive timebins by this procedure is termed cluster from now on. After the sums are shifted to the FRF a last verification concerning possible tracklet candidates ascribed to the channels i and i+1 is done by:

$$N_i \geq \text{TPCL} \tag{5.9}$$

[6] v_{drift} depends on the gas mixture and the voltage applied to the drift region.

$$N_{i+1} + N_i \geq \text{TPCT} \tag{5.10}$$

TPCL and TPCT are cluster thresholds. They are described in detail in section 6.2.4. Equation 5.9 requires that the clusters found in channel i exceed a threshold TPCL. Equation 5.10 requires that the sum of the clusters found in channels i and $i+1$ exceeds another threshold TPCT. If these conditions are fulfilled, the calculation proceeds. The fit sums in the FRF are accessible by the four CPUs of the TRAP and used to perform a straight line fit to get the parameters a and b by calculating[7] [Gut06] :

$$a = \frac{N \cdot xy - xy}{Nx^2 - xy} \tag{5.11}$$

$$b = \frac{N^2 y - x^2 y}{Nx^2 - xy} \tag{5.12}$$

These values parameterize a straight line and they are stored in the FRF.

5.2.3 Tracklet Word

After the linear regression two values are obtained and stored in a data word named tracklet word. In the first place this is the y-coordinate of the intersection point between the straight line taken from the FRF and the the top of the drift chamber[8]. Second, the deflection dy which is extracted from the slope $\frac{dy}{dx}$ of the straight line fit. This slope can be directly turned into the deflection dy due to the constant drift length of $dx_{\text{drift}} = 3$ cm (see figure 5.7).

Before adding dy to the tracklet word some corrections have to be made by the assembler program that runs on the CPUs. As the B-field coincides with the beam axis and the E-field points to the direction of the drifting electrons (x-direction), the Lorentz force leads to a deflection of the secondary electrons in y-direction dy_{Lorentz}. In the current setup of the ALICE experiment an angle of $\Psi_L = 7°$ is expected. As introduced in section 4.5.4 the pads are slightly tilted in opposite direction for consecutive layers. By a projection to the primary vertex (see section 8.1.1) the correction for the pad tilting dy_{tilt} is obtained so that the new value $dy' = dy + dy_{\text{Lorentz}} + dy_{\text{tilt}}$ is stored in the tracklet word [dC03].

The precision of y directly affects the accuracy of measurements for the transverse momentum p_t. The granularity of the y-position in the tracklet word is chosen to be $1/160\mu$m with a total range of -643.2 mm $\leq y \leq$ 643.2 mm for all layers. This value is stored with a size of 13 bits in the tracklet word. The deflection dy is stored with a size of 7 bits and a granularity of $1/140\mu$m including a range of -8.8 mm $\leq dy \leq$ 8.8 mm. Moreover, the z-position and the electron PID are stored. The z-position is known from the padrow of the detected hit, stored with a size of 4 bits, and a maximum range of $0 \leq z \leq 15$ padrows. The PID is obtained by two independent charge measurements in the TPP. It is stored with a size of 8 bits and a range from 0 % to 100 %. Taking all these values into consideration, the tracklet word comprises a size of 32 bits [dC03]. In addition to the values stored in the tracklet word the detector (stack and layer) of the found tracklet is known.

[7] This calculation is an approximation with regard to straight line tracks.

[8] In chapter 7 it is shown that the exact reference plane of online tracklets is located about 3.3 mm above the padplane.

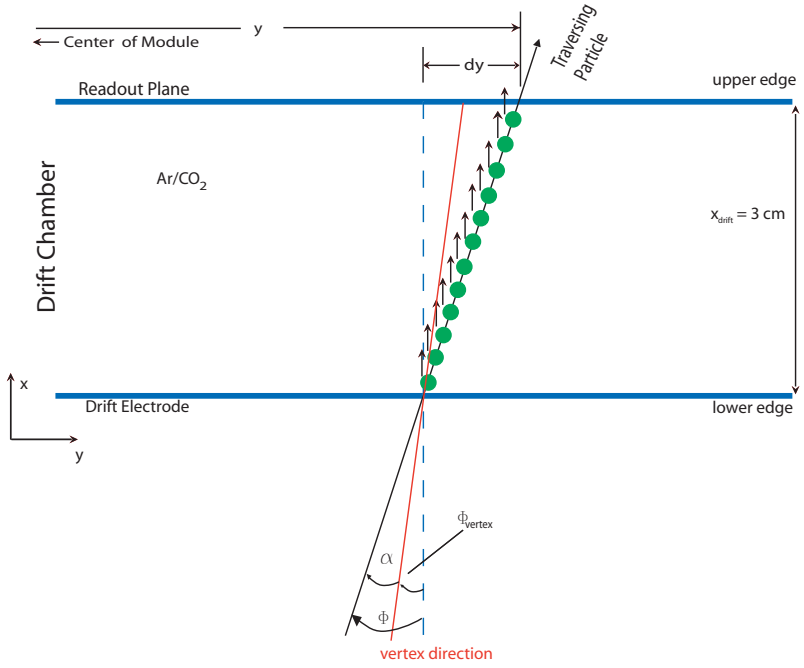

Figure 5.7: *A particle traverses the drift region. Its intersection point with the upper part of the chamber defines the local y-position. The difference between the y-coordinates with respect to the top and the bottom of the chamber defines the deflection dy.*

This information can implicitly obtained by the related TMU receiving the data. Table 5.1 summarizes all values written to the tracklet word. The distributions in figure 5.8 visualize y and dy for the setup in Münster.

For the trigger decision the first cut on the transverse momentum is done by the MCM. Instead of p_t, a maximum deflection angle $\alpha_{\max}$ is calculated based on a given threshold $p_t^{\min}$:

$$\alpha_{\max} = \arcsin\left(\frac{e \cdot r \cdot B}{2 \cdot p_t^{\min}}\right) \tag{5.13}$$

The default value for $p_t^{\min}$ is chosen to be 2.3 GeV/c. r describes the radius with respect to the vertex, e stands for the electromagnetic charge and B denotes the external magnetic field. The angle $\alpha_{\max}$ is transformed into a deflection $dy_{\min}$ and $dy_{\max}$ in order to compare it with the deflection dy'. The deflection angle α of the tracklet is measured with respect to the vertex direction. For resolution measurements in this analysis the angle ϕ as defined in figure 5.7 is used. With the definition of angles in this sketch, α can be expressed by:

$$\alpha = \phi - \phi_{\text{vertex}} = \arctan\left(\frac{dy}{dx}\right) - \phi_{vertex} \tag{5.14}$$

so that the minimum and maximum deflection is calculated by:

$$\begin{aligned} dy_{\min} &= dx_{\text{drift}} \cdot \tan\left(\phi_{\text{vertex}} - \alpha_{\max}\right) \\ dy_{\max} &= dx_{\text{drift}} \cdot \tan\left(\phi_{\text{vertex}} + \alpha_{\max}\right) \end{aligned} \tag{5.15}$$

Symbol	Granularity	Size	Range
y	1/160μm	13 bits	-643.2 ... 643.2 mm
dy	1/140μm	7 bits	-8.8 ... 8.8 mm
z	1	4 bits	0 ... 15 padrows
PID	1/39%	8 bits	0 ... 100 %

Table 5.1: *Contents of the tracklet word.*

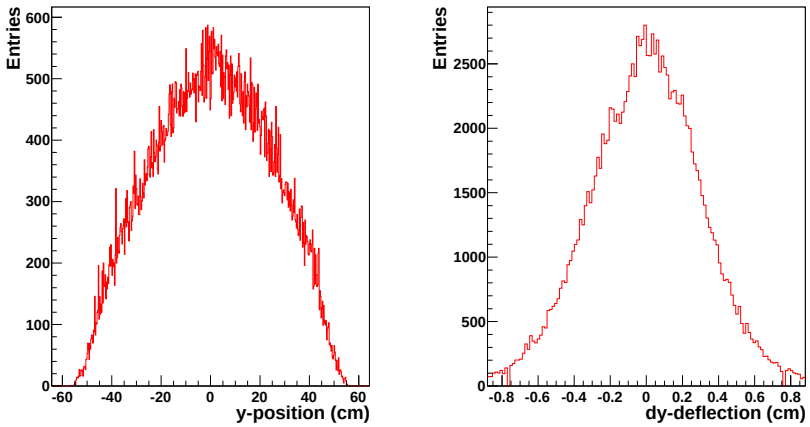

Figure 5.8: *The distribution of y (left panel) and dy (right panel) created within a cosmic run of $2 \cdot 10^4$ events at Münster. Due to the small acceptance of the cosmic trigger in y-direction the entries are distributed around zero.*

For more information about this formula see [dC03]. These calculations proceed during the configuration of the MCMs and the values $dy_{\min}$ and $dy_{\max}$ are stored in the LUT. If $dy_{\min} \leq dy' \leq dy_{\max}$, the tracklet word is forwarded to the GTU. The unit which made these calculations contributes to the overall tracking procedure of the GTU. Therefore, it is often termed a **L**ocal **T**racking **U**nit (LTU) [dC03].

It is important for both, the p_t estimation in the LTUs and the further calculations in the GTU, which depend on the performance of the LTUs, that the values y and dy have a sufficient resolution to ensure the TRD's capability as a trigger detector.

5.2.4 Online Tracklet Simulation

For a reasonable track calculation the GTU requires at least four tracklets. In the construction phase of the supermodules in Münster the precondition of four installed layers is only partially fulfilled. Additionally, the data taking with an appropriate amount of statistics causes a considerable expenditure of time. To be more flexible it is possible to simulate the MCM on the stored raw data. The simulation comprises the filter, the TPP, and the TRAP. It offers the possibility to adjust filter and TPP parameters with a remarkable saving of time, although the data has already been taken. When Monte Carlo data is used for the analysis as well, the MCM simulator is the only possibility to obtain the online tracking information.

Filter Type	Register	Explanation	Value
Nonlinear	FLBY	Nonlinearity Bypass	0
Pedestal	FPBY	Pedestal Bypass	1
	FPNP	Common Additive	$4 \cdot 10$
Gain	FGBY	Gain Bypass	0
Tail Cancellation	FTBY	Tail Cancellation Bypass	0
Crosstalk	FCBY	Crosstalk Bypass	1
	FCW 1-5	Filter Weight 1-5	0

Table 5.2: *Default values of filter parameters.*

Register Type	Register	Explanation	Value
Selection & Detection	TPHT	Hit Threshold	$4 \cdot 60$
Arithmetic Unit	TPFS	Linear Fit Start	8
	TPFE	Linear Fit End	25
	TPQS0	Charge Accumulator 0 Start	0
	TPQE0	Charge Accumulator 0 End	8
	TPQS1	Charge Accumulator 1 Start	8
	TPQE1	Charge Accumulator 1 End	25
	TPVBY	Cluster Verification Bypass	0
	TPVT	Cluster Quality Threshold	0
	TPFP	Filtered Pedestal	$4 \cdot 10$
Fit Register File	TPCL	Left Cluster Threshold	1
	TPCT	Total Cluster Threshold	8

Table 5.3: *Default parameters of the TPP.*

5.2.5 Default Values in the TPP and Filter

The MCM has a large amount of registers which have to be set for data taking. In the following the relevant registers in the context of this thesis are briefly presented. The default values for the TPP and the filter unit are depicted in table 5.2 and 5.3. The values correspond to the parameters which were set during the data taking in Münster. These settings are used for data analysis initially. In table 5.2, the registers that are marked with the letters 'BY' stand for a bypass. This simply implies to skip the corresponding filter in order to proceed with the next one. As can be seen from this listing, the pedestal filter is the only one that is applied in the default settings. Indeed, the crosstalk filter is not bypassed, but the five available weights are all set to zero. The pedestal value is set to 10, where the pre-factor 4 considers the fact that the TRAPs internally calculate with a higher precision of two additional digits. For the filters which are bypassed additional parameters are not shown as these filters are not used in this setting anyway. In section

8.2 settings for the tail cancellation filter will be applied to investigate the influence on the position and angular resolution. A detailed discussion and description of the additional tail cancellation parameters is given in that section.

In table 5.3 the registers are ordered by the respective subunit of the TPP. The value TPHT is the threshold defined in equation 5.5 and it is a tool to locate a hit. The next registers that are presented all concern the arithmetic units. TPFS and TPFE describe the time window in which the linear fit through the calculated clusters is performed. To find a reasonable fit window the drift velocity has to be known. It can be determined by the pulse height plot as described in section 6.2.1. The four charge accumulators of the arithmetic unit are of minor importance for the online tracking resolution and efficiency, but they are required to determine the electron PID. The parameter TPVT stands for a quality measure of the detected hits and it is implemented by the following formula:

$$\frac{Q_{i-1}(t) \cdot Q_{i+1}(t)}{Q_i^2(t)} \leq T_Q, \tag{5.16}$$

With its activation this value is used to detect and sort out hits produced by two or more overlapping signals that actually do not belong to the same particle. As can be inferred from table 5.3 this quality measure is bypassed.

Equation 5.7 is only valid for a zero pedestal value. As parts of the filter procedures, as e.g. the tail cancellation filter, modify the initially set pedestal value a filtered pedestal has to be determined. Actually, the goal for the final pedestal value at the endpoint of the processing chain is a value of 10 ADC units just like the initially set pedestal. Therefore, a value for the register FPNP has to be found previously so that after the filter procedure the original value is obtained. Another possibility would be to use the filtered pedestal register TPFP to add the correct pedestal after the filtering. This is a difficult task as the automatization to find these values dependents on the choice of other activated filters.

The two registers TPCL and TPCT are used to assign a tracklet candidate to the related channel. They will play an important role in the determination of the efficiency of the online tracking procedure. After the calculation of the tuples (x,y) and before the straight line fit is performed, it is checked whether the channel i and its left neighbor i+1 exceed a certain threshold TPCT and whether the channel i+1 for its own exceeds a threshold TPCL of detected hits. For the selection of these values a compromise has to be found to have neither too little tracklets nor tracklet splitting (see chapter 6).

5.3 The Access of Data

One part of the subsequent analysis is based on data taken from cosmic runs of supermodule VII using the coincidence trigger placed above stack 3. The assembly was finished in July 2009 and the complete supermodule was sent to CERN afterwards.

The common chain to access the data starts with a raw data stream which comprises all important information gathered during the data taking. This stream is stored by the DAQ-system in the `root` format and has to be reconstructed with Aliroot. The reconstruction delivers new `root` files such as `AliESDs.root`, `TRDTracklets.root`, and `TRDDigits.root` which are used for the analysis.

ESD stands for **E**vent **S**ummary **D**ata and contains information about the reconstructed tracks and the corresponding offline tracklets. These tracks describe the trajectory of a particle in space with the help of 5 parameters and a corresponding covariance matrix. Further track information like detector clusters can be obtained from the `AliESDfriends.root` file. The `TRDTracklets.root` file contains all necessary information for the online tracklet analysis. In the case of hardware MCMs the class `AliTRDtrackletWord` provides access to all values stored in the data word. The file `TRDDigits.root` includes digitized signals measured by the readout pads. It is the starting point for the analysis with the MCM simulator. By simulations of the MCM via the class `AliTRDmcmSim`, online tracklets are processed and stored in the same `TRDtracklets.root` file as mentioned above. Finally, using the class `AliTRDtrackletMCM` allows to extract the values stored in the tracklet word based on MCM simulations [roo10]. Figure 5.9 schematically shows the process of data-access.

As it is shown below the procedure using cosmic rays is not sufficient to investigate the online tracking performance of the TRD precisely. Therefore, Monte Carlo information is used, too. Nevertheless, the way of data access and production does not change substantially. Using Monte Carlo data the files `TRDtracklets.root` and `TRDDigits.root` are created within the simulation. A subsequent reconstruction will then produce the ESD file. The analysis chain then proceeds identically as sketched in figure 5.9.

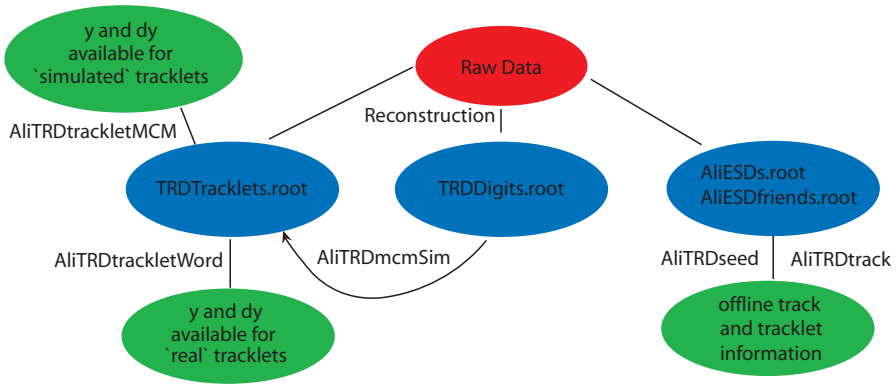

Figure 5.9: *Chain to obtain the tracklet information. Starting from the raw data it is possible to retrieve tracklets from the hardware MCMs, from MCM simulations using real data, and from offline reconstruction. In addition, Monte Carlo data can easily be embedded in this chain.*

6. Online Tracking Efficiency

For the TRD's purpose as a trigger detector an appropriate efficiency of online tracklet reconstruction, which is the starting point of the L1 decision, is absolutely necessary. In this chapter a method is developed to obtain the efficiency of the online tracking procedure by using cosmic rays. This efficiency is then optimized by adjusting some MCM parameters. Instead of relying on calculations of hardware MCMs, for simplicity reasons, the MCM simulator is used exclusively since some parameters of the TPP have to be adjusted continuously throughout the subsequent analysis. Initially, the default parameters are used as introduced in section 5.2.5.

Section 6.1 describes tracklet properties at the beginning of the analysis and shows the progress after correcting some mistakes. In section 6.2 the efficiency is determined. First, the fit range has to be adjusted in order to correspond to the results of the pulse height plot (section 6.2.1). Thereafter, the method to determine the efficiency of single detectors in stack 3 is presented (section 6.2.2). This efficiency is optimized by a review of the hit threshold TPHT and the cluster thresholds TPCL and TPCT (sections 6.2.3 and 6.2.4).

The data used in this chapter was taken in coincidence mode within the cosmic run 2249 using the configuration `cf_p_zs-s16n_tb30_trk-p0b0.4l0d9_mstrg` version r3072-01. The parameters describing this configuration are summarized in table 6.1. The upper trigger was placed above stack 3. The data was taken in the coincidence mode using supermodule VII. The voltage was chosen to be 1500 V for both, drift and anode. The reconstruction was done with Aliroot version `v4-17-Rev-09`. In order to be up to date continuously, the special version based on Aliroot HEAD (development version as of 18. 6. 2009) was used for MCM simulations since the class `AliTRDmcmSim` had to be changed and improved quite often during the writing of this thesis. These modifications were committed in the latest Aliroot versions.

6.1 First Visualization of Online Tracklets

In this thesis the nature of online tracklets based on 'real' detector data is explored. Lot of work was necessary to establish the online tracking procedure in order to get the tracklets ready for a statistical analysis which provides reasonable physical results. At the starting point this was not the case at all. A first attempt to visualize the online tracklets using the Alieve event display is illustrated in figure 6.1 (left panel). This is one representative event which shows the problems that occurred at the beginning. The yellow dots stand for the trace of reconstructed clusters that visualize the path of the traversed cosmic ray. The red lines correspond to online tracklets found in the respective detectors. The positions and angles of the tracklets strongly differ from those of the clusters and they seem to have nothing in common with the depicted track. The first task was to locate the mistakes and to correct them since in this condition a study of tracklet properties with much statistics was futile. Therefore, single events were scanned to get a feeling of what went wrong.

With regard to the left part of figure 6.1 a first noticeable fact is the erroneous angular distribution as none of the tracklets points into the direction of the clusters. With a

Abbreviation	Meaning	Value
cfg	configuration	/
p	pedestal	10
zs-	settings for zero suppression	/
s	single threshold for zero suppression	16
n	neighbor pads are read out for zero suppression	/
tb	timebins to be read out	30
trk-	settings for tracklets	/
p	p_t threshold	0
b	external B-field	0.4
l	Lorentz angle	0
d	timebins of the drift time	9
mstrg	Münster trigger	/

Table 6.1: *Overview of the abbreviations used in the configuration file.*

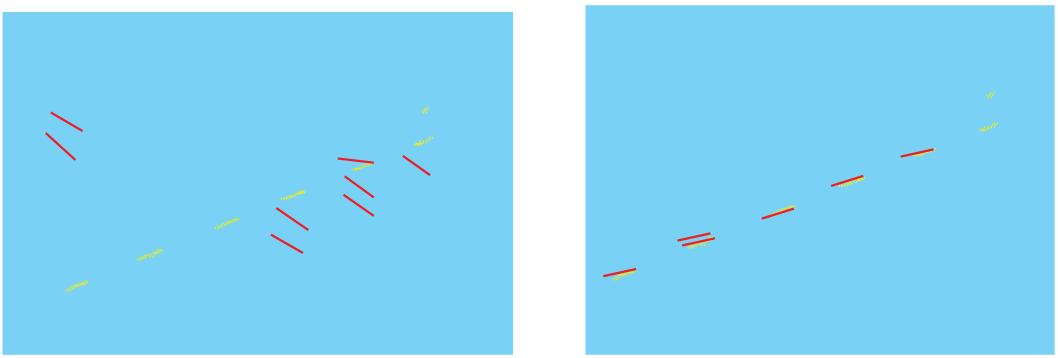

Figure 6.1: *Visualization of online tracklets with Alieve. Left panel: the starting point, right panel: situation after debugging.*

closer look it becomes obvious that all tracklets more or less point in the same wrong direction. After a study of many of these pictures in Alieve, only rare events showed the correct angular distribution which corresponded to that of the clusters. This error could be traced back to an overflow in a MCM register and occurred due to the limited size of the bit word for the deflection *dy* (7 bit; see section 5.2.3). Depending on the chosen number of timebins that corresponds to the drift time, the tracklets are either too steep or too flat. In this context steep tracklets correspond to a small angle interval of about $|\phi| < 10°$. The term 'flat' applies to tracklet angles which lie outside this region. The drift time can be set in a MCM register (see section 8.1.2). The default value of this register was 25 timebins which corresponds to a small drift velocity and flat tracklets. Since there was no initial cut done on tracklets with large incident angles the deflection was calculated and stored in the data word though in many cases it was too large for the 7 bit. Consequently, the deflection was cut down to the size of the tracklet word as only the lower 7 bits were

used and the original information of the tracklet slope got lost. As a result, the incorrect and uniform angular distribution was created. In case the tracklets were steep enough to match the tracklet word the correct angle was calculated. This corresponds to the rare events mentioned above. To correct these influences a cut was established that sorts out all tracklets with an angle exceeding a certain threshold[1]. In order to receive sufficient amount of tracklets during data taking the number of timebins was set to a small value of 9. This contributes to steep tracklets and does not influence the efficiency procedure and the calculation of the position resolution developed in chapter 7. For the determination of the angular resolution in chapter 8 the correct drift velocity had to be found.

Another mistake occurred in the assignment of the correct y-position inside the MCM. Due to a transfer of the calculation concerning the y-offset positions to the TRAPs[2] there was a shift of half a pad width which could be corrected quickly. Moreover, a convention about the sign of the deflection dy had to be established in the TRAP as the definition of the deflection dy introduced in figure 5.7 is not unambiguous [Kle09].

In the subsequent sections a problem called 'tracklet splitting' is discussed. Due to wrongly set parameters in the TPP the tracklet information can be calculated twice for a single hit. The registers TPCL and TPCT are parameters to control the splitting. Based on the experience with the Alieve visualization the parameter setup was adjusted to be TPCL = 4 and TPCT = 12 initially, in order to suppress the splitting. The discussion about this topic proceeds in the following sections as it is fundamental for the determination of the efficiency. It is intended to find an appropriate compromise that ensures both, as little tracklet splitting as possible and sufficient efficiency of found tracklets.

The right panel of figure 6.1 shows the same event after the correction of the mistakes outlined above. This is the starting point of a statistical analysis of tracklet properties. The tracklets now describe the clusters quite well, though tracklet splitting still occurs (layer 1). A consequence of the new parameters is that sometimes tracklets are not detected anymore as it is shown in layer 5.

6.2 Determination of the Efficiency

6.2.1 MCM Simulator

For the results in this chapter, the MCM simulator has been used for the first time. Figure 6.2 (left panel) visualizes the tracklet calculation in the TRAP as described in section 5.2.2. As can be seen from this picture the charge is deposited via a 2-pad-cluster on the channels 1 and 2. This allows to calculate the precise positions using the PRF due to charge sharing. The star symbols show the positions calculated for each timebin by this method. With the largest charge deposition channel 2 is identified as the local maximum, see equation 5.4. In case the sum of the 3 channels 1, 2, 3 (calculated timebin-wise) exceeds the threshold of 60 ADC values the precise cluster position is calculated. Actually, the default parameter for TPHT is 240 but due to the two additional digits of the four CPUs (see section 5.2.5) this value has to be divided by four. As the number of

[1] By default this threshold is about 10°.

[2] The offset is now calculated by the positions stored in a MCM register. Initially, the y-position calculation is done internally and afterwards corrected by this offset.

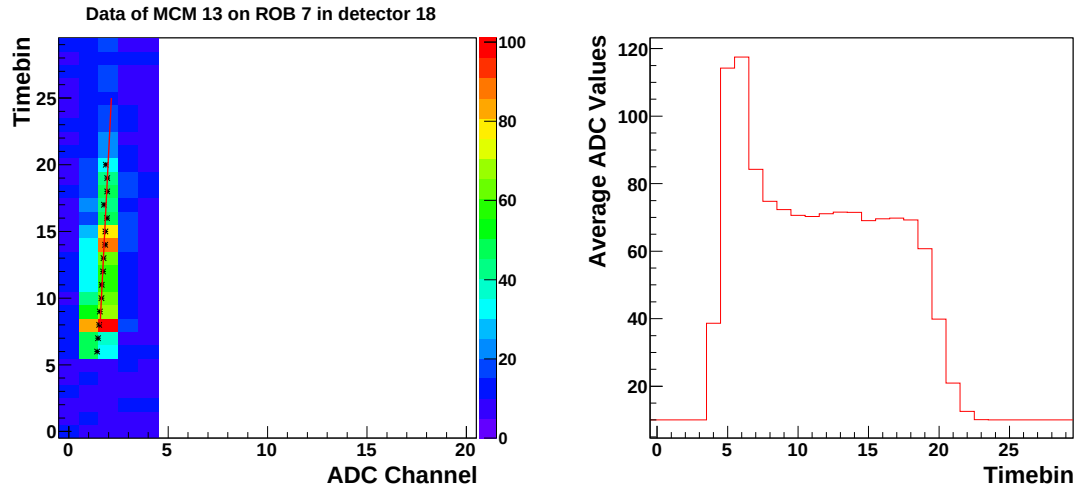

Figure 6.2: *Signal formation. Left panel: 2-d visualization of the data taking in the MCM, right panel: the pulse height plot ($2 \cdot 10^4$ events) shows that the fit range is not optimal.*

found clusters exceeds the standard values of both, TPCL = 4 and TPCT = 12, the fit can be performed. The red line depicts the tracklet which is calculated on the basis of the cluster positions.

In the right panel of this figure the pulse height plot (see section 4.5.4) is shown. It is obtained by superposing several of the 2-d plots as depicted in the histogram to the left. A subsequent projection to the time axis of the particular ADC channels where the hits were found then delivers the plot. It shows that the current fit range (TPFS = 8, TPFE = 25) as introduced in table 5.3 does not coincide with the start and end point of the drift region. In this plot the amplification peak already starts at timebin 4 or 5. The drift region starts around timebin 7 or 8 and its end is approximately reached at timebin 18.[3] For further calculations the MCM parameters of the fit range are chosen to be TPFS = 7 and TPFE = 18. In doing so, the drift time is reduced to eleven timebins. Thus, the threshold TPCT has to be adjusted, because otherwise no tracklets will be found anymore. The new value is chosen to be TPCT = 10. With this initial parameter setup the method to determine the efficiency is described in the next section.

6.2.2 The Method

A simple way to examine the efficiency of online tracklets as a function of the layer number is described in this section. As introduced at the beginning of this chapter the efficiency measurement concentrates on stack 3. To simplify matters the detectors of this stack are termed by their global TRD detector number. Table 6.2 summarizes these numbers of stack 3.

[3] To issue a clear statement about the beginning of the drift region is quite difficult as this area is superimposed by the ion tail of the amplification peak.

Layer:	L0	L1	L2	L3	L4	L5
Global Detector Number:	18	19	20	21	22	23

Table 6.2: *Global detector numbers for stack 3 of the supermodule inserted in slot 00.*

As an example to obtain the efficiency of detector 18, it is initially checked whether the detectors 19 to 23 found a tracklet. If this is true it is ensured that with high probability the tracklets belong to a particle track. Subsequently, the number of tracklets found in detector 18 is determined and stored. The same procedure applies to the other layers of stack 3. Figure 6.3 shows the results of this efficiency method for different detectors. The plots show the distribution of $\mathrm{NoT_A}$ that denotes the number of tracklets found in the particular detector, for which the efficiency shall be determined. This quantity is normalized to the number of accepted events, where an event is only accepted in case of a positive response from all other detectors. Otherwise the efficiency measurement is stopped in order to proceed with the next event. $\mathrm{NoT_A} = 0$ means no tracklet was detected in the particular detector though all other detectors in stack 3 found one. In the further discussion this case is called tracklet **loss**. In case $\mathrm{NoT_A}$ corresponds to 1, the respective detector found one tracklet just exactly like the others. For this number the term **efficiency** is used from now on. Two tracklets appear because of tracklet splitting and noisy pads which have fired by accident during the event. In the subsequent discussion the expression **splitting** stands for $\mathrm{NoT_A} = 2$. Values like $\mathrm{NoT_A} = 3$ or higher can almost

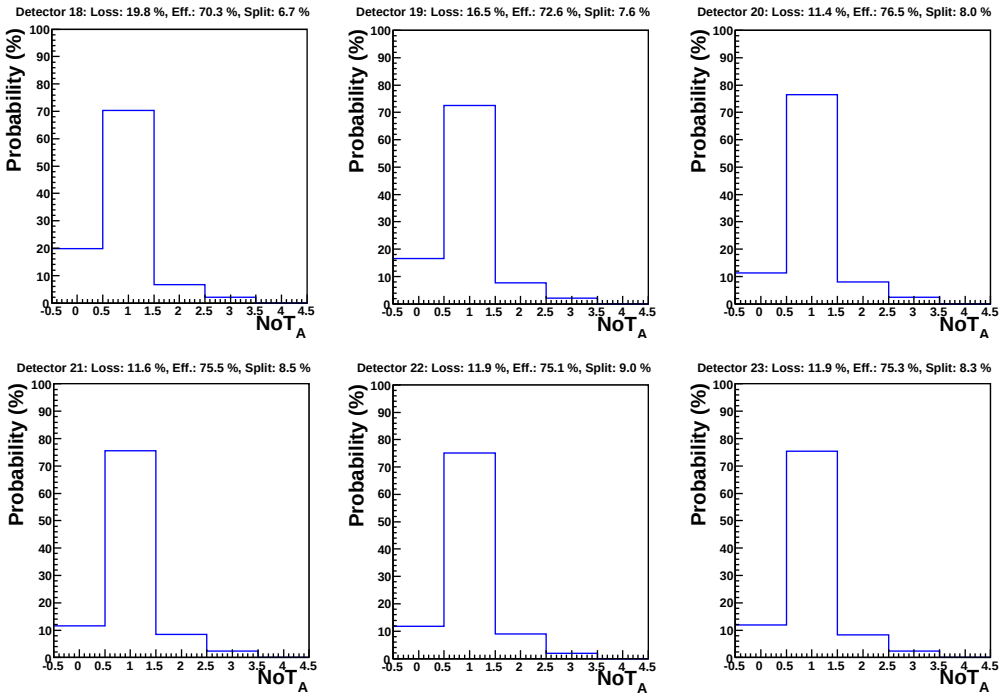

Figure 6.3: *Efficiency plots for different detectors. They give an overview about the loss, the efficiency and the splitting of tracklets. The quantity NoT_A denotes the number of tracklets found in the particular detector normalized to the number of accepted events.*

exclusively be attributed to noisy events. The occurrence of them is below 2 % of accepted events.

The tracklet loss is below 12 % for the upper detectors 20 to 23. Detectors 18 and 19 have much larger loss factors. For the upper detectors the efficiency is about 75 %, for the detectors 18 and 19 it is less. The splitting factor is distributed between 6 % and 9 % for all detectors. In case of adding this part to the efficiency the upper detectors would reach an overall efficiency above 80 %. In section 6.2.4 the validity to combine splitting and efficiency is discussed. In this context it is interesting to find out the ratio of real splitting to noise in events with two found tracklets. Moreover, the question arises in what way these split tracklets impact the analyses .

The behavior of the efficiency shown in figure 6.3 is just as expected in the cosmic setup. Due to the method proposed above the innermost detectors are more efficient than the outer ones. In the case of an inner detector the track cannot 'escape' to the neighbor stack as it is ensured that the particle was measured in the upper and lower layers of the current stack. Contrary to this, the track would be able to leave the stack after traversing either the detectors 23 to 19 or 22 to 18 so that respectively the detectors 18 and 23 cannot detect it. As the efficiency method is confined to stack 3 tracklets that have possibly appeared in layer 0 or 5 of the neighbor stacks are not considered. This is a first explanation for the smaller efficiency of the lower detectors. Furthermore, it is noticeable that the loss factor of detector 18 exceeds the one of detector 23 by about 8 %. This deviation can be explained by the properties of the cosmic setup. Considering the fact that a cosmic is detected by the upper cosmic trigger and traverses all detectors in stack 3 except detector 18 (escape in neighbor stack), it is likely that the particle is also detected by the lower cosmic trigger because of its large acceptance in z (see section 5.1.2). In case the particle traverses detectors 22 to 18 but escapes from 23 it is less probable that it is detected by the upper trigger. This is because of the movable device which has a rather small acceptance in z. Consequently, the event is not recorded. Therefore, the efficiency of detector 23 seems to be better than it would be with an upper cosmic trigger that has the same acceptance as the lower one. Moreover, the loss factor of detector 19 is larger than the one of the other inner layers. In case a particle traverses detectors 23 to 20, then escapes to one of the neighbor stacks and additionally a noisy event is created in layer 18 by accident, the tracklet in detector 19 would be marked as lost though the particle never entered it. This circumstance is less probable in the detectors 20 and 21 as at least two detectors have to detect tracklets based on noise simultaneously. Normally, the efficiencies of detector 22 and 19 should be equal, but again according to the inferior acceptance of the upper cosmic trigger those events, which are created by a particle traversing the detectors 21 to 18 and by noise in detector 23, are not recorded. The escape from stack 3 in z-direction, that contributes to wrong efficiency measurements, hardly occurs in y-direction. This is due to the smaller acceptance of both cosmic triggers in this direction. Hence, in case the particle escapes from detector 18 or 23 it is likely to be rejected by either of the triggers. Taking all this into account, detectors 20 and 21 provide the most reliable results for the efficiency, largely independent of the cosmic setup.

In figure 6.4 the positions of lost tracklets of detector 18 are shown. The positions are calculated on the basis of a straight line fit through the tracklets found in the detectors 19 to 23. The line is propagated further to detector 18 and the y- and z-positions are

measured at its padplane. This gives an impression of the place where the rejected tracklets would have been calculated. In the upper left panel a distribution plot for the z-position is depicted. The red lines mark the border positions of stack 3 in global detector coordinates. It is obvious that a remarkable part of the positions is outside this stack. In contrast to this, the z-distributions of the detectors 19 to 23 are almost inside the red borders (see sections A.1 to A.3 of the appendix). This manifests the speculations about the efficiency of detector 18 as given above. As presumed, the y-distribution matches the borders quite well since particles which escaped from detector 18 in y-direction are not captured by the trigger anyway. The bottom panel visualizes lost tracklets of detector 18 from the view point of the padplane. Apart from the pads in row 7 and column 59 as well as row 8 and column 65 the distribution looks rather uniform. Due to their increased number of entries these two pads could possibly point to MCM channels that do not work properly. Because of the small acceptance in y no columns are marked at the borders of the detector and the pads in the middle exhibit most of the entries. In z each row is filled substantially since the acceptance of the lower cosmic trigger is large. Contrary to the y-direction no gradient is present. Since the dimension of the detectors in z-direction grows with the number of layers the entries for the padrows 14 and 15 decrease in detectors 20 to 23 (see

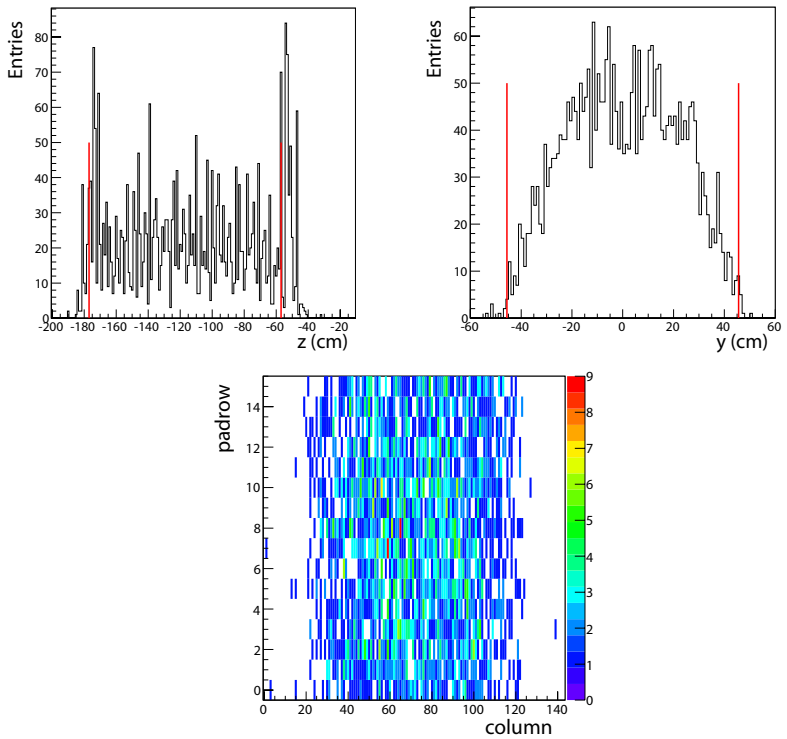

Figure 6.4: *Extrapolated positions for lost tracklets in detector 18. Upper left panel: distribution of the z-position, upper right panel: distribution of the y-position, bottom panel: padplane. Based on the trigger setup, a large part of the tracklet positions is located outside stack 3 in z-direction and as expected this behavior is not present in y-direction. The padplane shows the distribution as expected by the cosmic trigger.*

figure A.3). Probably the cosmic trigger was not placed symmetrically above stack 3, but slightly shifted in the direction of stack 2.

6.2.3 Efficiency Optimization of the Cluster Threshold

One of the most important parameters of the efficiency is the hit threshold TPHT which decides on the fact whether a hit is accepted or not. Both, too large and too small values of TPHT, would deteriorate the efficiency. In the case of large thresholds insufficient amounts of tracklets would be found, whereas at small numbers noisy pads would be marked as a hit. The purpose of this section is to find an optimized value for TPHT that considers both facts.

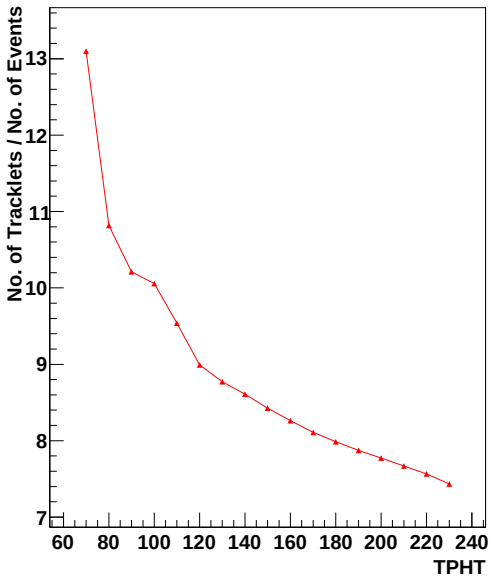

Figure 6.5: *Total number of tracklets normalized to the number of events.*

Figure 6.5 shows the total number of tracklets (normalized to the number of events) which were found during a run of $2{\cdot}10^4$ events as a function of TPHT. This number corresponds to the entirety of tracklets that are detected by the MCM without the application of any cuts. As expected it grows for decreasing hit threshold. With the kink at TPHT $\approx$ 120 the number of tracklets grows faster since at this point the pedestal value is undershot. A division by four is necessary to obtain the 'real' pedestal because of the different calculation procedure in the four CPUs. This results in a value of 30 which has to be distributed among the channels $i-1$, i, and $i+1$. Hence the value TPHT = 10 = FPNP is obtained. In case, under these circumstances, a padrow fires during an event and even if this signal produced by noise is only 1 ADC value above pedestal the hit will be detected since both criteria, the local maximum and the threshold TPHT, are complied.

Figure 6.6 summarizes the efficiency measurements of different layers as a function of TPHT. In the upper left part the tracklet loss is shown. As can be seen from this plot the loss is reduced by decreasing the value of TPHT so that for TPHT $\approx$ 200 it falls below the value of 10 % for the inner layers. This leads to the conclusion that the threshold for the default value of TPHT = 240 is too large since many tracklets which obviously belong to a particle track were rejected. As expected the efficiency simultaneously rises and reaches best values for TPHT = 190 (upper right panel). In contrast to even lower values of TPHT, the value at 190 ensures that the tracklet splitting does not increase (lower left panel). Therefore, TPHT = 190 seems to be a reasonable choice at this point of the analysis. The values for TPHT = 160 also provide good efficiencies, however the tracklet splitting slightly increases. This is the case for all lower values of TPHT, the efficiency decreases and the splitting grows so that the sum of these values would contribute to rather high efficiencies (lower right panel).

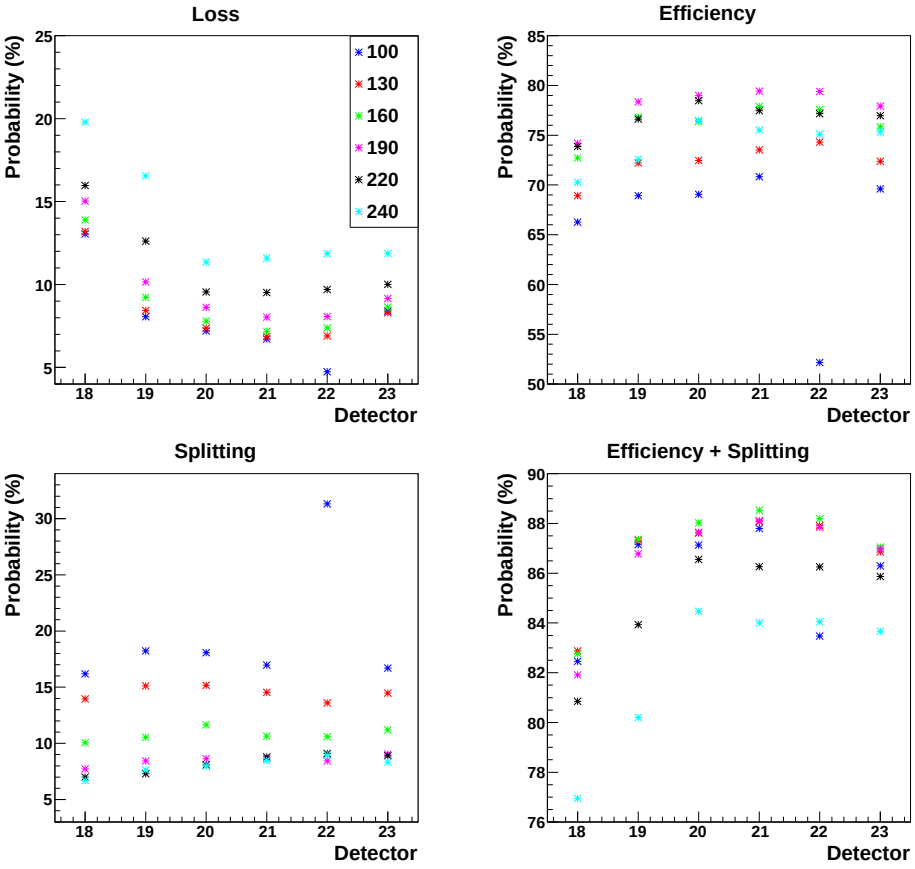

Figure 6.6: *Results for the loss, the efficiency and the splitting as a function of TPHT.*

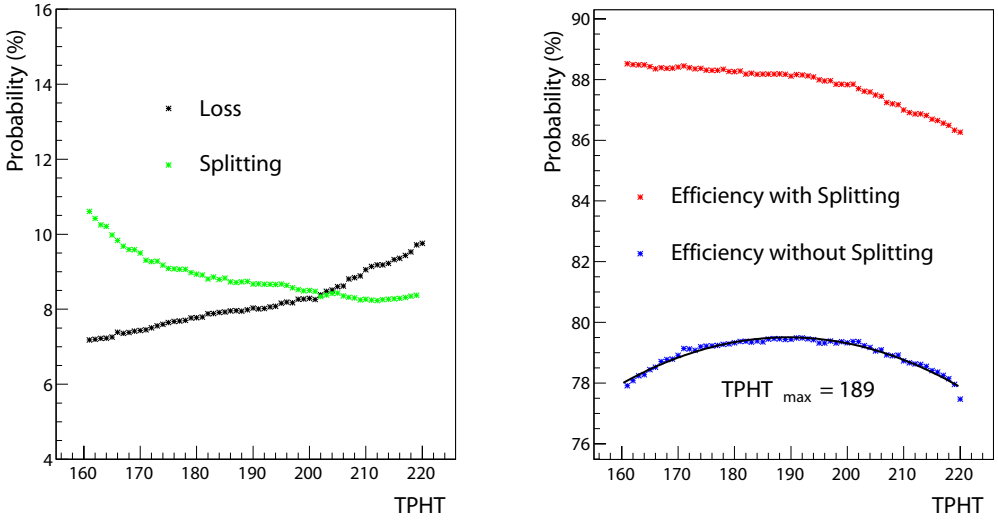

Figure 6.7: *Precise measurement of the loss, the efficiency and the splitting. At TPHT = 189 the efficiency fit reaches best values. The data is based on average values obtained from the detectors 20, 21 and 22.*

In the following efficiencies around TPHT = 190 are studied in detail. For this purpose the inner layers are used since these detectors provide results that are independent of the cosmic setup (see section 6.2.2). In the left panel of figure 6.7 the average values for loss and splitting as a function of TPHT are depicted. As expected with decreasing TPHT the number of lost tracklets is reduced, whereas the splitting strongly grows for values below TPHT = 170. In the left panel the efficiency as well as the sum of efficiency and splitting are plotted. Fitting the blue stars with a polynomial of 2^{nd} order the maximum value is reached at TPHT = 189. Since this value is still in the constant region of the splitting it seems to be a reasonable value to set from now onwards. The loss in this context corresponds to about 8 % which is distinctly smaller than for the default setting of TPHT. Indeed, for values of TPHT smaller than 189 the loss steadily reduces, but the events are more and more contaminated by noise and tracklet splitting.

6.2.4 Tracklet Splitting

One of the most important topics to discuss is the splitting of tracklets. The splitting occurs because sometimes the TPP interprets found hits wrongly. In the course of these matters it is possible that two tracklets that belong to the same particle are calculated.

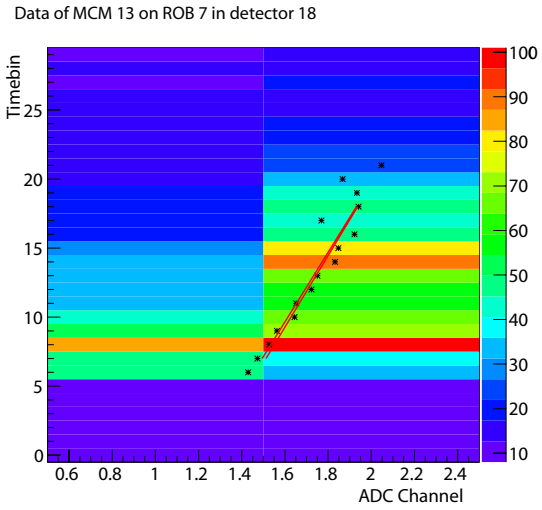

Figure 6.8: *Tracklet calculation with default values for TPCL and TPCT.*

The question that arises now is in what way the splitting deteriorates the trigger performance. Regarding measurements of the position resolution, different tracklet positions which belong to the same hit are undesired, whereas for the GTU the splitting has no dramatic impact as one of the tracklets is sorted out anyway. Since in the further chapters emphasis is put on the resolution of the tracking procedure in this section it is intended to find a configuration for TPCL and TPCT to minimize tracklet splitting for an optimized efficiency. To illustrate the tracklet splitting figure 6.8 shows a close-up of the same signal as depicted in figure 6.2 with the difference that the cluster thresholds were changed to the default MCM values. As both cluster thresholds are rather small two tracklets were calculated in this case. For a better understanding of this behavior in the following different possibilities for the tracklet calculation based on this plot are discussed in detail. To start with, the clusters (stars) of the channels 1 and 2 have to be counted in the area of the fit range. In this region channel 1 has 1 cluster and channel 2 has 10. Mainly 3 different scenarios are possible: tracklet splitting, 1 tracklet is found, and no tracklet is found. As introduced in section 5.2.5 the standard values for TPCT and TPCL are 8 and 1, respectively. This setting would contribute to the splitting of tracklets as shown in figure 6.8. Since TPCL = 1 $\leq$ 1 and TPCT = 8 $\leq$ 11 a tracklet fit is performed including the clusters of channel 1 and 2. Moreover, channel 2 exceeds the

thresholds for its own as in this case TPCL = 1 $\leq$ 10 and TPCT = 8 $\leq$ 10 delivers a true statement again[4]. Therefore, another tracklet is calculated via a fit through the clusters of channel 2 only. The two tracklets of figure 6.8 show small deviations from each other (about 160 μm), but in the case of resolution studies a difference like this has a substantial impact. With the cluster thresholds set in section 6.2.1 (TPCL = 4, TPCT = 10) only one tracklet is calculated. Regarding channel 1 as the left channel, the threshold TPCL = 4 $\not\leq$ 1 does not fulfill the condition to calculate the tracklet, whereas channel 2 with TPCL = 4 $\leq$ 10 and TPCT =10 $\leq$ 10 exceeds the thresholds for its own so that the tracklet is calculated. No tracklet is certainly found if the clusters of channel 1 fall below the threshold TPCL plus the sum of the clusters of channel 1 and 2 does not reach the threshold TPCT. Another possibility for this scenario would be that the clusters of channel 1 do not reach TPCL and channel 2 is below TPCT for its own.

In section 6.2.2 the occurrence of two tracklets was naively called splitting. In figure 6.9 this issue is specified to get an impression about the relationship of split tracklets and

[4]In this case channel 2 is the left neighbor channel as introduced in section 5.2.5. Indeed, the channel to the right does not carry any hit, but this is not obligatory since channel 2 fulfills the requirement alone.

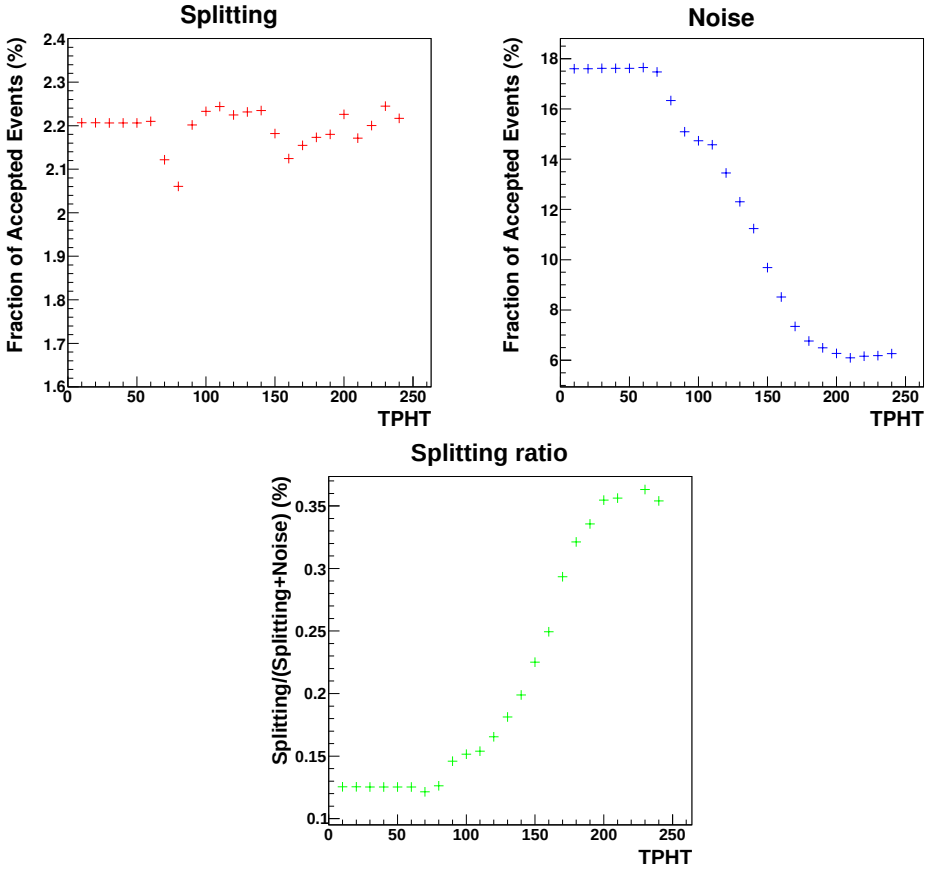

Figure 6.9: *Relation between splitting and noise ($2 \cdot 10^4$ events used). Upper panels: Number of tracklets (normalized to the number of accepted two-tracklet-events) that either correspond to noise or tracklet splitting based on different intervals of the plotted residuals. Bottom panel: the ratio of tracklet splitting in relation to the number of two-tracklet-events.*

noise. In order to distinguish between noise and splitting it is triggered on events with 2 tracklets found in detector 21 by the method explained in section 6.2.2. The residuals of the two y-positions found in this detector are calculated and inserted in a distribution plot. Assuming an error of at most one pad for the deviation of split tracklets, residuals found in the interval -7 mm $\leq \Delta y \leq$ 7 mm can be attributed to tracklet splitting. To avoid further correlations, an additional claim for splitting is that the two tracklets have to be found in the same pad row. Events with $|\Delta y| > 7$ mm are then attributed to noise. The upper panels of figure 6.9 show the entries of splitting and noise normalized to the number of accepted two-tracklet-events. The fraction of splitting fluctuates slightly but stays more or less constant. Naturally, the total number of split tracklets increases by lowering TPHT as the number of accepted events grows simultaneously. Noise strongly increases below values of TPHT $\approx$ 170. A cut on this value seems to be reasonable to avoid too much noise contamination. The current value of TPHT = 189 still seems a good choice as it exceeds the noise threshold. The kink at TPHT $\approx$ 120 as already observed in figure 6.5 means that the pedestal value is undershot. In the bottom panel the ratio of splitting to the total number of two-tracklet-events is shown. In the current region of interest (170 $\lesssim$ TPHT $\lesssim$ 240) the part of splitting is slightly above 35 %. Therefore, its influence is not negligible. After falling below the noise threshold the part of splitting decreases so that at low values of TPHT it has only a fraction of 6 %. Since the part of noise is much larger for each value of TPHT the term noise instead of splitting would be more intuitive in this case. Noting that the noise plot of figure 6.9 is based on constant values TPCL and TPCT the ratios may change by adjustment of these parameters.

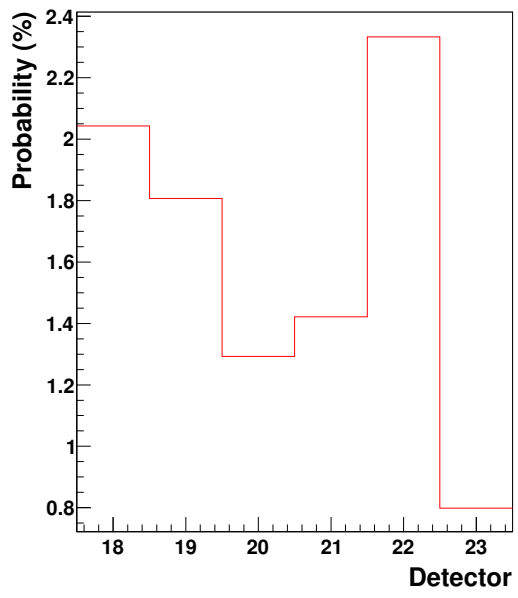

Figure 6.10: *Noise in one-tracklet-events.*

In terms of the final GTU tracking, for the 'real' efficiency the part of splitting has to be added to the efficiency as introduced in section 6.2.2 since at least one of the two tracklets corresponds to the one which was searched for. The other tracklet based on noise or splitting is rejected by the GTU anyway. In terms of resolution measurements this part must not be added as the event selector outlined in section 7.1.1 does not trigger on two tracklets found in one chamber. The other way around the noise of one tracklet events have to be subtracted from the efficiency. To determine the ratio of noise in those events a straight line fit through five detectors was performed. The line is propagated further to the detector which is currently under investigation[5]. Afterwards the position of the line and the single tracklet in this detector can be compared. In case the y-position is found in the interval $|\Delta y| > 7$ mm and the z-positions neither belong to the same padrow nor to one of the neighbor padrows the event is at-

[5]This detector is certainly left out while fitting.

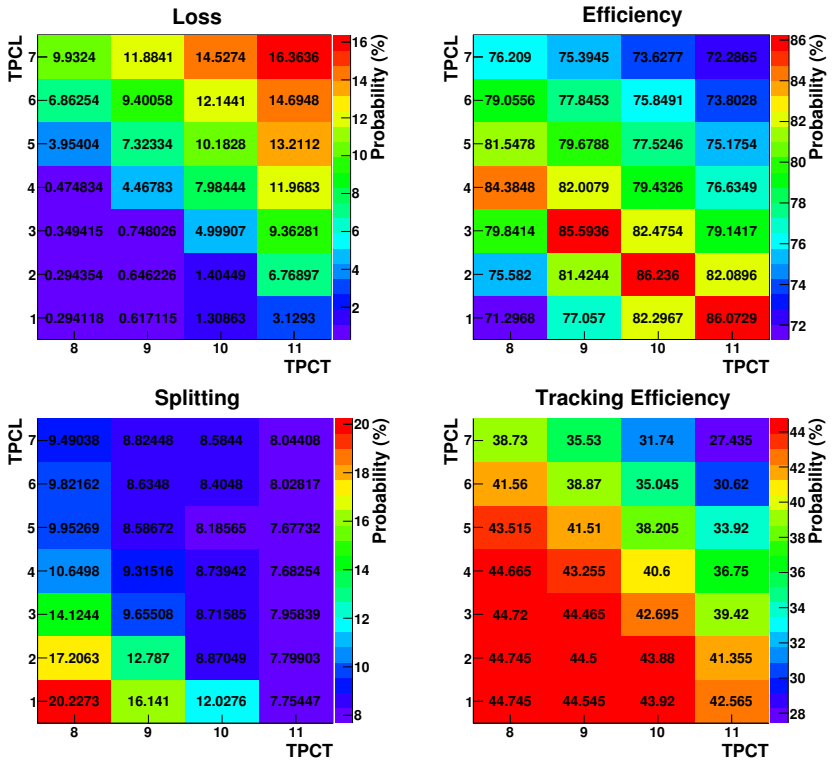

Figure 6.11: *Loss (upper left panel), efficiency (upper right panel), splitting (left bottom panel), and tracking acceptance (right bottom panel) as a function of the cluster thresholds. According to these plots the values TPCL = 2 and TPCT = 10 are chosen as optimized parameters.*

tributed to noise. Figure 6.10 shows the fraction of noise in one-tracklet-events. It only takes a small part between 0.8 and 2.3 %.

In the following the efficiency is explored as a function of TPCL and TPCT (see figure 6.11). In the upper left panel the loss is shown. Obviously, at large values of both TPCL and TPCT most of the tracklets are rejected. By decreasing either of them or both at the same time less tracklets are rejected. With a look at the efficiency plot in the right panel a diagonal from TPCL = 4 and TPCT = 8 to TPCL = 1 and TPCT = 11 promises best efficiencies. The default MCM values TPCT = 8 and TPCL = 1 as introduced in table 5.3 are useless as almost no tracklets are rejected, the efficiency is only 71.3 %, and splitting (left bottom panel) occurs numerously. With 86.2 % the value at TPCL = 2 and TPCT = 10 has the best efficiency value. With only 1.4 % the loss is reasonably small. Also the splitting or better to say the impact of noise with a value of 8.9 % is not too strong. Therefore, the value of TPCT is kept and TPCL is changed to 2 for the optimized settings. As the optimization method for the cluster thresholds is strongly dependent on these parameters itself, in the right bottom panel the tracking efficiency combined with the trigger acceptance is shown to get an impression of the total number of accepted tracklets. This quantity is simply called tracking efficiency from now on. To obtain this efficiency it is triggered on events with at least four tracklets in different detectors to ensure that

a particle track has traversed the stack. The resulting number is normalized to the total number of events. The values for the diagonal mentioned above are around 42 % to 44 %. This rather small number is due to the low acceptance of the cosmic trigger in the coincidence mode. Therefore, it does not represent the 'real' tracking efficiency which would be much better in the case of a more sufficient trigger acceptance. Nevertheless, this number is an indicator for the efficiency of tracking with the particular settings of the MCM. The efficiency at TPCL = 3 and TPCT = 9 is indeed smaller than the value at TPCL = 2 and TPCT = 10, but the tracking efficiency is slightly better. Therefore, TPCL = 3 and TPCT = 9 would be another appropriate choice for the current value of TPHT as the two effects balance each other.

The optimization so far concentrated on TPCL and TPCT while TPHT was held constant. Figure 6.12 shows efficiency plots for different values of TPHT while changing the cluster thresholds. Best efficiencies are again around 85 %, but now reached by other choices of TPCL and TPCT. For TPHT = 240 such a value is e.g obtained by TPCL = 5 and TPCT = 7. This setting maybe appropriate for GTU tracking but not for resolution measurements since splitting grows due to the rather small cluster thresholds. The final choice of the thresholds depends on the purpose of tracking. To find the parameters the plots for loss, efficiency, splitting and tracking efficiency have to be studied in detail. For this purpose, sections A.4 to A.6 of the appendix give an overview of loss, splitting and tracking efficiency as a function of TPCL and TPCT as well as for different values of TPHT.

6.2.5 Summary of Efficiency Measurements

In the previous sections a method was developed to determine the efficiency of online tracklets by using cosmic rays. In doing so, the setup of the cosmic trigger in the coincidence mode had to be considered to explain the efficiencies of single detectors in stack 3. The parameters fit range, hit threshold and the cluster thresholds were explored to optimize the efficiency. The process of optimization concerning these 3 phases is illustrated in figure 6.13. It shows the probability of the three observables loss, efficiency and splitting for different detectors in stack 3. For the first time an error estimation of the efficiency is performed in these plots. The values for loss, efficiency and splitting are mean values which originate from 7 independent measurements including $2 \cdot 10^4$ events each. The uncertainty of the mean is then estimated by:

$$\Delta v = \sqrt{\frac{1}{n(n-1)} \sum_{j=1}^{7} (v_j - \overline{v})} \tag{6.1}$$

In this formula v_j stands for the loss, efficiency or splitting from a single measurement, $\overline{v}$ is the related mean value, Δv represents the error inserted in figure 6.13, and n stands for the number of measurements.

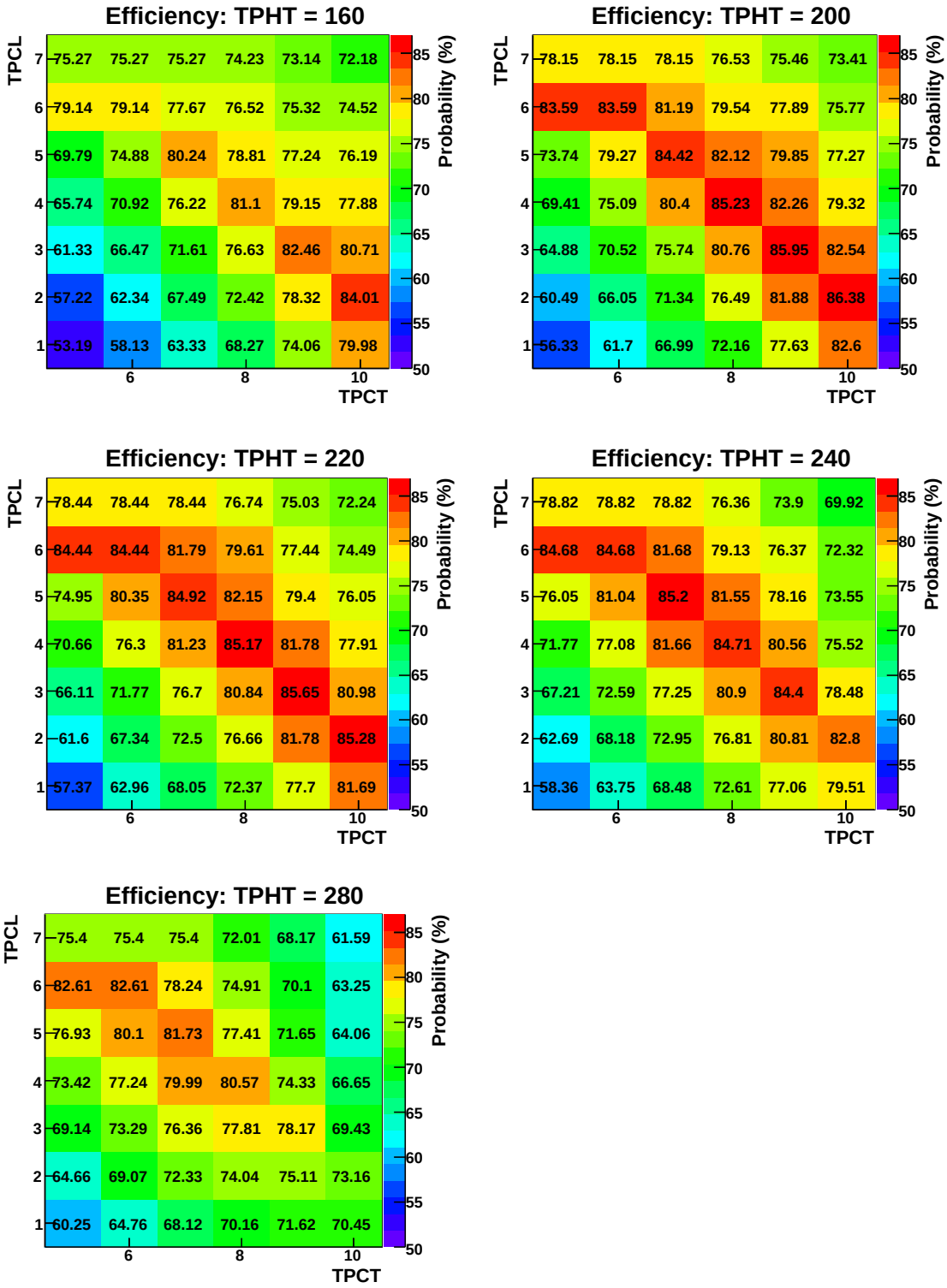

Figure 6.12: *Overview of the efficiency for different thresholds of TPHT.*

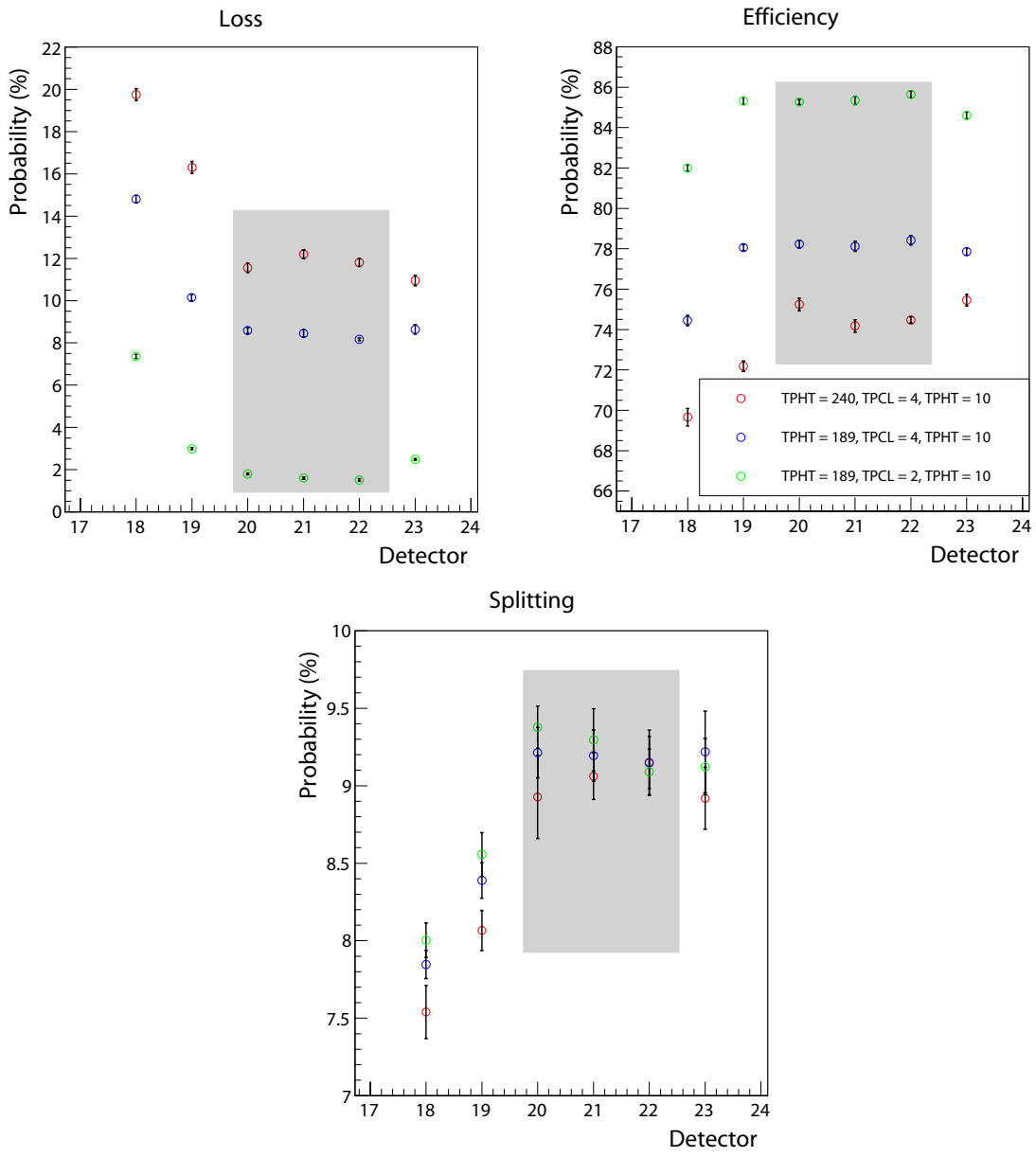

Figure 6.13: *Optimization for loss, efficiency and splitting using different parameters. The error is obtained by calculating the uncertainties of the mean values of 7 uncorrelated measurements including $2{\cdot}10^4$ events each. The gray box involves the inner layers which are independent of the cosmic setup.*

7. Position Resolution of Online Tracklets

In the following different methods to obtain the resolution of the y-position calculated by the MCMs in the online tracking procedure are described. The most serious problem that occurs is the influence of the tilted pads. Actually, the pad tilting should improve the resolution of the z-coordinate as outlined in section 4.5.4, but in the case of online tracking in the TRD test-setup this correction leads to problems concerning correct resolution measurements. In the Offline-Framework the tilted pad correction is realized by using an elaborate algorithm. This algorithm claims both, an enormous expenditure of time[1] and an adequate CPU performance. Therefore, no tilted pad correction is realized on MCM level. Besides, the exact offline algorithm cannot be applied for online tracklet reconstruction as neither the necessary cluster information nor a precise z-position is included in the tracklet word.

Another challenge in this thesis was to find an appropriate mechanism to determine a convincing resolution since there are no standard algorithms or default macros available in Aliroot that allow a rapid study. In the following chapter different methods are discussed to obtain information about the online tracking performance. To begin with, a quality measure of tracklet positions is given in section 7.1 using a simple straight line fit. One promising tool for the tilted pad correction in this case is the GTU fit which is based on a straight line using a vertex constraint. This algorithm is depicted in section 7.1.3. One possible approach to compare the y-positions with those computed during offline reconstruction is described in section 7.2. The most reasonable method to get reliable results is to compare online tracklets with simulated Monte Carlo tracks. This is done in section 7.3.

In sections 7.1 and 7.2 the determination of the position resolution is based on cosmic data. In this case the settings for the data taking as introduced in section 6 were applied. In section 7.3 Monte Carlo simulations are used for resolution measurements. The simulations are performed with Aliroot version `v4-17-Rev-12`. In sections 7.1 and 7.2 the MCM simulator is used to calculate the online tracklets based on raw data. The default MCM parameters are adjusted to the optimized values found in chapter 6. In section 7.3 the MCM simulator is applied to simulated Monte Carlo data.

7.1 Tracklet Quality Fit

7.1.1 Event Selection in Aliroot

The Aliroot programs which are used for the resolution measurements in this chapter include a simple but effective tracklet event selection. An event is accepted if 6 tracklets are found in stack 3, where each of the tracklet has to be located in a different detector in order to proceed with further calculations. This practice contributes to an easier handling

[1] Compared with the timeframe the MCM is forced to finish calculations (6.5 μs).

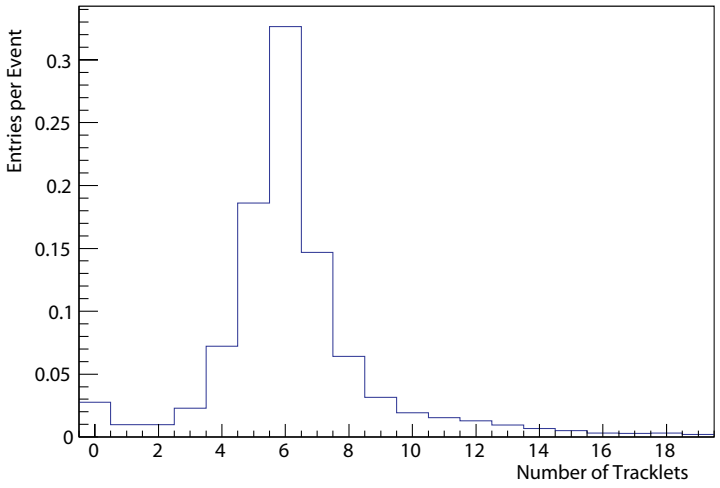

Figure 7.1: *Number of tracklets normalized to the number of events.*

of data and it ensures with high probability that the found tracklets originate from one particle track.

Figure 7.1 shows the distribution of the number of tracklets that have been found per event. The occurrence of 5, 6, or 7 tracklets is most probable with a fraction of 67 %, where 6 tracklets represent the largest fraction (33 %). Due to particle showers, incorrect settings in the TPP, random coincidences, or noisy pads it is possible that more than one tracklet is found in a chamber which does not belong to the particular particle track. The additional requirement that each of the 6 tracklets is related to a different detector leads to a final data efficiency of about 25 %. This rather small number is because of the lower acceptance of the coincidence trigger when using only stack 3 compared to the entire acceptance of the lower cosmic trigger.

7.1.2 Simple Straight Line Fit

A first quality check for the position resolution can be accomplished using a simple straight line fit. Therefore, events selected in section 7.1.1 are studied. A straight line fit through the six tracklets found was performed and is sketched in figure 7.2 (left panel). Built upon this plot, the resolution is obtained by calculating the residuals between the y-positions of the tracklets and those of the straight line fit at the respective x-reference position. As the event selection always includes six chambers of one stack the residuals of six different layers are available. Figure 7.2 (right panel) shows the distribution of these deviations as a superposition of all layers.

The distribution of the residuals is fitted with a Gaussian. The variable μ stands for the mean of the distribution. The quantity σ is the standard deviation and has a value of 1.2 mm. It is a measure for the resolution.

In comparison with the granularity of the stored y-position in the tracklet word and the results that have been found in [Wul09] using a cluster fit to determine the residuals, the

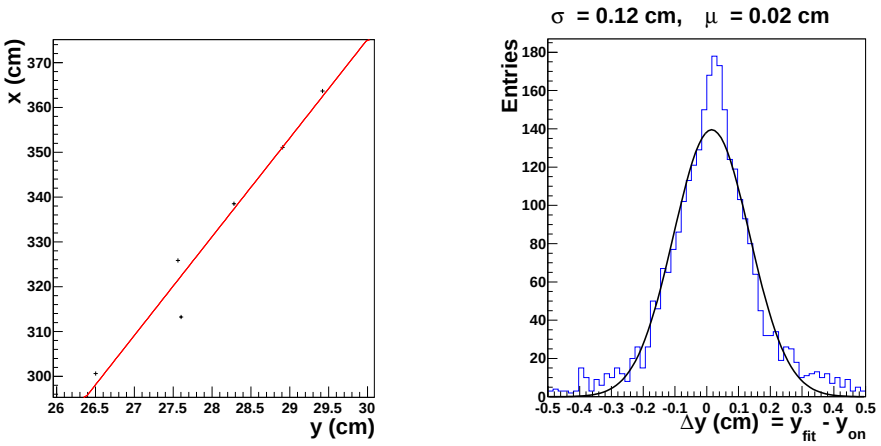

Figure 7.2: *Left panel: quality fit through 6 tracklets, right panel: distribution of the residuals calculated by the fit. The quantity σ depicts the resolution and has a value of about 1.2 mm.*

resolution obtained in figure 7.2 is not satisfactory. The decisive difference of the cluster fit performed in [Wul09] are the tilted pads. The cluster fit is confined to a single chamber so that the resolution can be determined independently. Contrary to this, the resolution for online tracklets using a straight line fit is based on all chambers and therefore strongly influenced by the pad tilting. The plot in the left panel of figure 7.2 indeed provides evidence that the tracklets belong to a dedicated track, but an adequate investigation of the resolution is not possible without a correction of the tilted pads. The strong influence of the tilting is once again sketched in figure 7.3, where the resolution distribution is shown for single layers. Not only the fact that these distributions are distorted and do not look like the expected Gaussian functions anymore, but also the fact that they are shifted in the opposite direction for consecutive layers points towards the tilted pads.

The low resolution can possibly be understood in figure 7.4. In the left panel the misleading signal induction is shown, which is caused by the tilted pads. At the center of the pad $z = 0$ the influence vanishes since this is the rotation point. Going to the boundaries of the pad in z-direction the impact of the tilting increases. As a consequence the red dot that indicates the position measured by the detector does not coincide with the real position illustrated by the blue dot. These errors occur in opposite directions for consecutive layers and thus deteriorate the resolution measurement. This is once more clarified in the right panel. The blue crosses depict the tracklet positions in different layers without the influence of the tilted pads, whereas the red crosses consider its influence. It is expected that the fit remains almost the same for both cases, but the residuals differ considerably. This fit is an example based on the assumption of an incident angle θ around 90°, as only for this, the symmetric shifts of the tracklet positions occur. For smaller θ a track can cover two or three padrows while traversing the detectors. Therefore, it is not guaranteed that the tracklet is measured at the same z-position with respect to the distance to the center of the pad. As a consequence the resolution can improve locally by accident. An example for this is given in figure 7.2 (left panel) where the residuals are small for layers 3

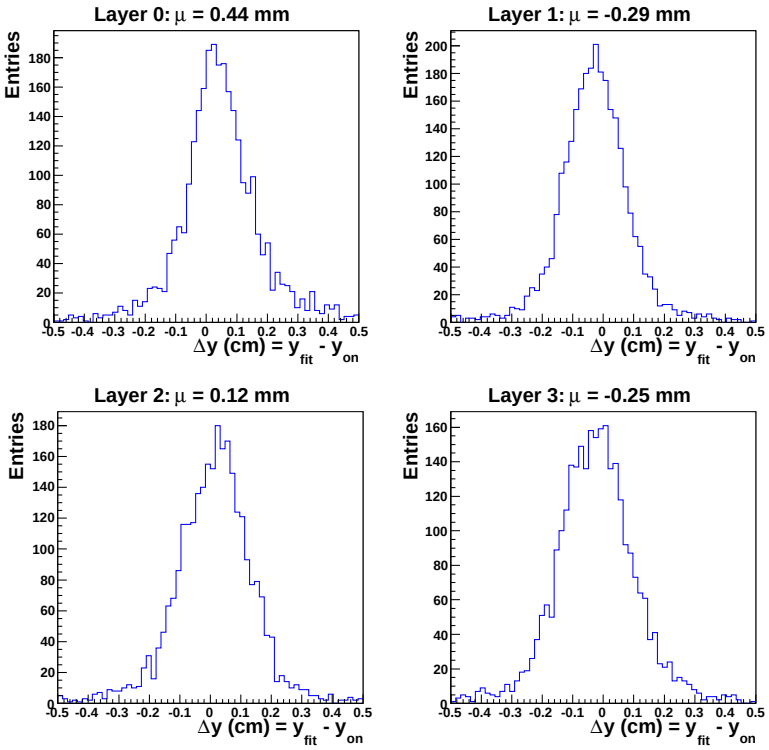

Figure 7.3: *Left panels: distribution for even layers, right panels: distribution for odd layers. The mean values of these distributions show considerable deviations from zero, although the most likely value is still near zero. This leads to asymmetric distributions that lost their original Gaussian shape. The symmetry is restored by superposing them as shown in in figure 7.2. The asymmetry arises from the influence of the tilted pads.*

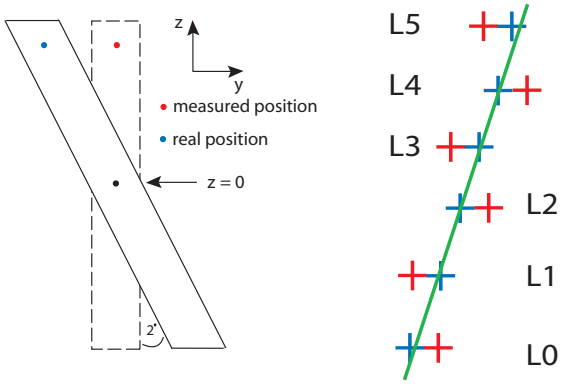

Figure 7.4: *Consequences of the pad tilting. Left panel: the dashed rectangle with the red dot shows the position that is read out by the FEE. The solid line depicts the tilted parallelogram with the position where the cosmic ray really hits the chamber. Right panel: straight line fit through corrected (blue crosses) and uncorrected (red crosses) positions. The symmetric shifts only occur for $\theta \approx 90°$.*

to 5 but become worse for the lower ones. An explanation would be that the particle hits the pad centrally in layer 5, but then heads towards the borders since θ differs from 90°. Another influence which causes the fit-quality to be unpredictable is that the padrows are not aligned to common row borders in z-direction for different layers. Even if a particle with $\theta \approx 90°$ traverses a padrow i in the upper layers, it is not guaranteed that it hits the same padrow in the lower layers. As the y-position is strongly correlated to the local z-position on a pad it is possible that more or less random-like positions are created. The residuals of these positions only provide reasonable results in case the tilting is corrected. All in all, the influence of the tilted pads as described above strongly deteriorates the y-resolution measurement.

7.1.3 Tilted Pad Correction Using the GTU Fit

One possibility to solve the problem concerning the pad tilting is to apply GTU-tracking. A consequence of this would be to rely on a vertex constraint that possibly leads to problems in the setup using cosmic rays. This is because cosmics entering the supermodule do not pass the origin of the coordinate system. This section shows whether the approach of a primary vertex assumption can be applied in the cosmic test setup.

GTU Tracking Procedure

At first, the assumption of a straight line fit is a good approximation for the selection of high p_t tracks in the online tracking procedure of the GTU. The track matching is built up on the projection of tracklets to a virtual y-z-plane[2] in the early phase after the data transmission from the MCMs. It is performed to ascribe at least four tracklets that are found in a small window in this plane to a single track. The matching in z is done using pre-defined sets of padrows that a track originating from within $|z| < 20$ cm can cross. In y-direction the projection is accomplished using the tracklet information calculated in the MCMs [Kle08]:

$$y_{\text{proj}} = y + dy \cdot \frac{(x_{\text{mid}} - x_L)}{dx_{\text{drift}}} \tag{7.1}$$

The slope $\frac{dy}{dx_{\text{drift}}}$ is used to map the tracklet on the reference plane x_{mid}. Thus, the only free parameter in this formula is the position of the layer x_L where the projection shall proceed. The value y is known from the tracklet word as well.
In z the projection is directed to the vertex [dC03]:

$$z_{\text{proj}} = z \cdot \frac{x_{\text{mid}}}{x_L} \tag{7.2}$$

As in the current test setup the GTU does not posses such capabilities (see section 5.1.3) the event selection outlined in section 7.1.1 is used. Indeed, this contributes to a lower efficiency compared to the GTU track matching, but it is sufficient for the analysis.

[2] Layer 2 is used as a reference to minimize errors of the projected positions.

Pad Correction

Just like the projection, the track calculation is based on a simple straight line fit through found tracklets because a full helix fit consumes too much time. The pad tilting can be corrected with the assumption of a primary particle. Therefore, the z-coordinate, which is necessary for the correct calculation of formula 4.6, is substituted by the quantity $z = c \cdot x$. The parameter c describes the constraint and can be descriptively regarded as the arc tangent of the angle in the x-z-plane (θ in local coordinates) pointing to the vertex. This parameter is optimized using the least squares method. The formula for the pad correction then reads [Kle08]:

$$y' = a + bx + (-1)^L \cdot \tan(\beta_{\text{tilt}}) \cdot c \cdot x = a + bx + (-1)^L \cdot c' \cdot x \tag{7.3}$$

This is simply a straight line fit with a correction of the pad tilting. The parameter b denotes the offset, a and c stand for the slope in the respective planes x-y and x-z. Since the tilting angle β_{tilt} is constant the parameter c can be written as $c' = \tan(\beta_{\text{tilt}}) \cdot c$. Using the least squares method the parameters should be optimized in a way to determine an exact z-position so that the tilting can be corrected.
For this purpose χ^2 has to be minimized:

$$\chi^2 = \sum_{L=0}^{5} \left(y_L - a - b \cdot x_L - (-1)^L \cdot c' \cdot x_L\right)^2 \tag{7.4}$$

In contrast to the general definition, χ^2 is not normalized to the errors of the variables. The sum runs over 6 layers including 3 parameters, which yields 3 degrees of freedom. y_L is the input value directly obtained from the tracklet word and measured at the x_L-reference of the particular layer L.
One possibility to solve the problem is to use the ansatz of the normal equation [Lor03]:

$$\overline{\overline{M}}^T \circ \overline{\overline{M}} \circ \vec{u} = \overline{\overline{M}}^T \circ \vec{y}_L \qquad \Leftrightarrow \qquad \vec{u} = \left(\overline{\overline{M}} \circ \overline{\overline{M}}^T\right)^{-1} \circ \overline{\overline{M}}^T \circ \vec{y}_L \tag{7.5}$$

with

$$\overline{\overline{M}} = \begin{pmatrix} 1 & x_0 & x_0 \\ 1 & x_1 & -x_1 \\ 1 & x_2 & x_2 \\ 1 & x_3 & -x_3 \\ 1 & x_4 & x_4 \\ 1 & x_5 & -x_5 \end{pmatrix} \quad , \quad \vec{y}_L = \begin{pmatrix} y_0 \\ y_1 \\ y_2 \\ y_3 \\ y_4 \\ y_5 \end{pmatrix} \quad , \quad \vec{u} = \begin{pmatrix} a \\ b \\ c' \end{pmatrix} \tag{7.6}$$

Vector $\vec{u}$ can be used to calculate the corrected value y' with the help of optimized parameters a, b, and c'.
The result of this procedure is shown in figure 7.5. In this graph the residuals of the corrected positions y' and the related straight line fit are plotted. In contrast to figure 7.3 the shifting of the Gaussian functions has weakened, but is still present. The resolution seems to have improved, but it is subject to strong fluctuations. It is very peculiar that the

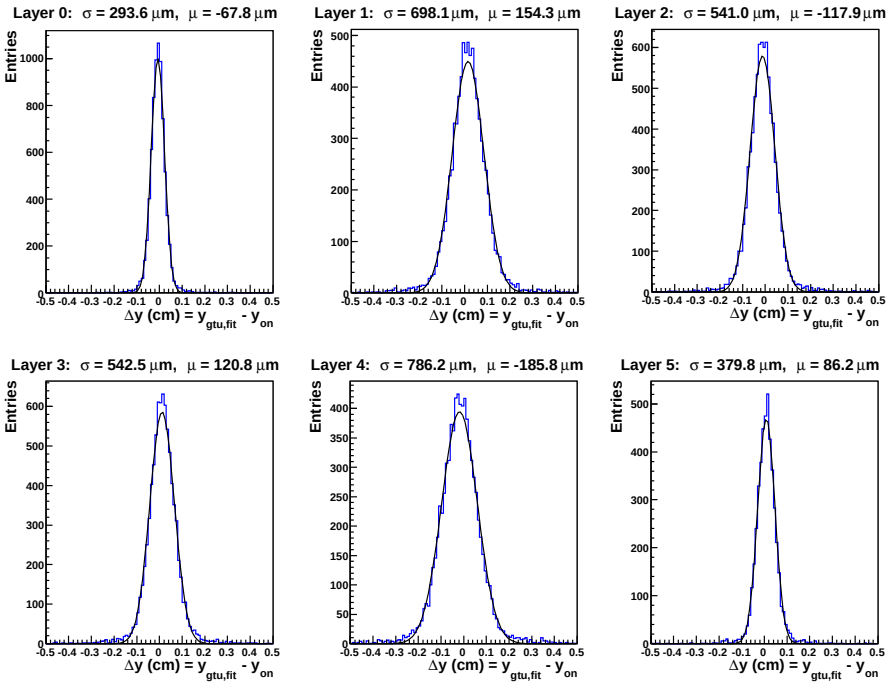

Figure 7.5: *Distribution of the residuals between y′-positions calculated with the least squares method and the linear fit through the corrected values. The shifting behavior has weakened but is still present. The resolution has improved and the Gaussian shape has been restored.*

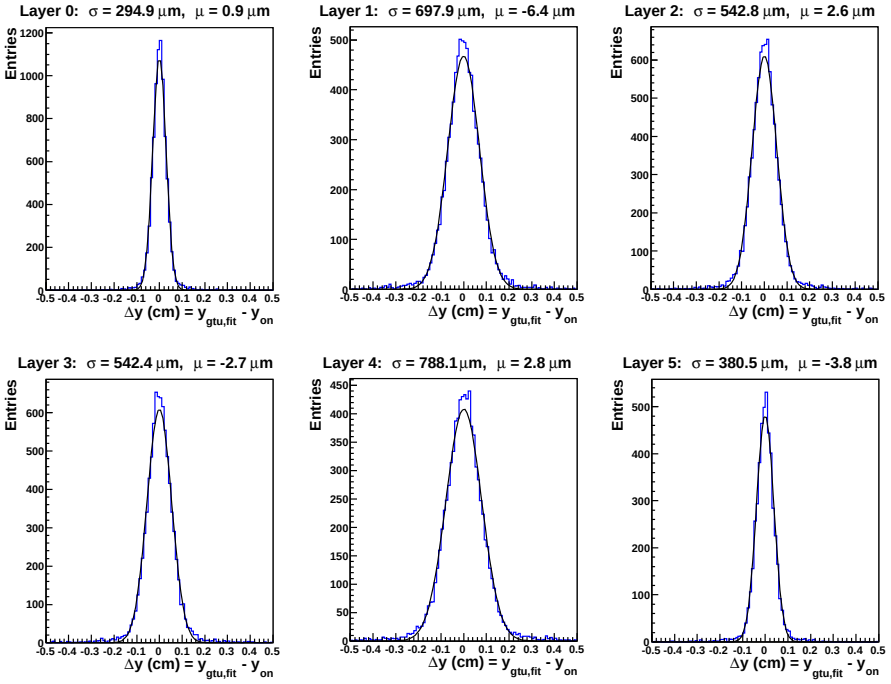

Figure 7.6: *GTU refit after correcting the y-positions with the mean values of figure 7.5. The shifting has vanished but the resolution does not improve.*

resolution in layer 5 is much better than in layer 1. Contrary to this, it is expected that the resolution decreases with growing number of layer since the granularity of the pad worsens in the upper layers. Moreover, there is a noticeable correlation between the resolution σ and the mean μ (see figure 7.5). This could possibly originate from misalignment of the TRD chambers in stack 3. Therefore, the vector y_L is corrected by shifts of the Gaussian distributions taken from figure 7.5 and the GTU fit is performed again (see figure 7.6). The shifts have weakened but the resolution does not improve. Consequently, the possible influences of alignment could not be corrected by this method and the results obtained so far lead to first doubts concerning the fitting procedure of the GTU in the cosmic test setup.

7.1.4 The Resolution as a Function of the Angle

The resolution σ calculated in the previous section is not the intrinsic one. This resolution depends on two uncertainties: σ_x originating from the charge deposition of the primary particle along the drift region in x-direction and σ_y limited by the ROC geometry. Figure 7.7 shows a particle traversing the x-y-plane in one timebin. The red dot stands for the x-position where the primary particle deposits its charge concerning the center of gravity. The blue dot describes the reconstructed position of the red dot extracted from the timebin information. The deviation of the two dots dominates the uncertainty in x-direction. Depending on the incident angle ϕ of the particle, this uncertainty directly influences the y-resolution. At an angle of $\phi = 0°$ no deterioration is expected as in this case the de-

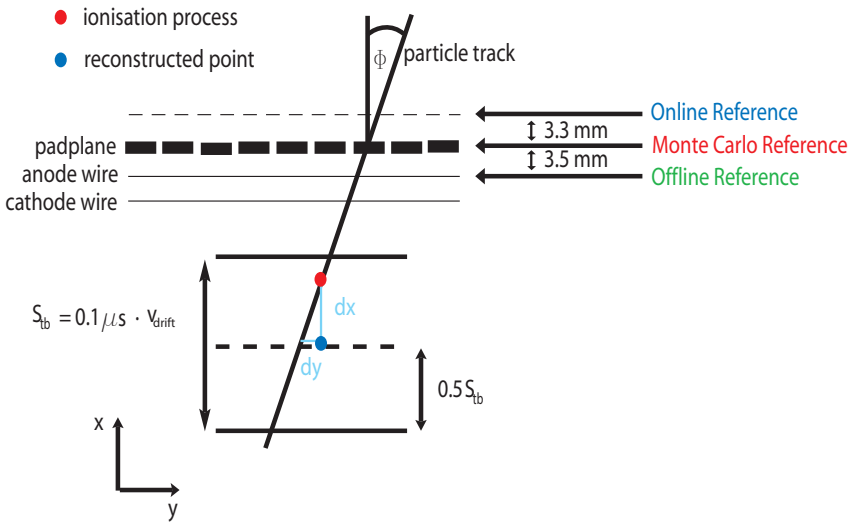

Figure 7.7: *A particle traverses the section S_{tb} which corresponds to the interval of one timebin. The x-position is determined timebin-wise with an error of σ_x. As a consequence the y-position resolution of tracklets with large ϕ is much more deteriorated than the resolution of tracklets with small ϕ. For the later discussion different reference planes where the y-position is measured are drawn. The offline tracklets are referred to the anode wires, the Monte Carlo track can be measured at the padplane, and online tracklets are determined about 3.3 mm above the padplane.*

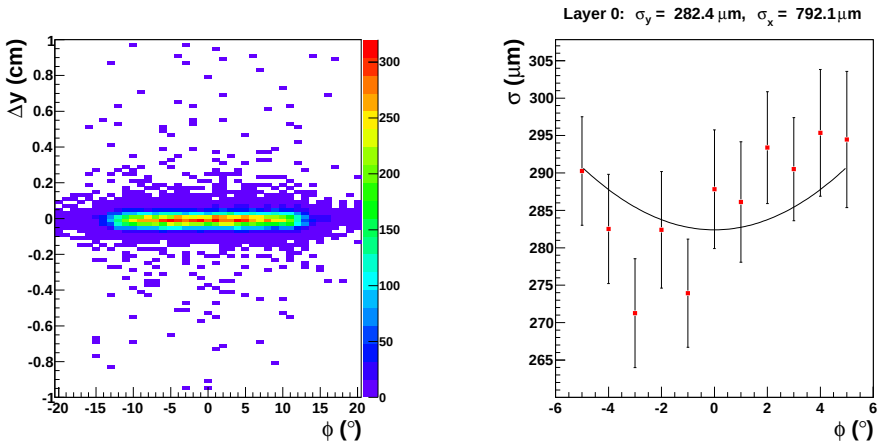

Figure 7.8: *Left panel: The residuals of figure 7.5 (layer 0) are plotted vs. the angle ϕ which is obtained from the straight line fit. Right panel: The value σ is plotted as a function of ϕ.*

termination of the y-position does not depend on the x-reference. At increasing angles ϕ the impact of the x-resolution grows. Therefore, the uncertainty of x can be expressed by $\sigma_x \cdot \tan(\phi)$ so that the overall resolution can be described using the error propagation law:

$$\sigma = \sqrt{\sigma_x^2 \cdot \tan^2(\phi) + \sigma_y^2} \tag{7.7}$$

Figure 7.8 (left panel) shows the residuals Δy for the GTU fit as a function of the angle ϕ. This angle is taken from the slope of the linear fit. To obtain the intrinsic resolution σ_y, as depicted in equation 7.7, the values for Δy around $\phi = 0$ are important. Hence, the 2-d diagram is projected to the Δy-axis for single angle intervals [-9.5°, -8.5°], [-8.5°, -7.5°], ..., [7.5°, 8.5°], [8.5°, 9.5°]. With this procedure 19 new 1-d histograms are created each displaying the position resolution inside the angle interval [i - 0.5 , i + 0.5] with $i \in$ [-9,9]. Each of these histograms is fitted with a Gaussian and the parameter σ is plotted in the graph of the right panel for the respective angle interval. The errors for the value σ are taken from the errors of the fitting procedure of the respective Gaussian functions. The distribution in the right panel of figure 7.8 can be fitted with the function of equation 7.7 using the two free parameters σ_y and σ_x. However, due to the large errors the fit is not really convincing. It seems that there is no obvious correlation between Δy and ϕ. Indeed, Δy slowly seems to grow with increasing angle $|\phi|$ but this is accompanied by considerable fluctuations. The minimum of the fit function depicts the intrinsic resolution σ_y. In this case it has a value of 282.4 μm. Actually, the minimum should be located at $\phi = 0$, but according to the fit of figure 7.8 this is not true. Resulting σ_x is about 792 μm, which is distinctly smaller than values found in [Wul09] and [Sic09]. Figure 7.9 summarizes the previously discussed plot for all layers. Intuitively, the resolution should worsen with ascending layer. According to figure 7.9 this is not the case as e.g. layer 5 has a better resolution than layer 1. These plots do not seem to reveal the real nature of online tracklets.

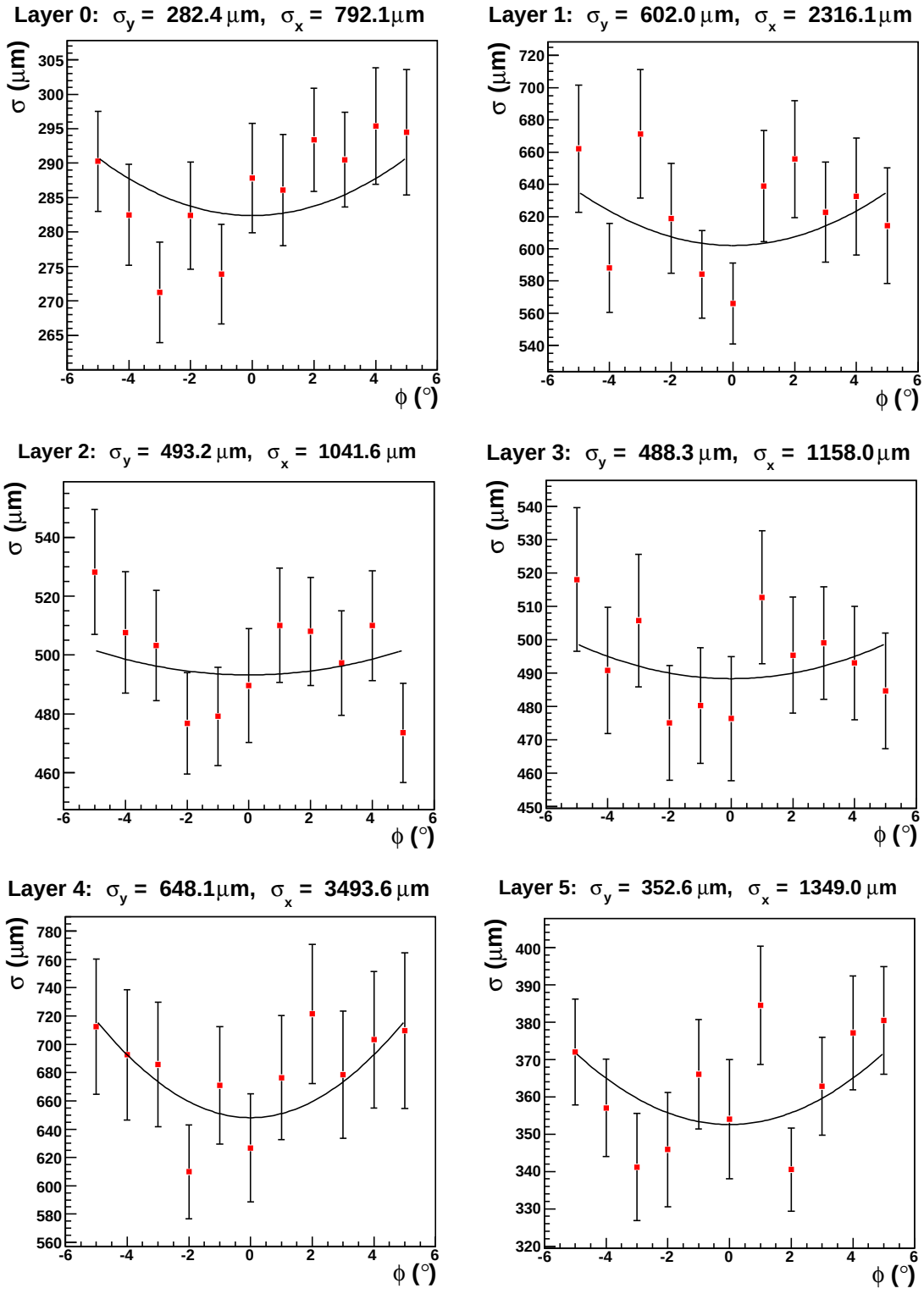

Figure 7.9: *Overview of the resolution measurement from the GTU-fit for all layers.*

All in all the topics discussed above lead to the conclusion that, as expected, the vertex constraint does not lead to reasonable results. Indeed, the resolution has been improved by application of equation 7.3, but the tracklets seem to have lost their original position properties. The main reason for the deteriorations can be ascribed to the vertex constraint which is not valid for cosmic rays. Therefore, the GTU-fit is not applicable in the cosmic test setup.

7.2 Comparison to Offline Tracklets

Offline tracklets calculated during the reconstruction offer another possibility for a comparison. As these are produced in nearly the same way as in the online procedure, namely by a cluster fit, the relation between the tracklets should give an impression of the difference between online and offline tracking. Another advantage of this comparison is that in contrast to the ESD track the offline tracklets can be accessed without tilted pad correction. Therefore, both tracklet types can be analyzed on the same level.

To obtain the difference between online and offline tracking the residuals of the y-position of online and offline tracklets were calculated. Figure 7.10 displays the distribution plots for all layers. As pad tilting does not play a role in this case the Gaussian distributions do

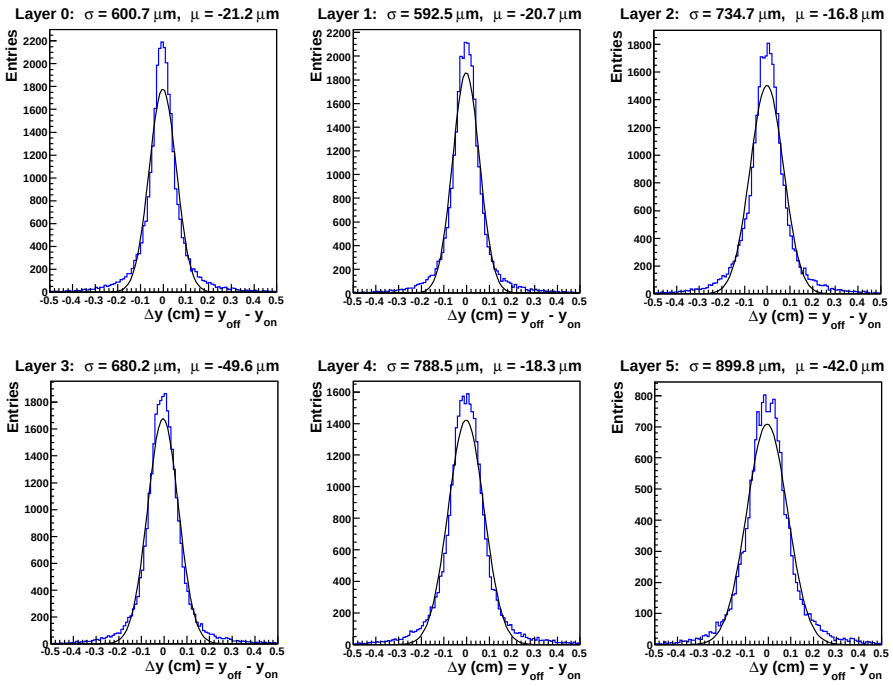

Figure 7.10: *Distribution of residuals by comparing the y-positions of online and offline tracklets. Alternating shifts per layer have disappeared since both tracklet types are not corrected for tilted pads. σ corresponds again to the standard deviation of the Gaussian fit. In this case it is not an indicator for the resolution but rather a tool to determine the differences between both tracking procedures.*

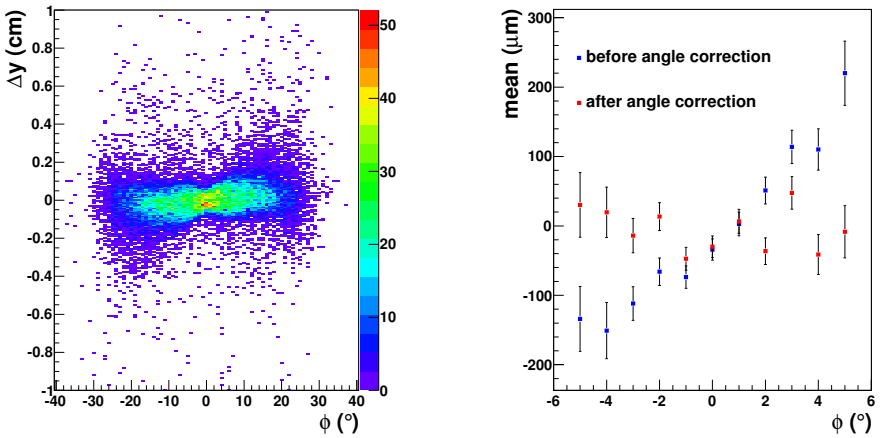

Figure 7.11: *Left panel: distribution of the offline-online residuals plotted vs. the track angle (layer 0). The slight tilting occurs because of different reference planes where the y-positions are measured. Right panel: mean values of the left distribution (again layer 0) using the reduced angle interval: -6° ≤ ϕ ≤ 6°. The slope of the blue squares emphasizes the tilting once again. The red squares are the result after the adjustment of the reference plane.*

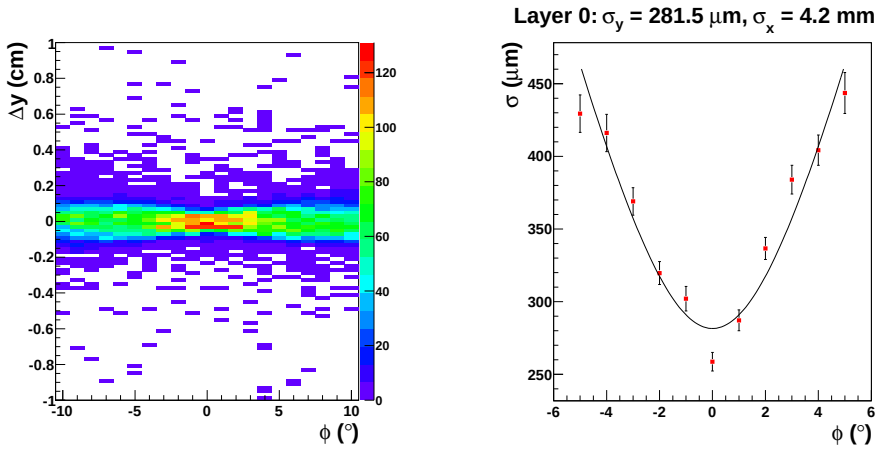

Figure 7.12: *Left panel: distribution after the correction of the reference plane (layer 0), right panel: distribution of σ as a function of ϕ to determine σ_y for the residuals of online and offline tracklets.*

not show the shifting behavior for consecutive layers as depicted in figures 7.3 and 7.5, but they rather have an offset in the same direction. This offset only amounts to very small values between -15 μm and -50 μm, which is within the region of expected uncertainties. The process to determine σ_y is visualized in figures 7.11 and 7.12. In the left panel of figure 7.11 the residuals are plotted against the reconstructed track angle ϕ to determine σ_y as outlined in the previous chapter. Since the y-position of offline tracklets is measured at the anode wires (see figure 7.7) the wrong x-reference plane deteriorates the resolution. The

consequence of a wrong reference plane is depicted in figure 7.11 (left panel) in form of the slightly tilted distribution. The explanation is similar to the discussion of the uncertainty σ_x and its impact on the y-resolution (see section 7.1.4). In terms of small incident angles ϕ, the reference plane does not play a role. At larger angles the differences of the y-positions at the respective x-references change significantly. The result is a distribution which is rotated by an angle that grows with the distance of the reference planes. For clarification of this problem, figure 7.11 (right panel) depicts the mean values computed for single angle intervals from the distribution plot as shown in the left panel. The values of the mean are calculated with the same discretization as done for the value σ in section 7.1.4. To solve the problem the offline tracklets are shifted 6.8 mm upwards (x-direction) so that they are comparable to online tracklets. The result is shown in figure 7.12 (left panel). It depicts a close-up view in ϕ of the previous distribution which has been corrected by adjustment of the reference plane. It seems to be perfectly parallel to the ϕ-axis. Based on this distribution the final resolution is plotted in the right panel. In comparison to figure 7.8 this graph is well approximated by equation 7.7. The minimum again corresponds to the resolution σ_y which has a value of 285.1 μm. The x-resolution is about 4.2 mm. An explanation for this large uncertainty is the lack of a tail cancellation filter which should improve the time resolution. With the application of this filter it is possible to determine the x-position more precisely (see section 8.2). The resolution plots for all layers are depicted in figure 7.13.

Though online and offline tracklets are based on nearly the same creation procedure, the deviations of the y-positions are larger than expected. Reasons for this could be problems in the synchronization of offline and online parameters. For instance the filter procedure is completely different for both. In order not to depend on settings applied in the reconstruction which actually are more or less a black box to compare with and since tuning of offline tracklets is not the topic of this thesis, in the next section a comparison to Monte Carlo tracks is performed.

7.3 Comparison to Monte Carlo Tracks

As the GTU fit of section 7.1.3 did not yield stable results due to the vertex constraint and the difference between online and offline tracklets of section 7.2 is rather a comparison between two tracking procedures than a real quality measurement for online tracklets, in this section Monte Carlo information is used. Due to Monte Carlo truth it is ensured to measure the 'true' positions of a particle without any unexpected and disturbing influence. Therefore, possible errors of offline reconstruction do not occur. The resolution is obtained by determination of the deviations between online tracklets and Monte Carlo tracks. Another advantage of this procedure is that Monte Carlo tracks can be programmed to originate from the primary vertex, which simplifies the pad correction enormously.

7.3.1 Settings of the Monte Carlo Simulation

The settings of the simulation are chosen to be close to the conditions of the cosmic data taking. One 4 GeV muon per event is simulated in an azimuthal range of $0° \leq \phi \leq 20°$. The pseudo-rapidity range was chosen to be $0.5 \leq \eta \leq 0.9$. These settings contribute to

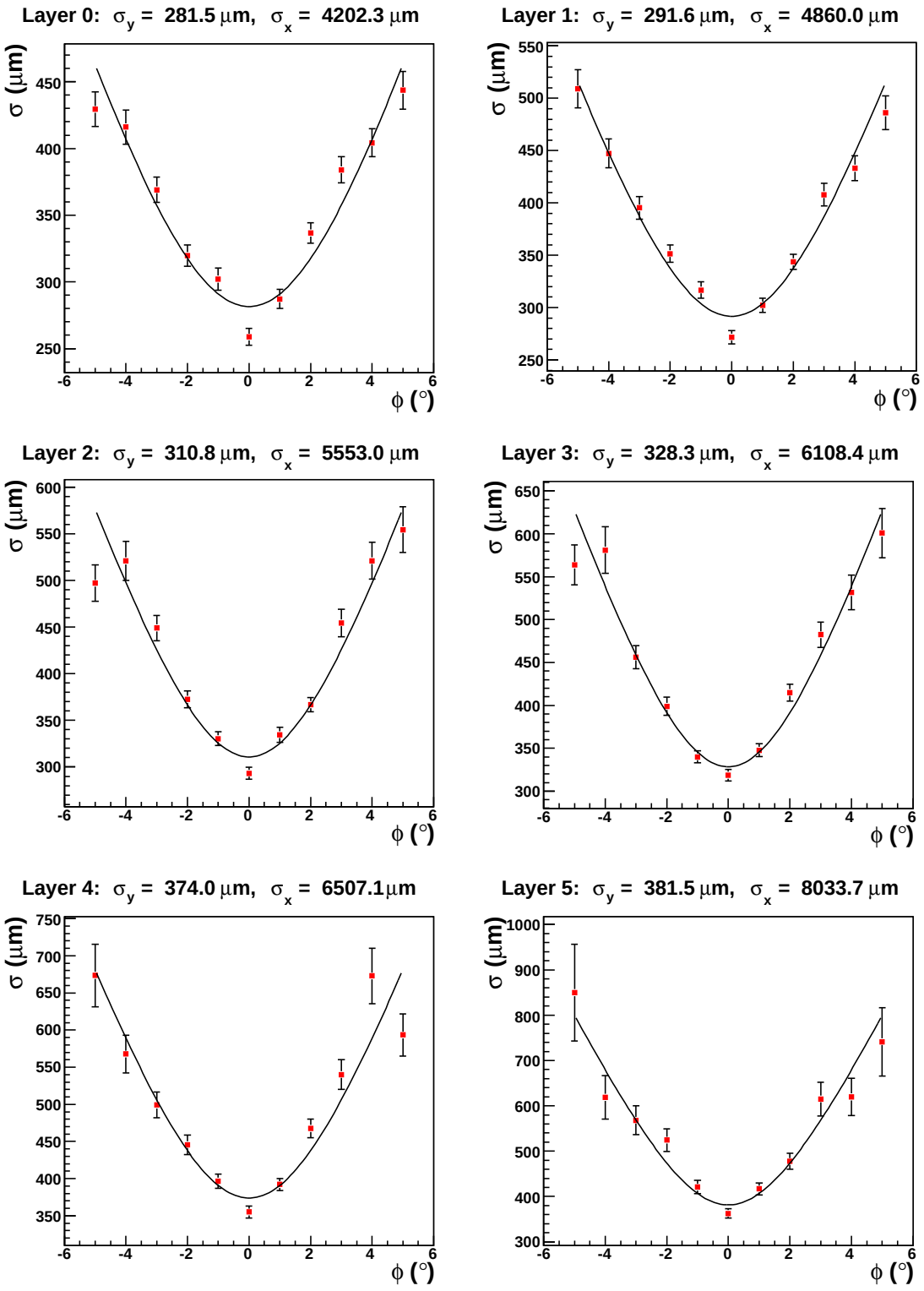

Figure 7.13: *Distribution of σ as a function of ϕ for all layers by comparing online and offline tracklets.*

particle tracks which mainly cross stack 0 of the supermodule inserted in slot 00 (global azimuthal angle $\alpha = 10°$). In addition, the magnetic field is set to zero, thus no Lorentz deflection appears just as in the cosmic test setup. The most important difference is that all particles originate from the same point. Suppressing all secondary particles the primary vertex assumption is valid. Table 7.1 summarizes the settings.

Quantity	Value
particles	1 muon per event
momentum	$p = 4$ GeV/c
pseudo-rapidity range	$0.5 \leq \eta \leq 0.9$
azimuthal range	$0° \leq \phi \leq 20°$
origin	$\vec{r} = (0, 0, 0)$
magnetic field	$B = 0$ T
detector setup	TRD only

Table 7.1: *Settings of the Monte Carlo simulation.*

For the analysis of online tracklets the MCM simulator is used once more. The MCM is simulated on the basis of the `TRDDigits.root` file produced during the Monte Carlo simulation.

7.3.2 Resolution Measurement

The resolution measurement is quite similar to section 7.2. Therefore, a correct x-reference plane has to be found first. In contrast to offline tracklets the Monte Carlo track has two references per chamber: one at the bottom of the drift volume, the second at the padplane. A straight line between these two references of the respective chamber is used to propagate the track to the reference plane of online tracklets. The residuals of the online tracklet and the line at the reference position are then a measure for the resolution.

Before calculating the residuals it is reasonable to have a look at the pulse height plot (see figure 7.14, right panel) which has been created in the same way as introduced in section 6.2.1. In the cosmic run 2249 the fit range was chosen to be TPFS = 7 and TPFE = 18 (compare to section 6.2.1). As can be seen from the pulse height plot, in Monte Carlo simulations the amplification peak already starts at timebin 1 or 2. The drift region starts around timebin 4 and its end is approximately reached at timebin 19. Thus, the MCM parameters for the fit range are chosen to be TPFS = 4 and TPFE = 19. For the calculation of the residuals the reference at the padplane is used. As visualized in figure 7.7 the x-reference plane of online tracklets is located about 3.3 mm above the padplane. Thus, the line connecting the top and bottom of the chambers is propagated to this x-position. Figure 7.15 shows the residuals plotted against the Monte Carlo track angle before and after the x-reference plane was adjusted. According to the distribution in the right panel, which is well aligned to the ϕ-axis, the current x-reference seems to be a reasonable choice. Henceforth this plane is used for the resolution measurements.

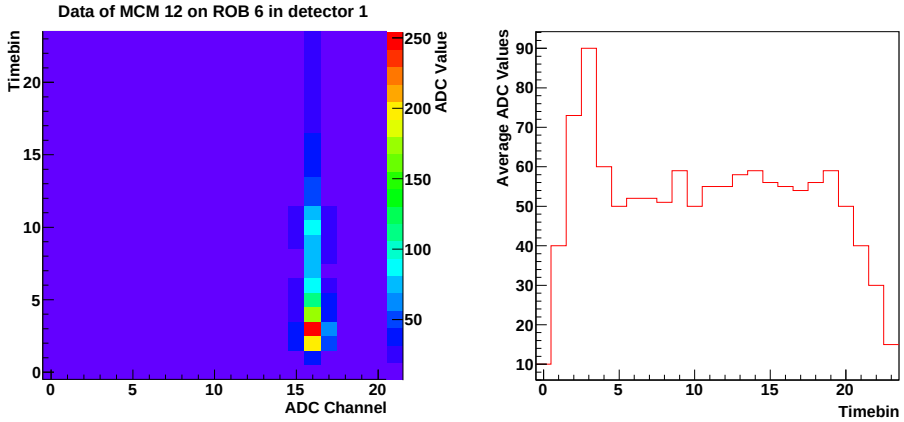

Figure 7.14: *Setting of the correct fit range. Left panel: visualization of the induced signal recorded by a single MCM over a range of 24 timebins, right panel: pulse height plot created by a projection of the ADC channels that carry the signal (averaged over $2 \cdot 10^4$ events).*

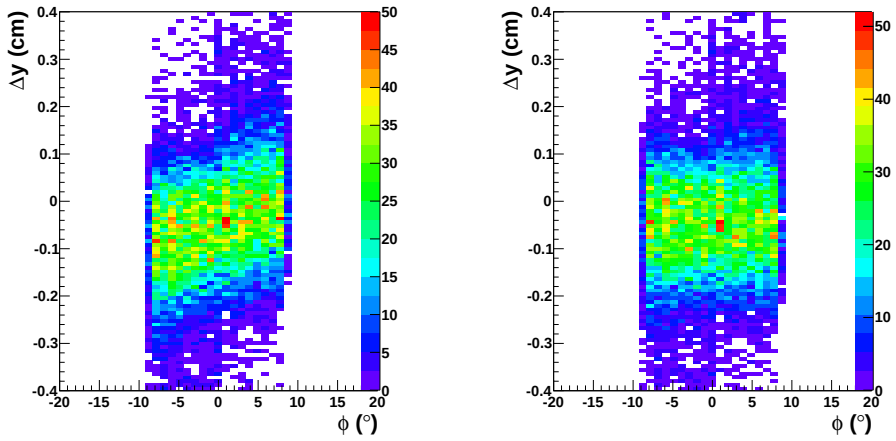

Figure 7.15: *Residuals of Monte Carlo tracks and online tracklets plotted against the Monte Carlo angle before (left) and after adjusting the correct reference plane (right). The plane set in the right panel is used for further calculations.*

7.3.3 Tilted Pad Correction

For reasonable resolution measurements the tilted pads have to be considered. One option to correct this influence is to apply equation 4.6. In local coordinates it reads:

$$y' = y + (-1)^L \cdot \tan(\beta_{\text{tilt}}) \cdot (z - z_{\text{row,middle}}) \tag{7.8}$$

In this context y' is the tilted pad aware value in local coordinates, L denotes the layer where the correction shall take place, and $z_{\text{row,middle}}$ is the center of the respective pad in global detector coordinates. Instead of tilting the online tracklets so that they match the

track, the Monte Carlo track will be tilted back in order to coincide with the uncorrected online tracklets since the z-position of the track is known precisely[3]. Thus, Monte Carlo and online tracklet information can be accessed on the same level. An important issue in this context is that also the z-position has to be measured at the x-reference plane of online tracklets. In this case the wrong reference plane would contribute to negative consequences for the correction of the tilted pads as the track to be tilted back has propagated further and possibly hits another padrow.

For the correction, the value $z_{\text{row,middle}}$ can be calculated based on the information of the padrow that is stored in the data word. The padrow has to be transformed into a global position in units of cm. This transformation can be done by using the Aliroot standard classes `AliTRDgeometry` and `AliTRDpadPlane` which include functions concerning geometrical aspects of the TRD. The conversion can be written as:

$$z_{\text{row,middle}} = \text{plane} \rightarrow \text{GetRowPos(padrow)} - \frac{\text{plane} \rightarrow \text{GetLengthIPad()}}{2} \tag{7.9}$$

The value `plane` is an instance of the class `AliTRDpadPlane` and obtained with the knowledge of the particular detector by `AliTRDpadPlane::GetPadPlane(detector)`. The function `GetRowPos(padrow)` delivers the global z-position at the beginning of the padrow. To receive the center position, half of the pad length has to be subtracted using the function `GetLengthIPad()`[4]. An illustration of these coordinates is given in figure 7.16.

Figure 7.17 shows the situation before the correction. The residuals of online tracklets and Monte Carlo tracks Δy are plotted against Δz which denotes the distance between the z-position of the Monte Carlo track and the middle of the respective padrow $z_{\text{row,middle}}$. The plots for consecutive layers display the orientation of pad tilting. At $\Delta z = 0$ the residuals are not influenced by the tilting, but going to higher values of $|\Delta z|$ the positions of the online tracklets and the Monte Carlo track are clearly distinct. As a consequence a distribution is created which mirrors the geometrical dimensions of the read out pads

[3]The z-position stored in the tracklet word with the granularity of one padrow is too imprecise for the tilted pad correction. The z-position must be very precise for an adequate performance of the correction since small disturbances will deteriorate this mechanism.

[4]This function is used for the inner pads. As the outer pads can differ in length from the inner pads the function GetLengthOPad() is used.

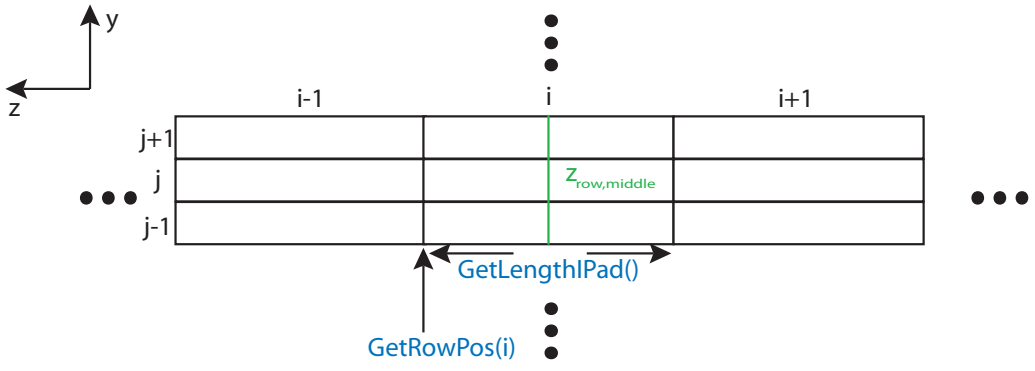

Figure 7.16: *Access of $z_{row,middle}$ with the geometry class of Aliroot.*

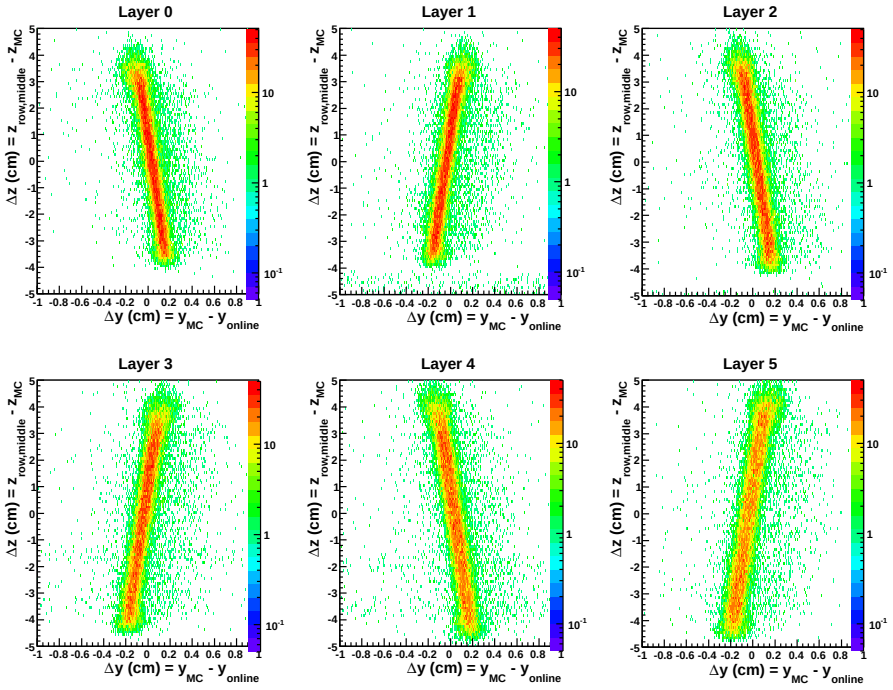

Figure 7.17: *Situation before correction of the tilting.* $\Delta y = y_{MC} - y_{online}$ *is plotted vs.* $\Delta z = z_{row,middle} - z_{MC}$*. Due to the deviations between Monte Carlo tracks and online tracklets at* $|\Delta z| > 0$ *the pad tilting can be recognized.*

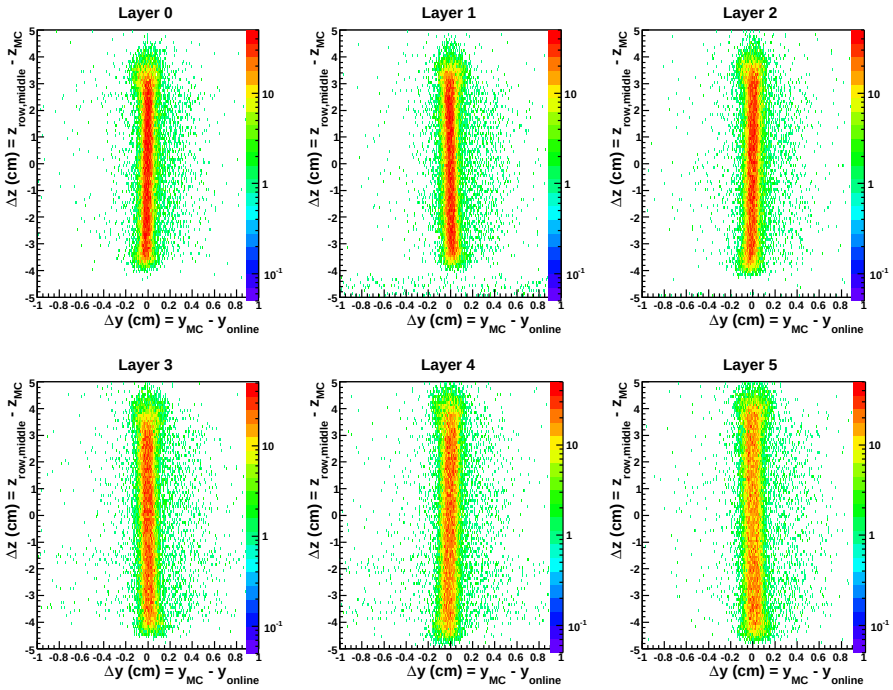

Figure 7.18: *Situation after correction of the tilting by equation 7.8. Plotting* Δy *vs.* Δz*, distributions are created which are well aligned along the vertical axis.*

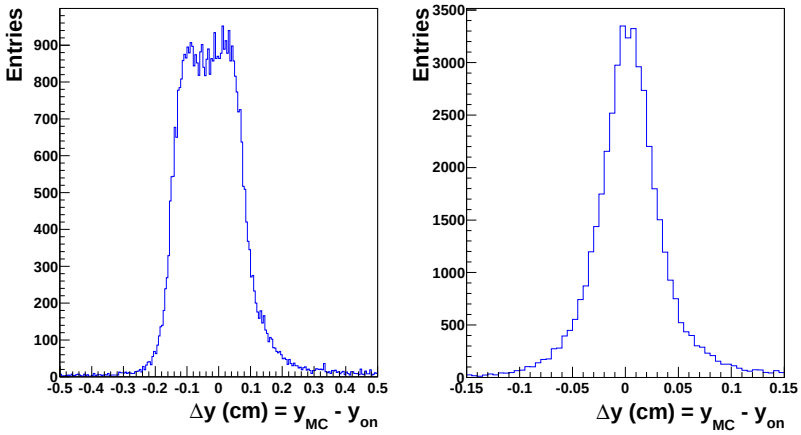

Figure 7.19: *Position resolution plots for layer 1 comparing online tracklets and Monte Carlo tracks. Left panel: uncorrected distribution, right panel: tilted pad corrected distribution. Note the change of scale for the y-axis.*

tilted by an angle of 2° in opposite direction for consecutive layers. As expected their rotation point is located at $\Delta z = 0$. In such a case a projection on the y-axis is strongly influenced by the pad tilting as depicted in the left panel of figure 7.19. Figure 7.18 shows the situation after the correction using equation 7.8. The distribution is now tilted back by an angle of 2°. A projection on the y-axis (figure 7.19, right panel) now leads to the real resolution without the impact of the tilted pads. On the basis of this plot the intrinsic resolution σ_y can be determined in the same way as outlined in section 7.1.4.

Figure 7.20 summarizes the resolutions σ_y and σ_x for different layers. σ_y takes values between 214 μm and 337 μm and shows the expected behavior for ascending layers. For the lower layers the resolution is comparable to results found in [Wul09], but for the upper layers deviations appear. In the next section local y-positions on a pad are reviewed to check whether the position **L**ook **U**p **T**ables (LUTs) are filled with useful values. The value σ_x has improved in comparison to section 7.2, but it is still more than three times as large as in [Wul09]. An appropriate setting of the tail cancellation filter is explored in section 8.2 to investigate the x-resolution.

7.4 Adjustment of Look Up Tables

The resolutions found in the previous section have improved in comparison to the GTU fit and the difference to offline tracklets, but the rapid growth in the upper layers leaves a negative impression. The increase of the resolution can already be observed in figure 7.18 since the width of the distribution has nearly doubled from layer 0 to 5. Section B.1 of the appendix shows the projection of the two dimensional distribution for all layers. Regarding these plots it becomes obvious that there is still an error in the resolution measurement. While the distributions for the lower layers look quite normal, those of the upper layers lose their Gaussian shape more and more. They have a rather flat maximum and seem to be spread out. To debug this error the tracklet position in local pad coordinates is reviewed in this section. To explore possible correlations of the local tracklet positions on a pad the residuals of online tracklets and Monte Carlo tracks are plotted vs. the local

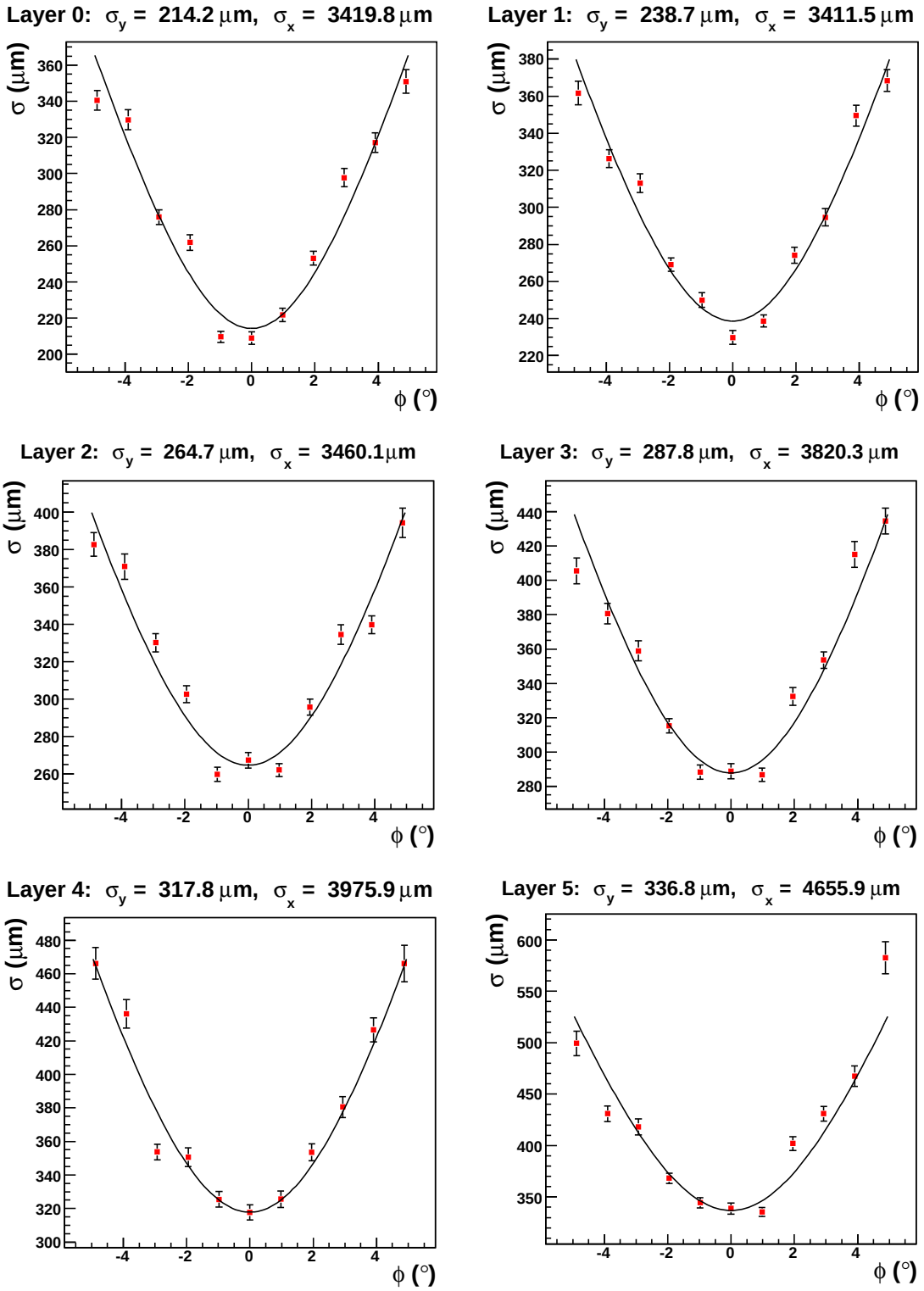

Figure 7.20: *Determination of the intrinsic resolution for Monte Carlo data.*

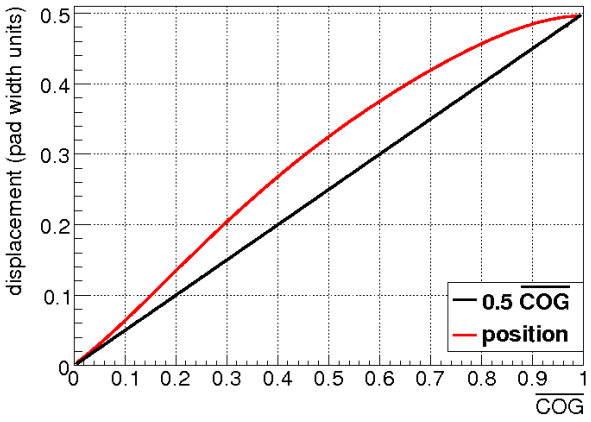

Figure 7.21: *The displacement in pad units is plotted vs. the value $\overline{COG}$ [Wul09]. The red line depicts exact values of the PRF, the black line is based on position calculations by the MCM. As can be seen the deviations do not change the sign for one half of the pad. The deviation curve has the same shape as the residual distributions of figure 7.22 and 7.23 which are used for the corrections.*

coordinate y_{local} of the corresponding pad. Normally, the y-position of the tracklet word is given in local detector coordinates (see section 5.1.1). To relate all tracklets to the same pad and thus to transform the y-position in the pad coordinate y_{local} the following expression is used:

$$y_{\text{local}} = y - \text{floor}\left(\frac{y}{W}\right) \cdot W \tag{7.10}$$

In this equation y denotes the position which is available from the tracklet word and W is the pad width. With this definition figure 7.22 shows the residuals as a function of y_{local}. This graph visualizes the real resolution modulated by another function which resembles the deviation curve from the PRF used for the calculation of the LUTs (see figure 7.21). The amplitude of this modulation increases with growing number of layers. That is why the resolution in the upper layers is much worse than in the lower layers. In the following a method is developed to adjust the LUTs with the information provided by the Monte Carlo track and the tracklet word.

As shortly introduced in section 4.5.4, the PRF is used to calculate a precise y-position of found hits. With the assumption of a Gaussian distributed signal overlapping two or three adjacent pads, the y position can be obtained by [Wul09][5]:

$$y = \frac{W}{2} \cdot \frac{\ln\left(Q_{i+1}/Q_{i-1}\right)}{\ln\left(Q_i^2/Q_{i+1} \cdot Q_{i-1}\right)} \tag{7.11}$$

In this formula Q_i is the charge deposit of the central pad, Q_{i+1} is the deposit of the right neighbor pad, and Q_{i-1} denotes the charge induced on the left neighbor pad. The value W again corresponds to the pad width. On MCM level this equation is not used as

[5] This formula can be extended by different weights to consider two- or three-pad-clusters.

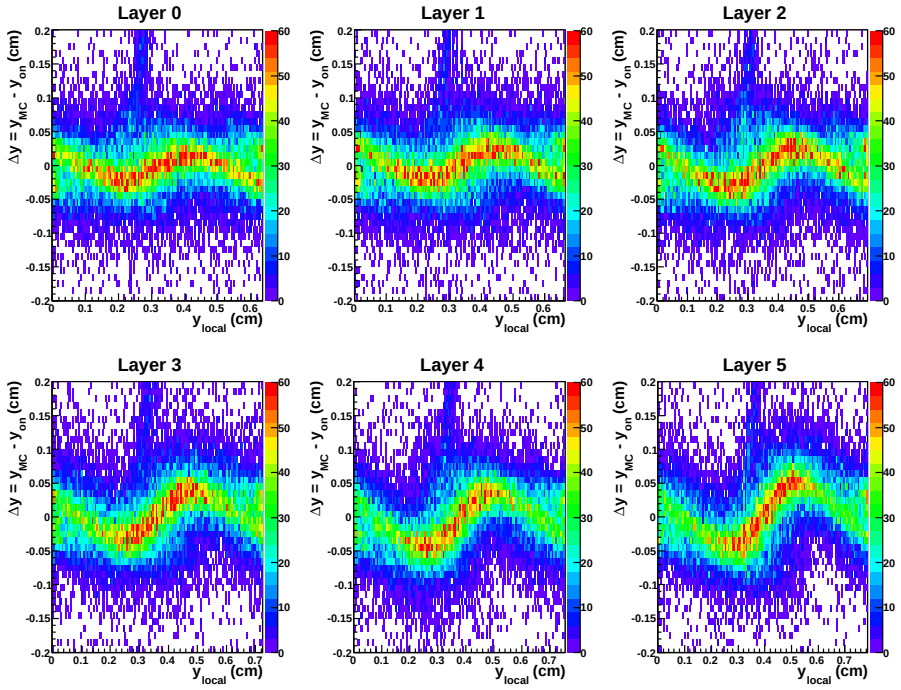

Figure 7.22: *The residuals Δy of Monte Carlo tracks and online tracklets are plotted vs. the local pad position y_{local}. The modulation function deteriorates the resolution measurement. The deviations between the value $\overline{COG}$ and the exact PRF deliver a function which resembles the modulation function so that by adjustment of the LUTs (using these plots) the deterioration can be removed.*

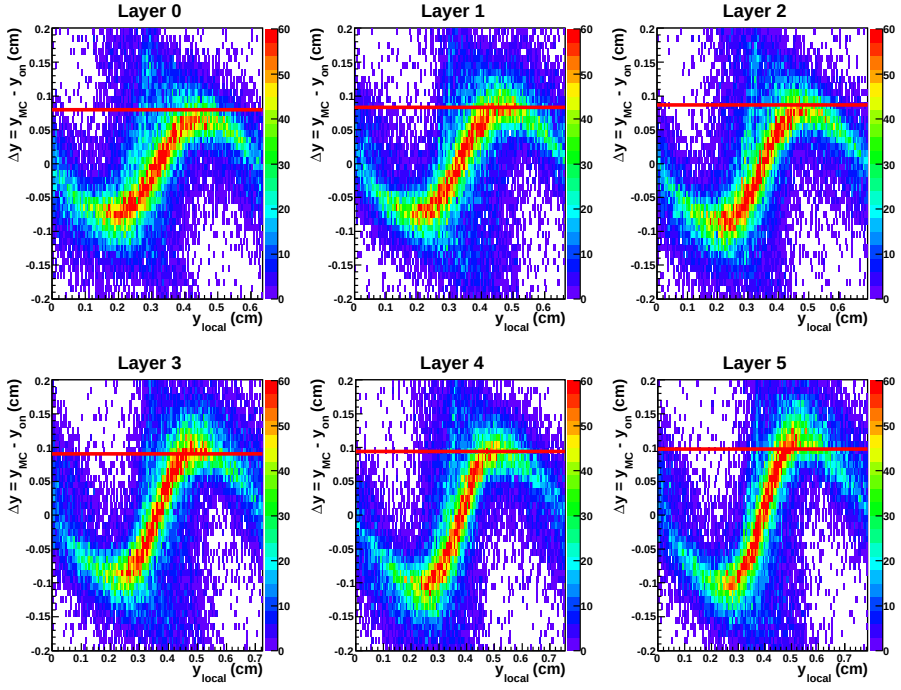

Figure 7.23: *In this plot all LUT standard entries are set to zero to define a starting point for the correction. As expected the amplitude of the modulation increases. The red line marks the border of the LUT register size.*

this rather elaborate formula requires several arithmetic operations which would extend the number of gates in the arithmetic units considerably. To save time the PRF can be approximated for example by formula 4.5 that only consists of a division of the charge deposits. Instead, for the implementation in the MCM, the value $\overline{COG} = \frac{Q_{i+1}-Q_{i-1}}{Q_i}$ as described in equation 5.7 is used. Regarding the value $\overline{COG}$ for half a pad width the deviations to the exact values of the PRF do not change the sign. The deviations are smallest at the center of the pad and at its borders. This is visualized in figure 7.21 by plotting $\overline{COG}$ vs. the displacement in pad units. The systematic shifts in relation to the PRF can be corrected by each MCM using its own position LUT which can be filled with a maximum of 128 entries. At the middle of the pad the deviations change the sign but their distribution (see figure 7.22 and 7.23) is symmetric with respect to the origin. That is why the calculation can be limited to half a pad width. Due to the symmetry, the calculated values for the LUT can easily be applied to the other half of the pad. To fill the LUTs, half of the pad width is subdivided into 128 parts. For each part the deviation to the exact PRF is calculated. The values in the LUTs can be stored with a precision of 8 bits after the decimal point and are restricted to a range of [0.000, 0.125] [A$^+$05]. The deviations have to be calculated in units of pad width/256 so that with this restriction values up to 32 (pad with/256) are possible.

To calculate reasonable values for the LUTs the plots of figure 7.23 are used. For these plots the standard entries of the LUTs were all set to zero in the MCM simulation. At first, the distribution plot for each layer is subdivided into two parts so that the pad is cut exactly at the center. The right part is used for further calculations, the left part is discarded. The horizontal axis of the new distribution is then discretized by 128 bins. This plot is the starting point for the calculation of the deviations in order to fill the LUTs as explained above. Instead of using deviations of the PRF, the residuals between online tracklets and Monte Carlo tracks serve to correct the LUTs. This procedure is necessary since the tracklet word does not contain the charges Q_n with $n \in \{i-1, i, i+1\}$. To obtain the value for the residual $\Delta y = y_{MC} - y_{on}$ at the respective bin of y_{local}, the cut distribution is projected on the vertical axis for each of the 128 bins. The bin of the newly created one dimensional histogram which possess most entries is then marked[6] and the corresponding residual Δy is multiplied by 256, divided by the pad width and inserted in one of the 128 entries of the LUT. Figure 7.24 shows the results of this method for layer 4. Based on these parameter settings for the LUTs, the MCM was simulated again. Figure 7.25 shows the residuals Δy as a function of y_{local} after this simulation. As can be seen from this picture the amplitude of the modulation that deteriorated the resolution in figure 7.22 has decreased after the adjustment of the LUTs. While in layer 0 and 1 the distribution is perfectly aligned to the horizontal axis, the modulation is still present in the upper layers. The reason for this is the restriction of the LUT value the maximum of which is 32 (pad width/256). After a transformation into units of mm this value would correspond to a residual of about $\Delta y = 1$ mm in layer 5. However, figure 7.23 shows that some of the calculated residuals exceed this value so that they cannot be corrected entirely since the size of the LUT register is not sufficient to store larger values. That is why the

[6] This procedure is used instead of mean values. The mean values did not provide reasonable entries for the LUTs as there are too much fluctuations within the residuals Δy. For the maximum method a granularity of 50 μm per bin was chosen.

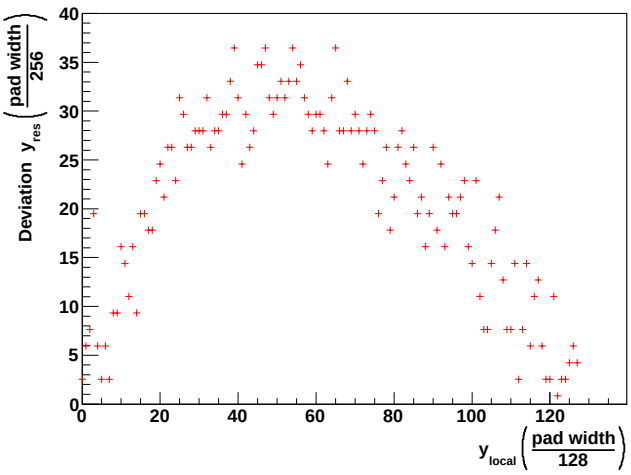

Figure 7.24: *Creation of the LUT in layer 4. To obtain the LUT values the right half ($y_{local} > 7.55/2$ mm) of the distribution in figure 7.23 (layer 4) is regarded. The axis of y_{local} is discretized with a binning of 128 so that for each bin the displacement can be stored in a LUT register. For each bin the distribution is projected on the Δy-axis. The bin (granularity 50 μm) with maximum entires of this histogram is used to decide which value of Δy to take for the LUTs.*

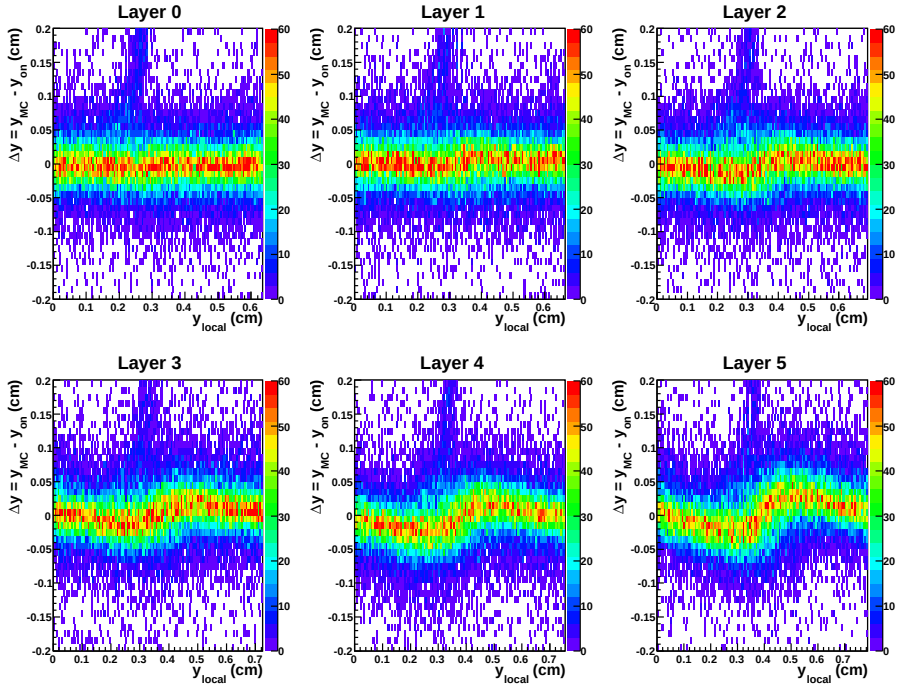

Figure 7.25: *Residuals Δy plotted vs. the local pad position after adjustment of the LUTs. The amplitude of the modulation decreases obviously. The LUTs of the upper layers could not be corrected entirely because of the limited size of the LUT registers.*

shape of the modulation can still be recognized. In the lower layers the correction almost exclusively includes residuals that are smaller than the restricted size of the LUTs, thus the LUT correction succeeds.

Section B.2 of the appendix summarizes the resolution plots of Δy (all incident angles ϕ included) for all layers after the adjustment of the LUTs. Contrary to the distributions before the correction of the LUTs, the functions have a 'real' Gaussian shape. Moreover, the resolution improved by up to 100 μm in layer 5 where the wrong LUT settings influenced the resolution measurement most. Figure 7.26 shows the plots for the intrinsic resolution σ_y. For layers 0 and 1 values of 170 μm and 180 μm are close to the numerical limit of the tracklet word. The resolution again grows for the upper layers but it was finally improved by the adjustment of the LUTs. An important result is that the origin of the fast growth of the resolution is known by now.

7.5 Summary of Resolution Measurements

In this section the results of the different resolution measurements are depicted. The first one was a quality fit which proved that the tracklets are suitable for a statistical analysis. However, this method is strongly influenced by the tilted pads. Further on, the GTU fit was performed to correct this influence. Since the vertex constraint did not work in the TRD test setup using cosmic rays the results did not provide the expected values. Thereafter, a comparison to offline tracklets was performed. The results improved, but they were not sufficient to draw a final conclusion about the quality of online tracking. When Monte Carlo data was used the primary vertex assumption was valid and the tilted pads could be corrected successfully. This procedure is the most reliable tool to determine the position resolution of the online tracking procedure. In the previous chapter the LUTs were adjusted so that the resolution for Monte Carlo simulations could be improved further. In figure 7.27 the y- and x-resolution for different layers obtained by these different steps (except the GTU fit) is shown.

In addition to the simple line which was used for the comparison to Monte Carlo tracks, the residuals of a straight line fit through all the 12 references of the 6 layers were performed for resolution measurements[7]. The result of this fit can be found in section B.3 (figure B.3, left panel) of the appendix. The distribution of the residuals between the Monte Carlo y-positions and the fit is shown in the right panel. Though the Monte Carlo track should lead to an optimum precision, a resolution of 79.4 μm is worse than expected. Possible deviations could originate from scattering processes at the detector volumes. The resolution of the Monte Carlo positions for single layers is summarized in table B.1. The fit does not seem to work properly as the values show fluctuations with a certain symmetric pattern. The deteriorations from scattering processes are suppressed when using the simple line since the resolution is much better as it is depicted in figure 7.27. On average the residuals Δy of the simple line undershoot those of the MC fit by about 25 μm. In layer 5 these deviations are even about 40 μm. This is an important insight as scattering processes naturally happen during the data taking in the cosmic setup, too. This implies the straight line fit performed in section 7.1.2 suffers from this deterioration as well.

[7]The resolution for this method is indicated by the term 'MC Fit' in Figure 7.27. The resolution is based on calculations before the LUTs were corrected.

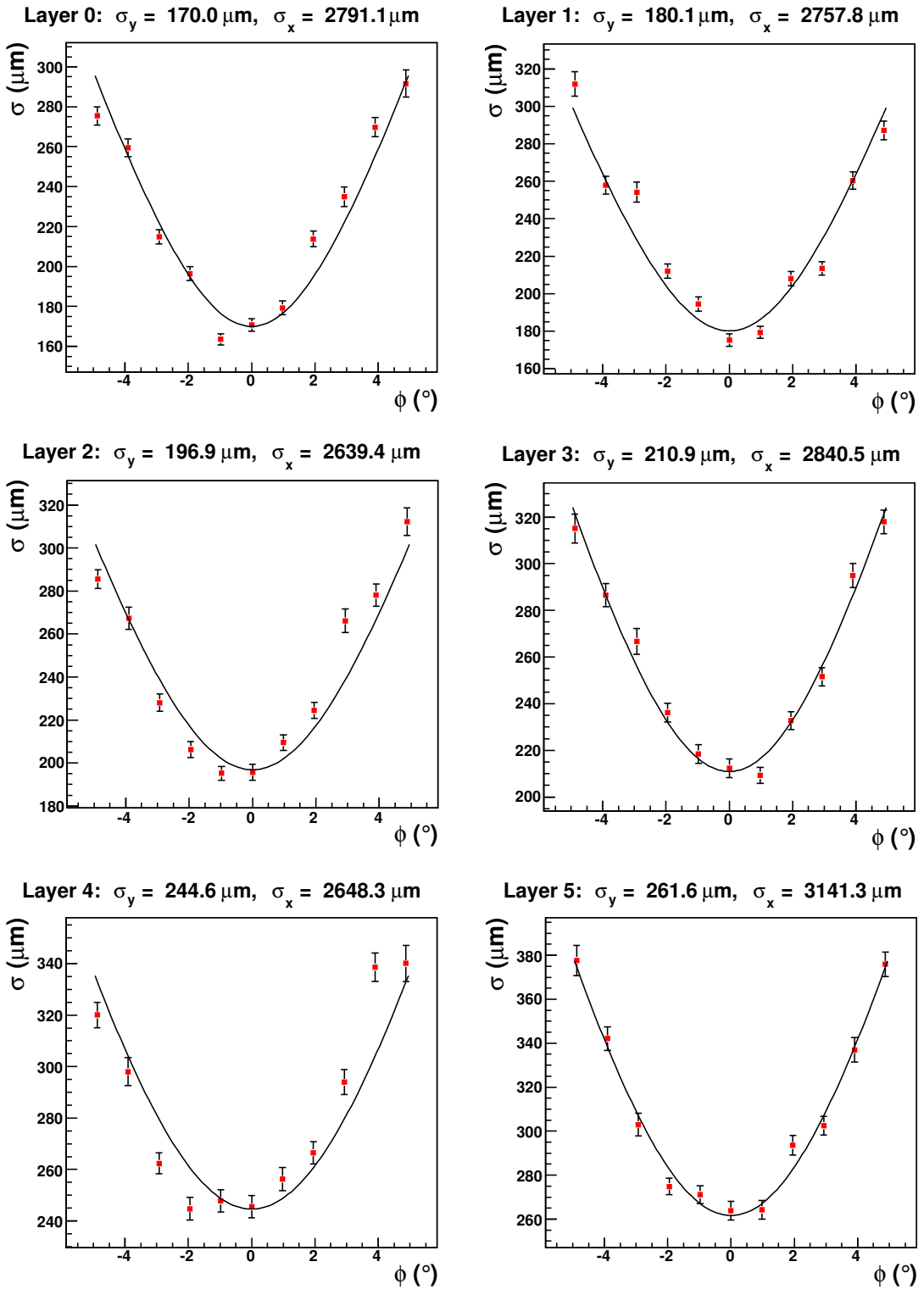

Figure 7.26: *Resolution of online tracklets by a comparison to Monte Carlo tracks after the adjustment of the LUTs as a function of ϕ.*

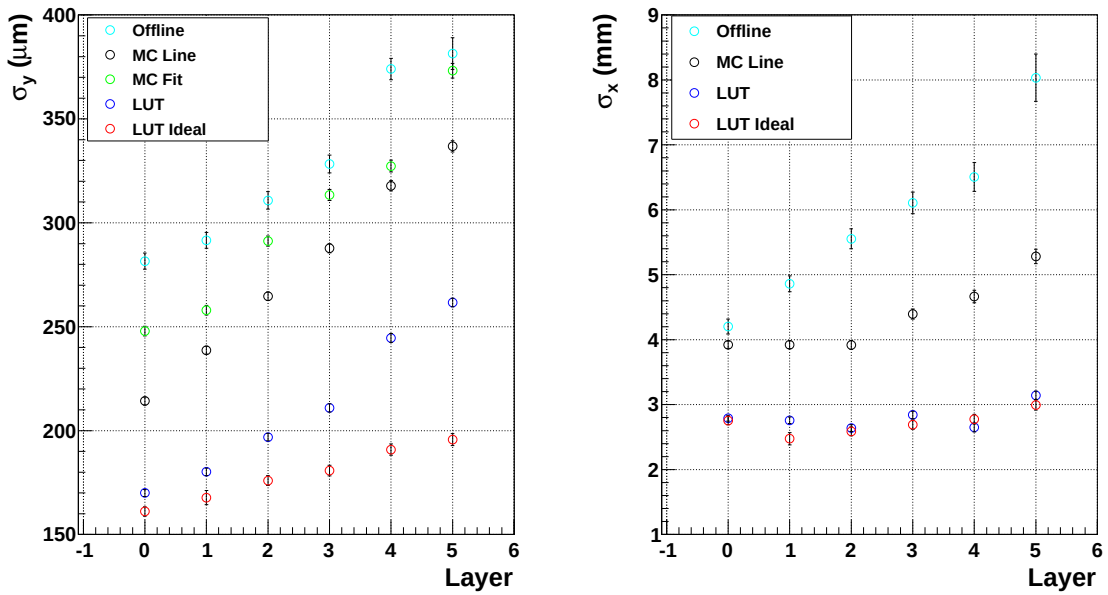

Figure 7.27: *Results of the y- and x-resolution for different comparisons.*

The term 'LUT' inserted in the legend of figure 7.27 stands for resolution measurements after the correction of the LUTs. As discussed in section 7.4 the LUTs of the upper layers could not be corrected entirely because of the restriction in size of the particular register. The term 'LUT Ideal' means the resolution which can be obtained in case the LUTs are corrected more accurately. To obtain this resolution a cut is performed on $y_{\text{local}} >$ pad width/2 so that the projection is less influenced by the modulation function. The result (red circles) is that the y-resolution for all layers is below 200 μm. For the ideal LUT correction the growth of the resolution in the upper layers is suppressed as can be seen from the large discrepancy between the red and the blue circles. Since the size of the LUT registers cannot be changed in the hardware MCMs anymore this ideal resolution is not available in reality.

8. Angular Resolution and Tail Cancellation

As discussed in section 7.1.3 the slope of the tracklet is used for the projection inside the GTU to find a track. Furthermore, in section 5.2.3 was mentioned that the first p_t cut is already performed on MCM level. To obtain this p_t threshold the information of the tracklet deflection is necessary according to formula 5.13. In section 8.1 the angular resolution of online tracklets is explored in order to check whether the tracklets can be used for the purposes mentioned above. As the Monte Carlo tracks are the best possibility for a comparison, Monte Carlo data is used exclusively in the subsequent discussion. The MCM simulator again runs on the `TRDDigits.root` file obtained during the simulation. The MCM settings are retained from the previous chapter and the LUTs as calculated in section 7.4 are used.

To obtain the correct angular resolution the tilted pads have to be corrected by a projection of the tracklet slope pointing to the vertex. As all primary Monte Carlo tracks originate from the same point ($\vec{r} = (0, 0, 0)$) this procedure can easily be applied. The algorithm for the correction is depicted in section 8.1.1. In addition, the drift velocity has to be adjusted in case of angular distributions to access the slope of online tracklets and Monte Carlo tracks on the same level. This discussion takes place in section 8.1.2. The intention in section 8.2 is to apply the tail cancellation filter in order to study the effects on the position and the angular resolution.

8.1 Resolution Measurement

In this section the angular resolution is determined by comparing the slope of the Monte Carlo tracks and the slope of online tracklets. Before the final resolution measurement, the tilted pads and the drift velocity have to be considered.

8.1.1 Tilted Pad Correction

Initially, the pad tilting has to be corrected. In reality this is already done on MCM level. Contrary to the pad correction of chapter 7 the angular correction does not consume much CPU time since the precise z-position is not required in this case. In section 5.2.3 the formula

$$dy' = dy + dy_{\text{Lorentz}} + dy_{\text{tilt}} \tag{8.1}$$

was introduced. The Lorentz and tilted pad corrected quantity dy' is written to the tracklet word. As there is no magnetic field set in the Monte Carlo simulations (see section 7.3.1) the deflection dy_{Lorentz} is zero. The value dy_{tilt} is set to zero initially to show the influence of the pad tilting, but it will be corrected right afterwards with the formula [dC03]:

$$dy_{\text{tilt}} = (-1)^L \frac{z_{\text{row,middle}} \cdot dx_{\text{drift}}}{x_L} \cdot \tan\left(\beta_{\text{tilt}}\right) \tag{8.2}$$

In this equation dx_{drift} stands for the length of the drift region, x_L is the x-reference position of the particular layer L, $z_{\text{row,middle}}$ is the middle of the padrow just as in equation 7.8, and β_{tilt} is the tilting angle. This is the formula which is used to calculate the correction for the deflection inside the MCM, but in the current mode of the simulator it is bypassed. In the examples shown below the correction is done manually to highlight the effect of the tilted pads.

8.1.2 Setting of the Correct Drift Velocity

In order to access online and Monte Carlo information on the same level, the correct drift velocity has to be found as the MCM does not calculate the tracklet slope in local coordinates internally. This slope can easily be adjusted by a multiplication factor stored in a register inside the MCM. The factor has to be set to the number of timebins that corresponds to the length of the drift region. This factor is multiplied by the slope either to make the tracklets steeper or to flatten them. In the previous chapter the correct drift time was not set. It simply did not influence the position calculation because the position of the x-reference, where the y-position is measured, is the rotation point of the slope. Therefore, any rotation will keep the measurement of the y-position invariant.
In the following the residuals between the slope of Monte Carlo tracks $\left(\frac{dy}{dx}\right)_{MC}$ and online tracklets $\left(\frac{dy}{dx}\right)_{on}$ are used quite often. From now on the expression for this difference is:

$$\Delta d = \left(\frac{dy}{dx}\right)_{MC} - \left(\frac{dy}{dx}\right)_{on} \tag{8.3}$$

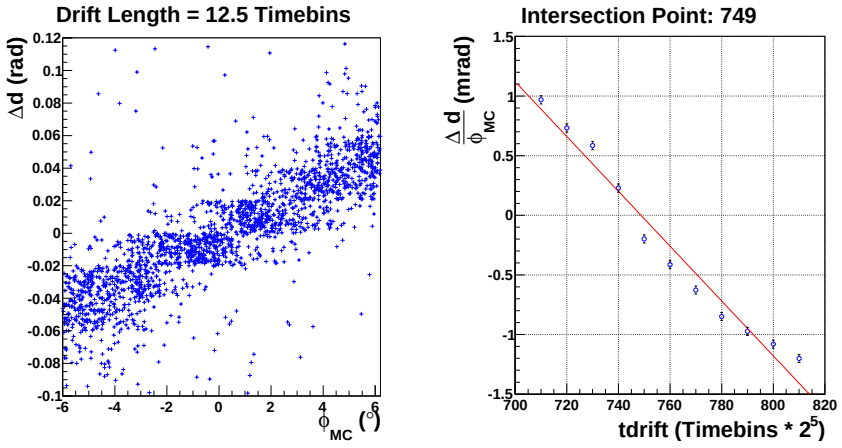

Figure 8.1: *Left panel: residuals of Monte Carlo track and online tracklet slope plotted vs. the track angle ϕ for a drift value of $tdrift = 400 = 12.5 \cdot 2^5$. To flatten the slope the drift value has to be increased. Right panel: the slope of the linear fit based on plots as shown in the left panel is inserted for values of tdrift between 710 and 810. The intersection point with the vertical axis denotes the value where track and tracklet angle coincide.*

In order to find the correct drift velocity, Δd is plotted against the Monte Carlo track angle (see figure 8.1). Using the slope, the corresponding angle in the x-y-plane can be calculated by:

$$\phi = \arctan\left(\frac{dy}{dx}\right) \tag{8.4}$$

In case the slope of the linear fit which can be performed in the left panel of figure 8.1 reaches a value of zero, the track and tracklet angles coincide. The drift value can be set within the MCM simulation using the function `AliTRDtrapConfig::cnf` → `SetDmem(0x025, tdrift)`. The first argument depicts the address of the MCM register. The parameter $tdrift/32$ corresponds to the number of timebins and is set with a precision 2^{-5}. In the right panel of figure 8.1 the slopes obtained from calculations as shown in the left panel are plotted against $tdrift$. The intersection point between the linear fit and the origin of the vertical axis then yields the corrected drift value. According to this plot a drift value of $tdrift = 749$ which is equal to 23.40625 timebins corresponds to the correct tracklet slope. In the further discussion this slope is set in the simulations. This drift time is much longer than the drift plateau of the pulse height plot of figure 7.14. A possible explanation is the influence of ion tails which distort the tracklet slope (see section 8.2).

8.1.3 Angular Resolution

Figure 8.2 depicts angular resolution plots for layer 1 that are calculated by comparing the slope of Monte Carlo tracks and online tracklets. In the upper left panel the distribution without tilted pad correction is shown. The distribution is obviously shifted to the left. With application of formula 8.2 this deterioration can be corrected as it is depicted in the right panel. The distribution plots for all layers can be found in sections C.1 to C.3 of the appendix. In section C.1 the pad tilting can be recognized since the distributions are shifted in opposite direction for consecutive layers just as shown for the positions in the previous chapter. In the bottom panel the residuals are plotted against the Monte Carlo track angle and similar behavior like in the case of position resolutions becomes obvious. By increasing $|\phi|$ the angular resolution deteriorates. Based on this plot the resolution can be calculated for single angle intervals with the same discretization as introduced in section 7.1.4. Figure 8.3 shows these graphs for all layers. The minimum is located at $\phi = 0$ and corresponds to steep tracklets. In this case the impact of the drift value and its error is minimized. Indeed, the drift value is not the only error that occurs, but the angular resolution can be improved by a precise knowledge of the drift velocity. Above all, the resolution for this small angle interval benefits from the fact that the knowledge of the exact x-position of the deposited charge does not influence the measurement. The results obtained from these distributions can be seen as ideal resolutions $\sigma_{\Delta\mathrm{d,ideal}}$. The data points of figure 8.3 are fitted with function 7.7 though the quantity σ_x of this formula has no explicit meaning in this context. However, the variable σ_y can be identified with the ideal angular resolution $\sigma_{\Delta\mathrm{d,ideal}}$.

At this point a worthwhile question is in which way this resolution impacts on the relevant physical observables as e.g. the transverse momentum. The variables deflection dy and

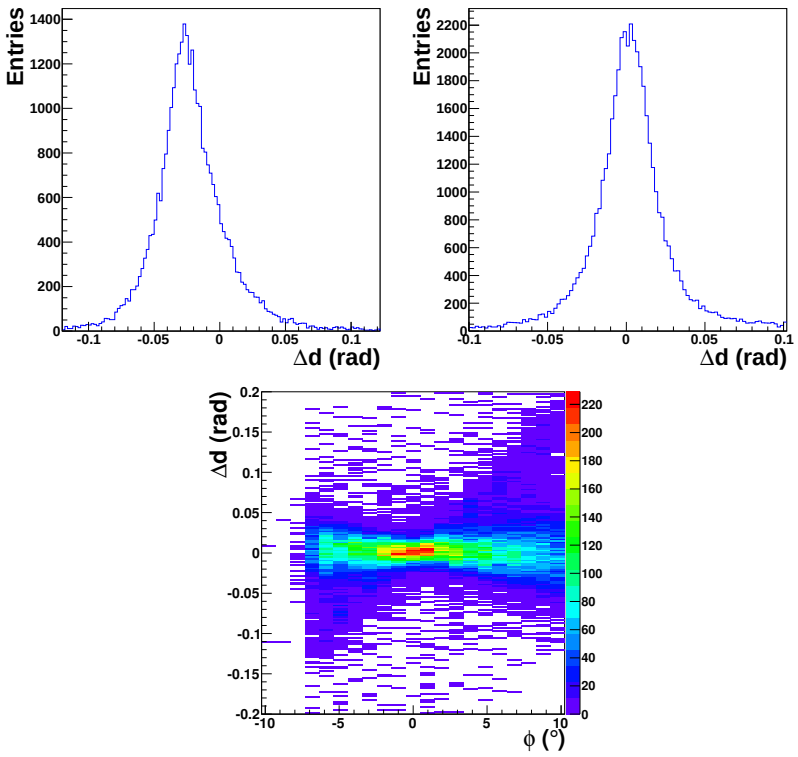

Figure 8.2: *Resolution plots by comparing the slope of Monte Carlo tracks and online tracklets (layer 1). Upper left panel: uncorrected distribution, upper right panel: tilted pad corrected distribution. In the bottom panel the residuals are plotted against the MC track angle to show the behavior for single angle intervals. The upper distributions do not show a pure Gaussian shape. This is due to the superposition of many Gaussian functions for different incident angles ϕ.*

deflection angle ϕ are explored additionally. To estimate the error of these variables the standard error propagation law is used without consideration of correlations. It reads:

$$\Delta f = \sqrt{\sum_{i=0}^{n} \left(\frac{\partial f(x_1, ..., x_n)}{\partial x_i} \cdot \Delta x_i \right)^2} \tag{8.5}$$

In this formula the cumulative error of an observable f as a function of x_i with $i \in [0, n]$ and a respective error Δx_i is calculated. In the subsequent discussion the error of the transverse momentum is simply calculated as a function of the error Δd since especially the influence of the angular resolution shall be studied. Hence, only the case $i = 0$ is considered:

$$\Delta f = \left| \frac{\partial f(x_1, ..., x_n)}{\partial x_0} \cdot \Delta x_0 \right| \tag{8.6}$$

The error Δdy for the deflection can be calculated by:

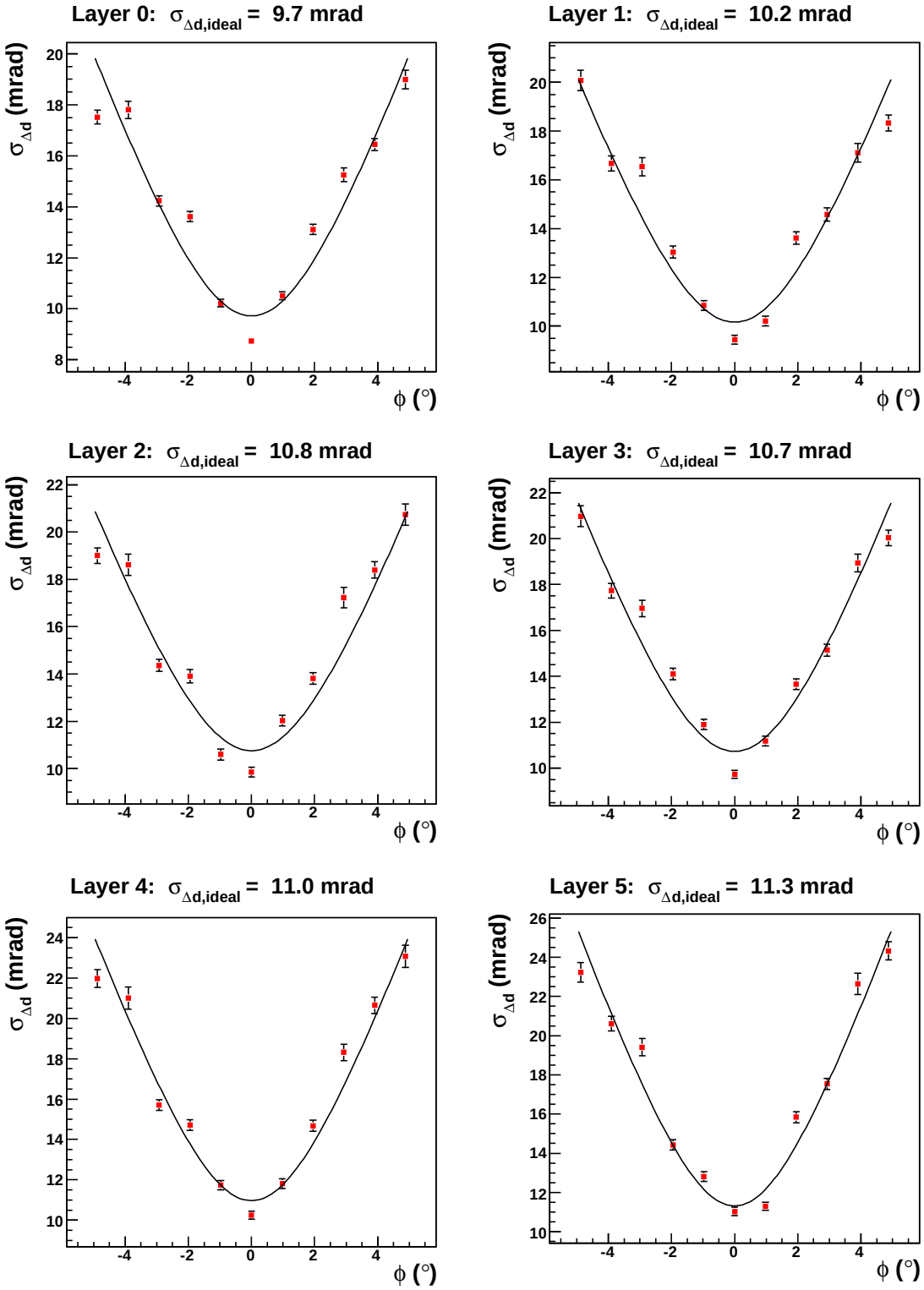

Figure 8.3: *Calculation of $\sigma_{\Delta d}$ as a function of the Monte Carlo track angle ϕ. $\sigma_{\Delta d,ideal}$ is the minimum value of the resolution obtained from these plots and it corresponds to steep tracklets.*

$$\begin{aligned} dy &= \left(\frac{dy}{dx}\right)_{on} \cdot dx_{\text{drift}} \qquad \Rightarrow \qquad \frac{\partial dy}{\partial \left(\frac{dy}{dx}\right)_{on}} = dx_{\text{drift}} \\ \Delta dy &= 3 \text{ cm} \cdot \Delta d \end{aligned} \tag{8.7}$$

Δd is the resolution that can be taken from the plots in section C.2 including all angle intervals or with regard to the ideal case from figure 8.3. The error $\Delta\phi$ for the deflection angle can be calculated as follows:

$$\begin{aligned} \phi &= \arctan\left(\left(\frac{dy}{dx}\right)_{on}\right) \qquad \Rightarrow \qquad \frac{\partial \phi}{\partial \left(\frac{dy}{dx}\right)_{on}} = \frac{1}{1+\left(\frac{dy}{dx}\right)^2_{on}} \\ \Delta\phi &= \frac{\Delta d}{1+\left(\frac{dy}{dx}\right)^2_{on}} \end{aligned} \tag{8.8}$$

Now the question arises which value to take for $\left(\frac{dy}{dx}\right)_{on}$? As mentioned in section 5.2.3 the default parameter for the p_t threshold is chosen to be 2.3 GeV/c. Assuming this value, the deflection angle α according to formula 5.13 can be calculated:

$$\alpha = \arcsin\left(\frac{erB}{2 \cdot p_t}\right) \tag{8.9}$$

As introduced in section 5.2.3, α is the tracklet angle with respect to the vertex direction. The relevant angle ϕ is given by equation 5.14: $\phi = \alpha + \phi_{\text{vertex}}$. For simplification reasons, in the subsequent error estimation the vertex direction matches the x-axis with respect to local detector coordinates, so that $\phi_{\text{vertex}} = 0$. Hence, α and ϕ are equalized from now on. The global position $r = \sqrt{x^2 + y^2}$ can be chosen as a general position in TRD: for example by using the local coordinates $y = 0.2$ m and $x = 3.1$ m $\Rightarrow r = 3.106$ m. The B-field is 0.4 T and e is the electric charge. Based on the choice of these parameters, ϕ is $\approx 4.6°$ and $\left(\frac{dy}{dx}\right)_{on}$ has a value of about 0.08.
The error estimation for the transverse momentum is likewise performed in this region. As mentioned above no errors for the positions x and y[1] are assumed, as especially the influence of the angular resolution shall be explored. The error estimation for Δp_t reads:

$$\begin{aligned} p_t &= \frac{erB}{2 \cdot \sin(\phi)} \qquad \Rightarrow \qquad \frac{\partial p_t}{\partial \phi} = \frac{-erB}{2} \cdot \frac{\cos(\phi)}{\sin^2(\phi)} \\ \Delta p_t &= \Delta\phi \cdot \frac{erB}{2} \cdot \frac{\cos(\phi)}{\sin^2(\phi)} \end{aligned} \tag{8.10}$$

[1] These positions are unrelated to those written to the tracklet word. As they are stored in the particular MCM where the tracklet is found these values are rather imprecise.

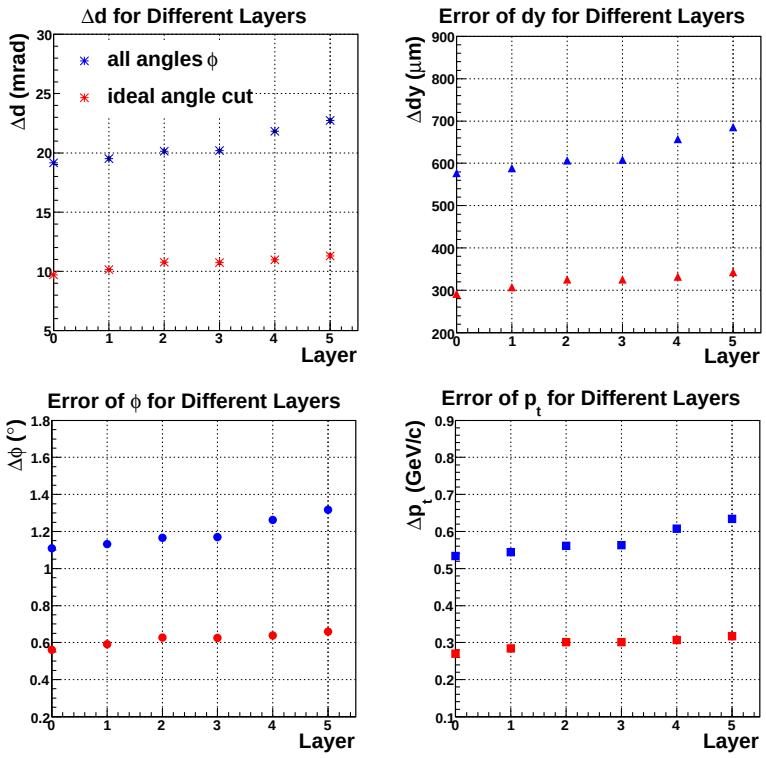

Figure 8.4: *Overview of the errors of the physical observables calculated by the formulas 8.7, 8.8, and 8.10. The points marked in blue are based on resolution measurements of figure C.2, whereas the red points correspond to the ideal case with the resolution* $\sigma_{\Delta d,ideal}$ *obtained from figure 8.3.*

Figure 8.4 gives an overview of the error estimations as explained above. As the angular resolution of online tracklets was not explored before these values are difficult to interpret. Since the cut on the transverse momentum on MCM level is not intended to be particularly sharp a deviation of about 0.5 to 0.6 GeV/c is acceptable. Considering the fact that the drift velocity can be determined more precisely, this resolution can be further improved. In the ideal case (steep tracklets) the values are about 0.3 GeV/c.

In the current condition the online tracklets provide a sufficient resolution to contribute to the p_t cut which is the first step of the TRD's L1 decision.

8.2 Tail Cancellation

8.2.1 The Functionality of a Tail Cancellation Filter

The time response of the detector is strongly influenced by the slowly moving positive ions that induce the signal on the padplane. Figure 8.5 shows the time response function created by a MAGBOLTZ/GARFIELD simulation. It consists of a fast increasing part in scales of nano seconds and a long tail which extends for microseconds. This ion tail not only provides a signal in a single timebin but also in subsequent bins on the same pad.

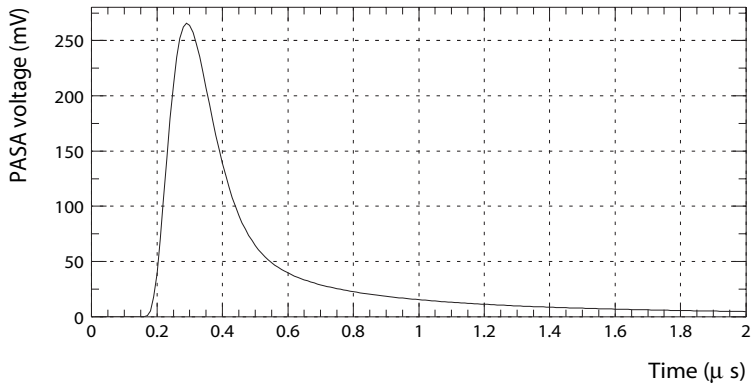

Figure 8.5: *Time response function for a TRD chamber generated with Magboltz/Garfield [trd01].*

This superimposes and deteriorates the signal produced in the following timebin which itself influences the next timebins by its own ion tail. Above all, these deteriorations will affect the angular as well as the spatial resolution performance. The **T**ail **C**ancellation (TC) filter is a tool to correct the influences of the time response function in different timebins. This section explores whether such a filter improves the angular and x-position resolution in the online tracking procedure.

The tail can be approximated by two exponential functions which describe the temporal behavior of the gas amplification and the front-end electronics:

$$S(t) = \alpha_L \cdot e^{\kappa_L t} + \alpha_S \cdot e^{\kappa_S t} \qquad \text{with } t \geq 0 \tag{8.11}$$

The first part describes a fast, the second a slow decay. In the MCMs this formula is implemented by using three independent coefficients:

$$S(t) = \alpha_L \lambda_L(t) + (1 - \alpha_L)\lambda_S(t) \qquad \text{with } \lambda_i(t) = e^{\kappa_i t} \tag{8.12}$$

With a chosen granularity of 2^{-11} the range of the parameters is defined as [A$^+$05]:

$$\begin{aligned} \alpha_L &\in [0, 0.5 - 2^{-11}] \\ \alpha_S &= (1 - \alpha_L) \\ \lambda_L &\in [0.75,\ 1 - 2^{-11}] \\ \lambda_S &\in [0.25,\ 0.5 - 2^{-11}] \end{aligned}$$

With the help of this formula the TC filter subtracts the previously created ion tails of the respective timebins. Using the Aliroot class `AliTRDtrapConfig` the three parameters are available in form of:

$$\begin{aligned} \text{FTAL} &= \alpha_L \cdot 2^{11} \\ \text{FTLL} &= (\lambda_L - 0.75) \cdot 2^{11} \\ \text{FTLS} &= (\lambda_S - 0.25) \cdot 2^{11} \end{aligned} \tag{8.13}$$

For simulations the parameters FTAL = 246, FTLL = 285, and FTLS = 211 appeared to be reasonable [Kle09]. From now on these values are set in the MCM simulations and the bypass FTBY is switched off.

8.2.2 MCM Parameters for Tail Cancellation

For the resolution measurements with TC the fit range is set to TPFS = 4 and TPFE = 19 as introduced in section 7.3.2. Furthermore the thresholds TPHT, TPCL and TPCT have to be adjusted. In the former analyses including Monte Carlo simulations these values were set to TPHT = 210, TPCL = 4, and TPCT = 12, but were not discussed further.

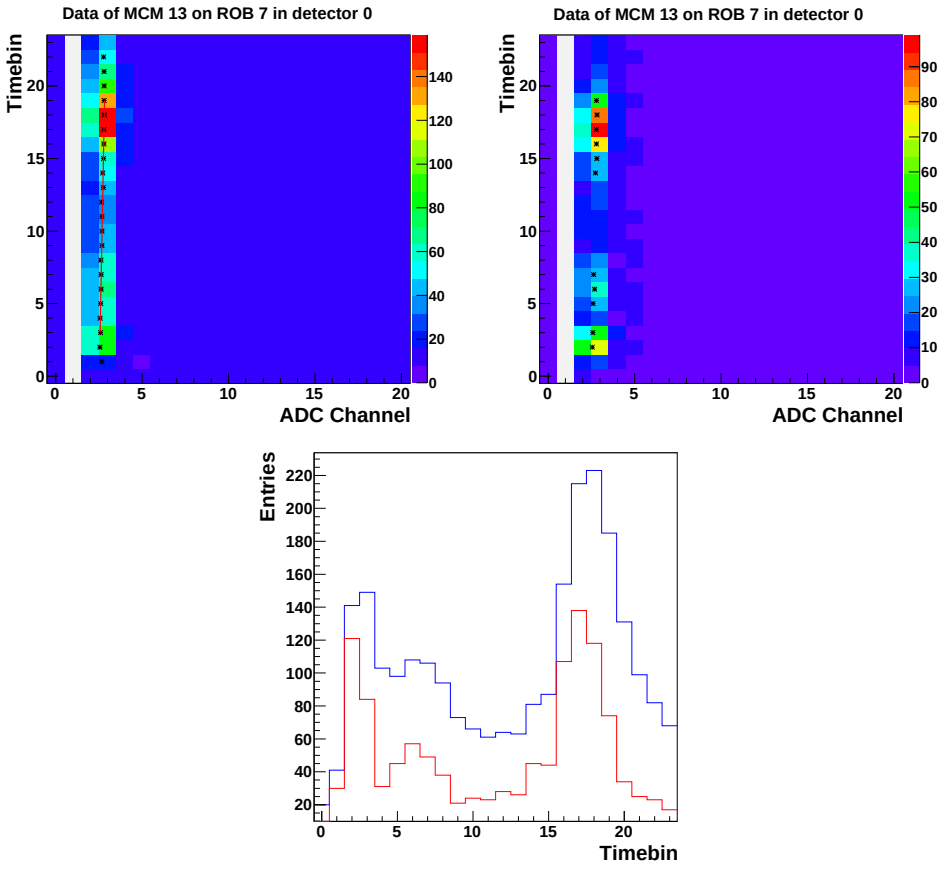

Figure 8.6: *Top left panel: signal recording of the MCM without TC filter, top right panel: signal recording of the MCM with TC filter, bottom panel: pulse height plot of the upper cases. With application of the TC filter the signal is reduced substantially.*

As TC reduces the amplitude of the signal in different timebins these parameters have to be reviewed once again. In the upper panels of figure 8.6 the signal distribution of MCM channels in different timebins is shown. In the left panel the TC filter was bypassed, whereas in the right panel it was applied[2]. In timebins 17 and 18 a signal with a large amplitude is induced. Consequently, the ion tail provides an increased signal during the subsequent timebins. This impact is rather large compared to the influences of the ion tails of the earlier timebins which are much lower in amplitude. This causes positions in channel 3, which are calculated by the PRF, to be displaced in the timebins 19 to 21 as the signal induction is much larger due to the artifact of the tail. Therefore, the center of gravity moves in the direction of channel 3 and the position is calculated wrongly with a shift to the right. Without the influence of the tail the center of gravity would be more balanced between channels 2 and 3. Thus, a direct impact of the angular resolution is expected since the slope used for resolution measurements is obtained by the cluster fit. With the application of the TC filter not only the influence of the ion tail decreases, but also the whole signal is reduced. Therefore, less hits are found inside the fit range so that with the current setting of the cluster thresholds no tracklet is fitted (see figure 8.6, right panel). Consequently, the application of TC strongly impacts on the efficiency of the tracking procedure. The bottom panel shows a projection of the 2 dimensional distributions on the time axis summing up the channels 2 and 3. In this context the blue distribution depicts the projection without TC and the red curve with TC applied. In this plot the impact of the signal in timebins 17/18 and its ion tail becomes obvious since the tail even exceeds the amplification peak. The influence of the tail is reduced substantially after TC was applied. In timebin 0 the signal has a value of 20 ADC units before filtering. As two channels were used for the projection this value corresponds to the pedestal of 10 ADC units. After filtering, timebin 0 only has a value of 8 ADC units[3] which corresponds to a pedestal of 4 ADC values per channel. As introduced in section 5.2.5 the baseline is intended to be 10 ADC values after the filtering. That is why the filter register FPNP is set to 23 ADC values to balance the signal reduction of the filter procedure.

The adjustment of the pedestal value indeed heightens the whole pulse height plot of figure 8.6, but the signal lost in most of the timebins is much larger. In order not to loose to many of the tracklets the threshold TPHT has to be reduced, too. A reasonable compromise has to be found as too small values of TPHT would contribute to a substantial contamination by noise. To find such a value the left panel of figure 8.7 visualizes the behavior of found clusters as a function of TPHT. Regarding the standard settings for Monte Carlo simulations without TC, 17.2 clusters were found on average. Figure 8.7 (left panel) shows that this number is only reached when going far below the noise and pedestal level. From now onwards the hit threshold will be set to TPHT = 150. At this value 15.2 clusters are found on average and thus only two clusters less, compared to the standard values without TC. To compensate the reduction by two clusters both cluster thresholds are also decreased by two so that their values are TPCL = 2 and TPCT = 10.

[2]There is no pedestal value set in channel 1. The origin of this error is not obvious. As it is an individual case and was not noticed in other MCM visualizations it is simply ignored.

[3]This is not really visible in the plot (it shows zero) due to the binning.

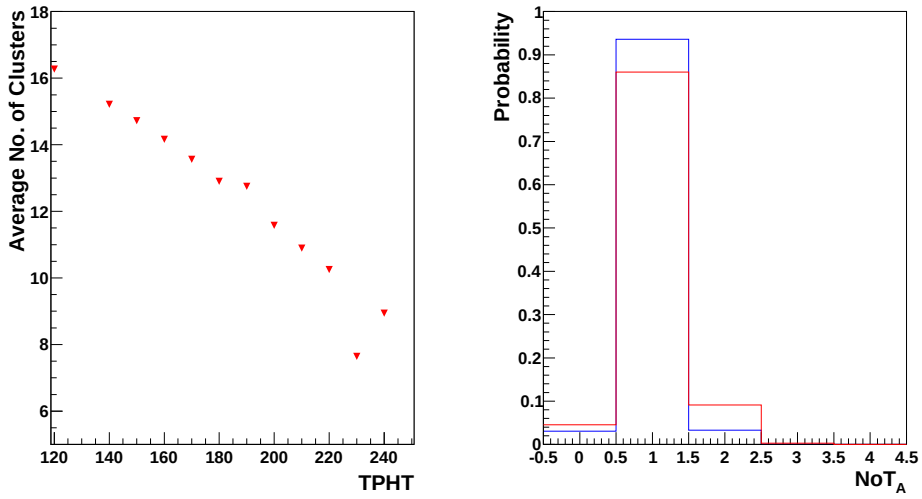

Figure 8.7: *Left panel: number of found clusters after TC as a function of TPHT. To reach the usual value of about 17 clusters the noise level has to be undershot. Right panel: efficiency measurements without TC (blue) and with TC (red) as introduced in section 6.2.2. After application of TC, the efficiency is still acceptable with the new MCM parameter setting.*

	Monte Carlo without TC	Monte Carlo with TC
TPFS	4	4
TPFE	19	19
TPHT	210	150
TPCL	4	2
TPCT	12	10
FPNP	$40 = 4 \cdot 10$	$92 = 4 \cdot 23$

Table 8.1: *Overview of new MCM parameters.*

In order to confirm the validity of these new thresholds two efficiency plots as introduced in section 6.2.2 are shown in figure 8.7 (right panel). The blue one is based on the standard variables for Monte Carlo simulations without TC. The red line corresponds to efficiency measurements that include a TC filter with the new MCM parameters. For the blue line the efficiency with about 94 % is excellent and loss as well as splitting are small with values below 2 %. After the application of the TC filter the efficiency decreases as expected, but with a value of about 86 % it is still fine. The splitting increases to 10 %. This fact is undesired for resolution measurements as explained in chapter 6, but difficult to prevent since the signal-to-noise ratio worsens by using the TC filter. Table 8.1 once again summarizes the settings for Monte Carlo simulations before and after the application of the TC filter.

8.2.3 Angular Resolution

Before calculating the final angular resolution with the application of the TC filter, the drift velocity has to be adjusted again. The procedure was explained in section 8.1.2. It was stated that a drift velocity of about 1.3 cm/μs which corresponds to a drift time of about 23.4 timebins does not match the drift plateau of the pulse height plot. Figure 8.8 visualizes the calculation of the new drift time. With a value of $642 \cdot 2^{-5} = 20.0625$ timebins it is smaller after the application of the TC filter. It does not exactly match the drift length of the pulse height plot but this value contributes to a better approximation. With this drift time the angular resolution and the resulting errors for the variables dy, ϕ, and p_t as introduced in section 8.1.3 are calculated including the TC filter (see figure 8.9). The resolution improves for layers 0 to 2 and deteriorates for layers 3 to 5. This effect again points to the LUT parameters which are not optimal for the upper layers. For layer 0 and 1 the TC filter provides an improvement of about 50 μm for the deflection, 0.1° for the deflection angle, and 50 MeV/c for the transverse momentum.

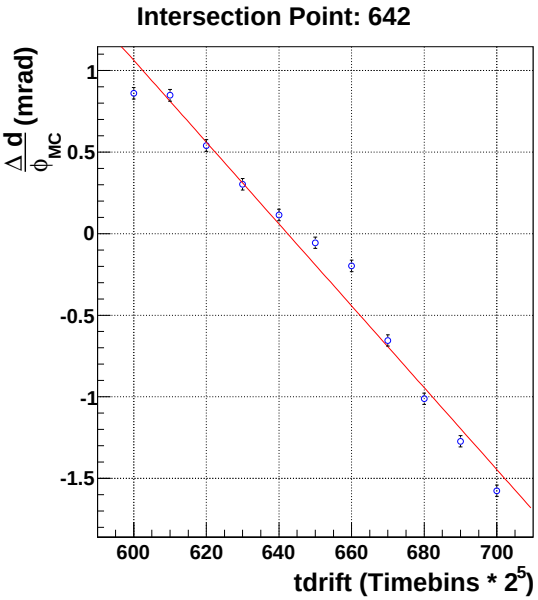

Figure 8.8: *Adjustment of the new drift time after TC. As expected the number of timebins now matches the pulse height plot better.*

8.2.4 Position Resolution

In this section the final results for the x- and y-position resolution after application of the TC filter are depicted. The tail cancellation filter should reduce the influence of the ion tails along the time axis and therefore improve the time- and x-resolution. The result of figure 8.10 (left panel) verifies this assumption for layers 0 to 3. Regarding layer 4, both resolutions are equal, whereas for layer 5 the resolution with TC is even worse. This is caused by the LUT parameters which could not be corrected entirely in the upper layers. The discrepancy of the two resolutions for the lower layers of about 1.2 mm gives an impression of the benefit using a tail cancellation filter in case the LUTs can be adjusted correctly. The new x-positions (only in layers 0 to 2) now match the results found in [Wul09] quite well. Contrary to x the y-resolution should deteriorate since the TC filter reduces the signal-to-noise ratio substantially. Figure 8.10 (right panel) shows this effect. For the lower layers the deterioration is about 100 μm, whereas for the upper layers it rapidly grows due to the influence of the LUT parameters so that for layer 5 a discrepancy of about 150 μm can be recognized.

To sum up, the TC filter provides results as expected. Indeed, for the lower layers the angular and x-resolution could be improved a bit, but in the upper layers the resolution

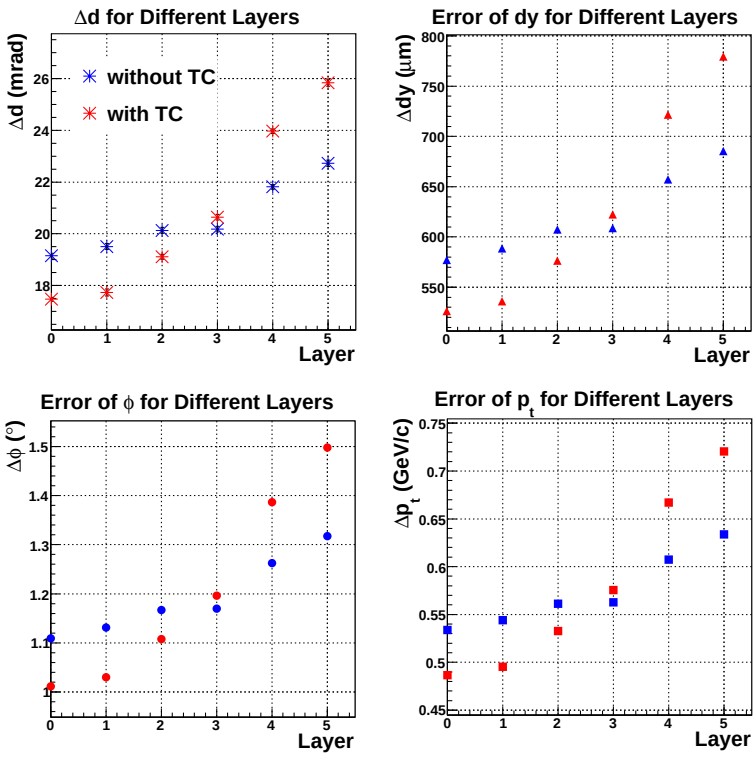

Figure 8.9: *Angular resolution (averaged over all incident angles ϕ) and error estimations for dy, ϕ, and p_t with TC filter (red) and without TC filter (blue).*

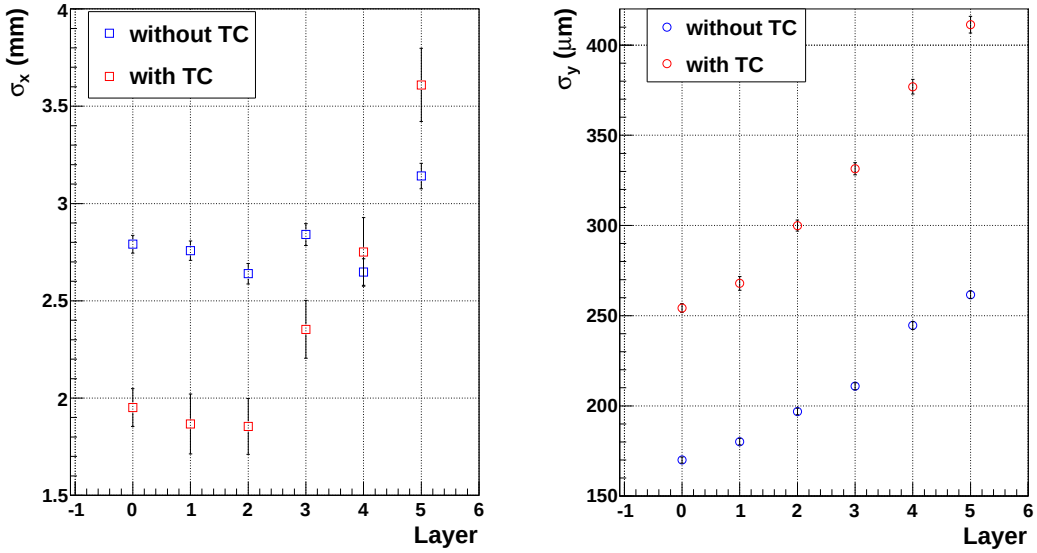

Figure 8.10: *x- and y-position resolution with TC filter (red) and without TC filter (blue). The resolutions are based on the new LUT parameters.*

worsens due to the lack of a reasonable LUT correction. Taking these facts into consideration, the online TC filter should be bypassed at the moment. The parameters for TC are standard values and can possibly be optimized, but as long as the LUTs can not be corrected entirely this filter only should be applied offline.

9. Summary and Perspective

In this thesis parts of the trigger performance of the ALICE TRD were investigated by measuring the efficiency and resolution of online tracklets. These tracklets are the first step for the L1 trigger decision and directly calculated by the front-end electronics mounted on each TRD chamber. They contribute to a first cut on the transverse momentum on MCM level and are used for the track reconstruction inside the GTU.

For this purpose a sufficient efficiency of online tracklets is necessary. In chapter 6 a method was developed to determine the efficiency of online tracklets using cosmic rays. In the course of the analysis the MCM parameters TPHT, TPCL and TPCT were investigated to optimize the efficiency. With the standard MCM parameters an efficiency of about 75 % was reached at the beginning. This was improved by the adjustment of the MCM parameters and now reaches best values of about 93 %. Dependent on the choice of MCM parameters for the cluster thresholds the fraction of tracklet splitting of this efficiency is around 8 % to 9 %. For the final tracking procedure the split tracklets are of minor importance, but for resolution measurements two tracklet events have to be suppressed. In this thesis was shown that best efficiency values are obtained for different parameter settings of TPHT, TPCL, and TPCT. A next step would be to check whether these parameters lead to the same efficiencies for the data taking with collisions at ALICE.

The y-position and the dy-deflection of the tracklet word are necessary for the track finding procedure inside the GTU. In chapters 7 and 8 the resolution of these values was determined. For the position resolution different methods were discussed to receive reasonable and reliable results. The straight line fit based on detector data by using cosmic rays did not work properly due to the influence of the tilted pads. Since the online stream does not contain a precise measurement of the z-position a correction could not be achieved. The GTU fit was not successful either as the vertex constraint failed in the cosmic test setup. A comparison to offline tracklets provided good results for the first time, but this method was more a tool to explore differences between online and offline tracking than a real resolution measurement for online tracklets. Finally, Monte Carlo data was used and the tilted pad correction succeeded. These measurements resulted in values between 170 μm and 262 μm for the intrinsic y-resolution σ_y. The rapid growth of the resolution in the upper layers can be explained by the fact that the LUTs could not be set to optimum values. In case the LUTs could be corrected entirely resolutions below 200 μm are possible. To correct these influences in layer 4 and 5 entirely the size of the registers would have to be extended from 32 (padwidth/256) to around 45 (padwidth/256).

For the angular resolution study, Monte Carlo simulations were used exclusively. After the tilted pad correction was done and the correct drift velocity was applied the resolution for the slopes of Monte Carlo tracks and online tracklets (averaged over all incident angles ϕ) provided resolutions between 19 mrad and 23 mrad. With the application of the tail cancellation filter the angular resolution improved for the lower layers. An error estimation of the transverse momentum at the cut value of 2.3 GeV/c with tail cancellation provides uncertainties of about half a GeV/c for layer 0 and 1 and increases to about 0.7 GeV/c in

layer 5. The x-resolution of the lower layers also benefits from the tail cancellation filter, whereas the y-resolution worsens by activation of this filter (up to 150 μm in layer 5).

Future tasks are a precise review of the tail cancellation filter as in this thesis only standard values were used. By optimization of the parameters FTAL, FTLS, and FTLL the resolution can probably be improved. In the current condition it is not recommended to use the TC filter for online tracking as it only works for the lower layers due to the LUT correction. In addition, the correlation between tracklet position and angle can be studied since these two values are not independent from each other. Based on this correction the y-position resolution can be improved further. In contrast to efficiency measurements the parameters for the hit threshold, the cluster thresholds, and the fit range were not considered so that the adjustment of these values can contribute to another benefit for the resolution. Nevertheless, the final results of the resolution measurements are within the region of expectations.

As a starting point, in this thesis a parameter setting of the MCMs for the online tracking procedure was created. The next step is to to check whether the resolution results can be reproduced by real detector data created in p-p collisions at the LHC this year. To start with, the tracklet stream has to be prepared at ALICE as the tracklet information is not available at the moment. Since in collisions the vertex constraint is valid the tilted pads can be corrected and problems as introduced in chapter 7 do not occur. Therefore, the resolutions obtained by simulations can be compared to real detector data for the first time. In this context, it will be interesting to check the LUTs once more in order to exclude that wrong settings in the simulations caused the problems in the upper layers. If this comparison provides the same results for the LUTs, the rather high resolution compared to the lower layers will remain as the size of the LUT registers cannot be changed in the hardware MCMs anymore

Appendix

A. Efficiency Plots

A.1 z-Distribution

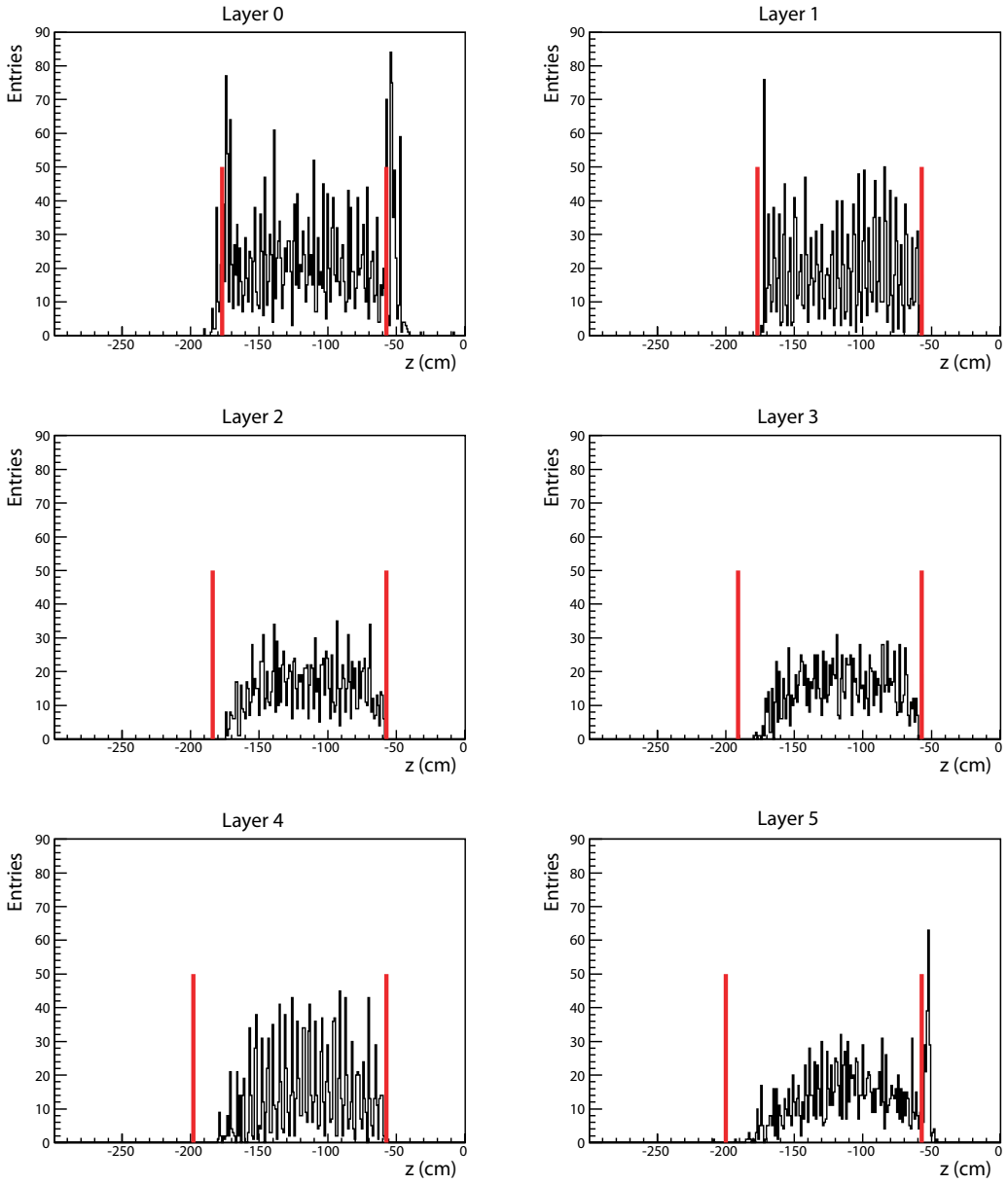

Figure A.1: *z-distribution for lost tracklets of all layers. In contrast to the outer detectors, for the inner detectors the positions are within the red borders of stack 3.*

A.2 y-Distribution

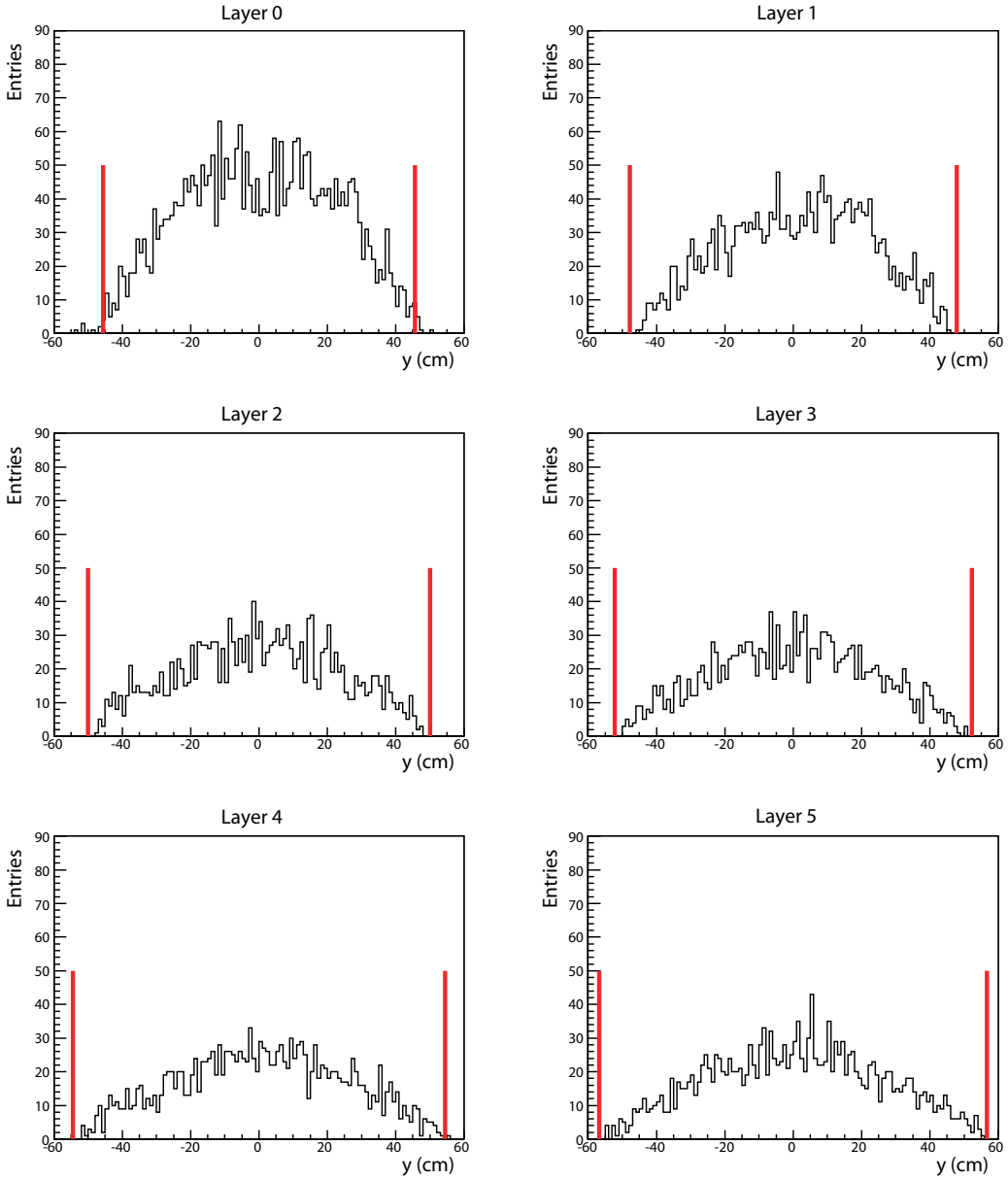

Figure A.2: *y-distribution for lost tracklets of all layers. Due to the trigger setup the positions are inside the red borders.*

A.3 Padplane-Distribution

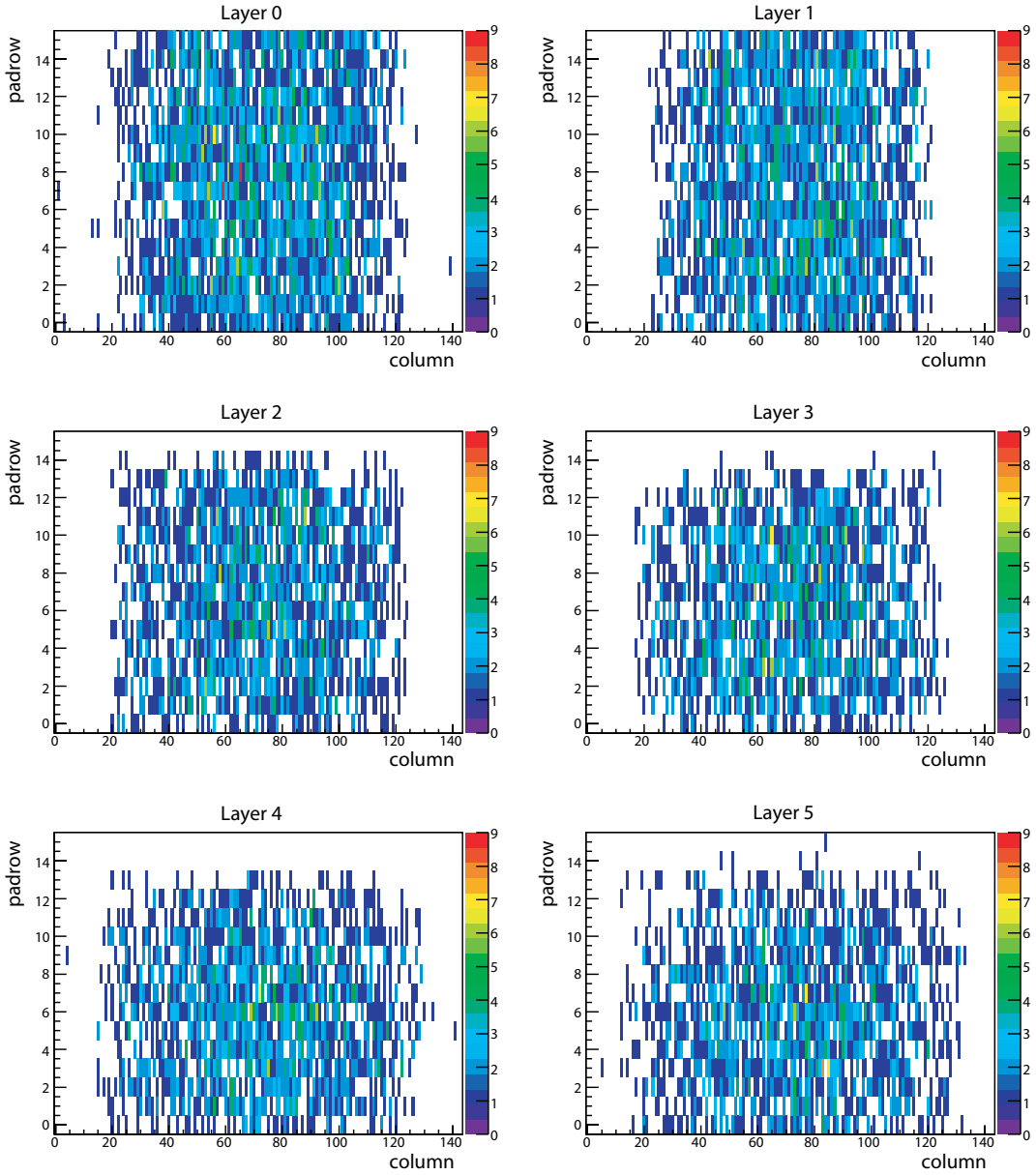

Figure A.3: *Overview of lost tracklets on the padplane.*

A.4 Loss

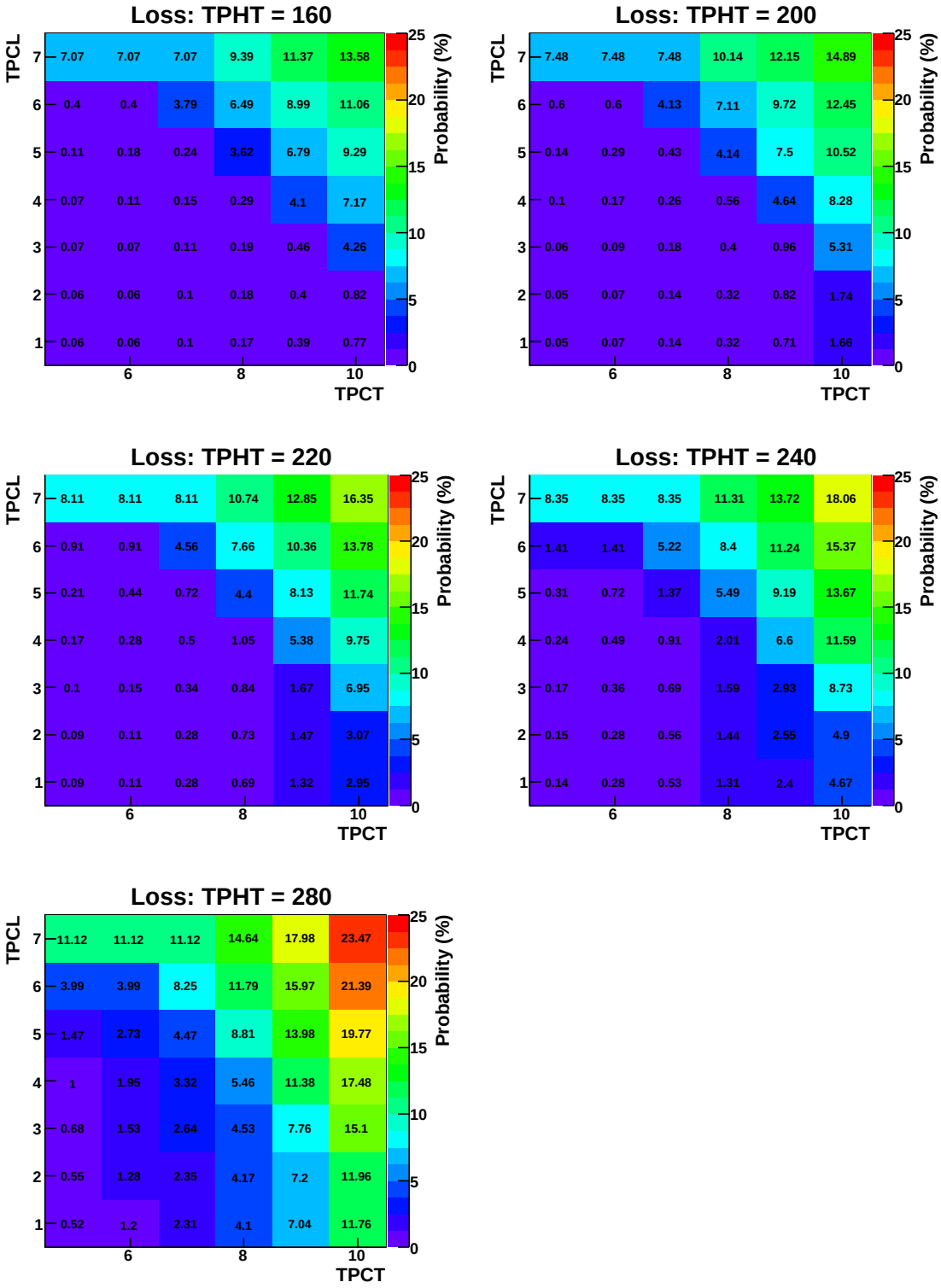

Figure A.4: *Tracklet loss for different values of TPHT, TPCL, and TPCT.*

A.5 Splitting

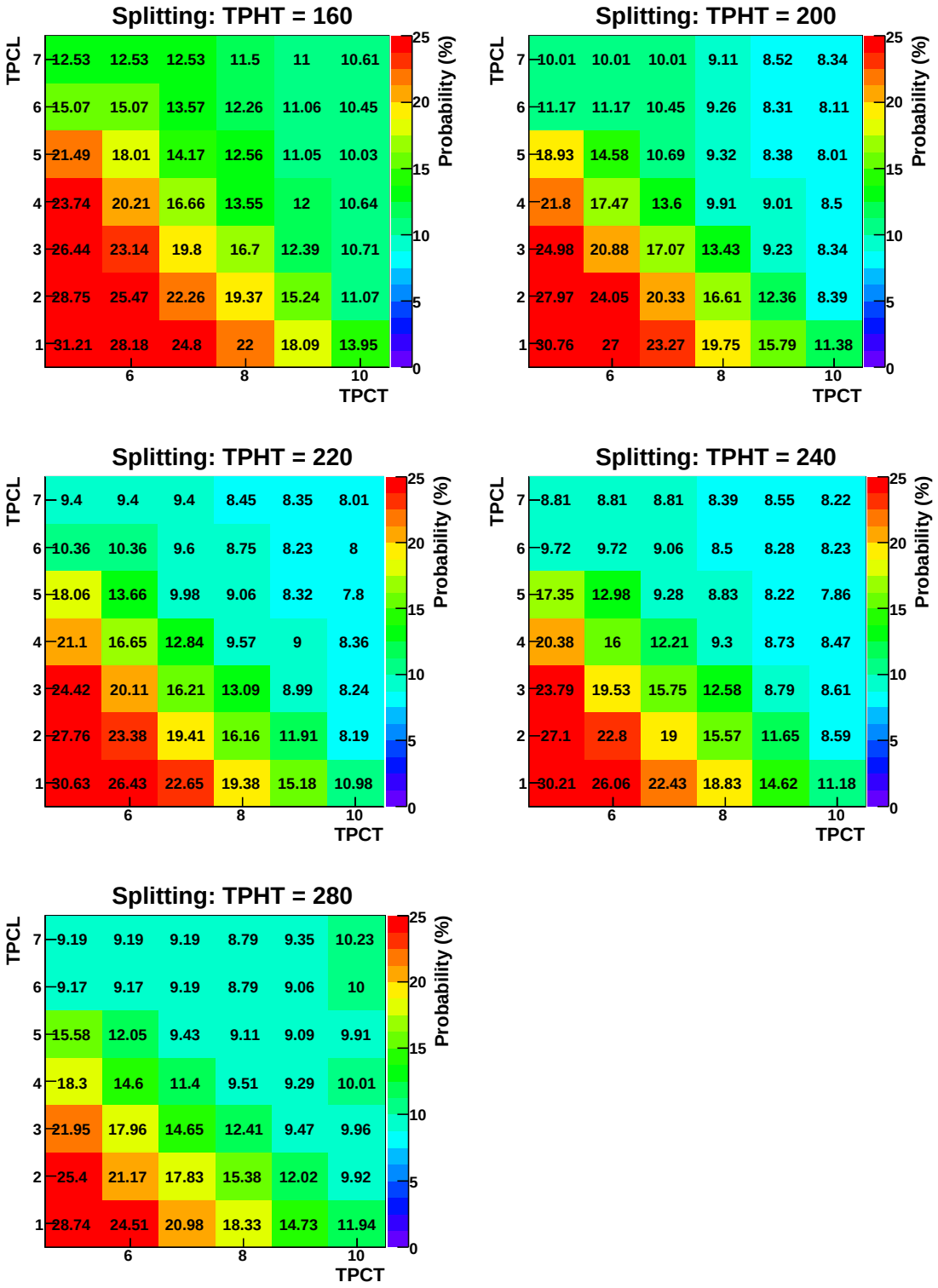

Figure A.5: *Tracklet splitting for different values of TPHT, TPCL, and TPCT.*

A.6 Tracking Efficiency Combined with the Trigger Acceptance

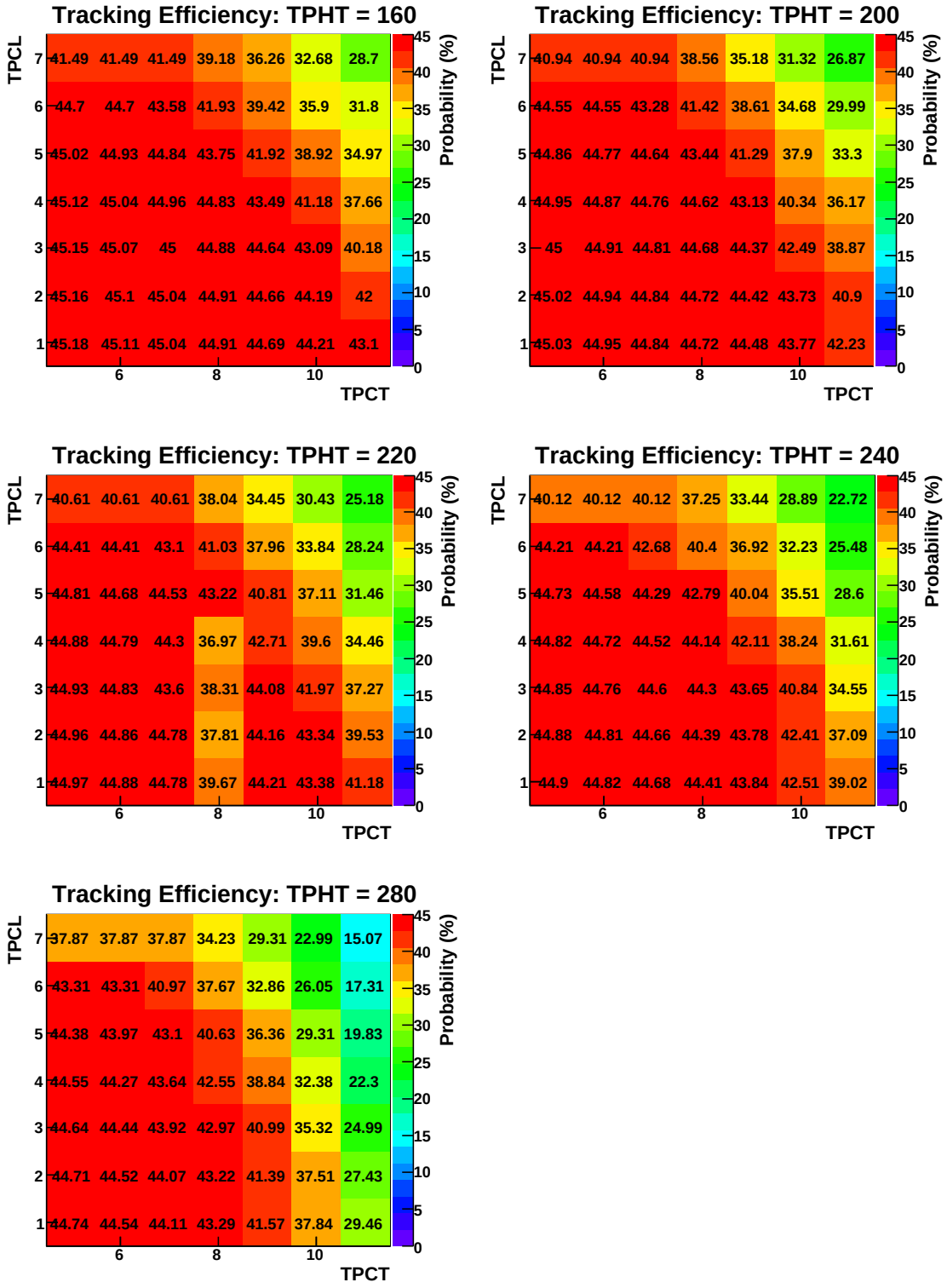

Figure A.6: *Tracking efficiency for different values of TPHT, TPCL, and TPCT. The small values are because of the low acceptance of the cosmic trigger in the coincidence mode.*

B. Position Resolution Plots

B.1 Position Resolution Before Adjustment of Look Up Tables

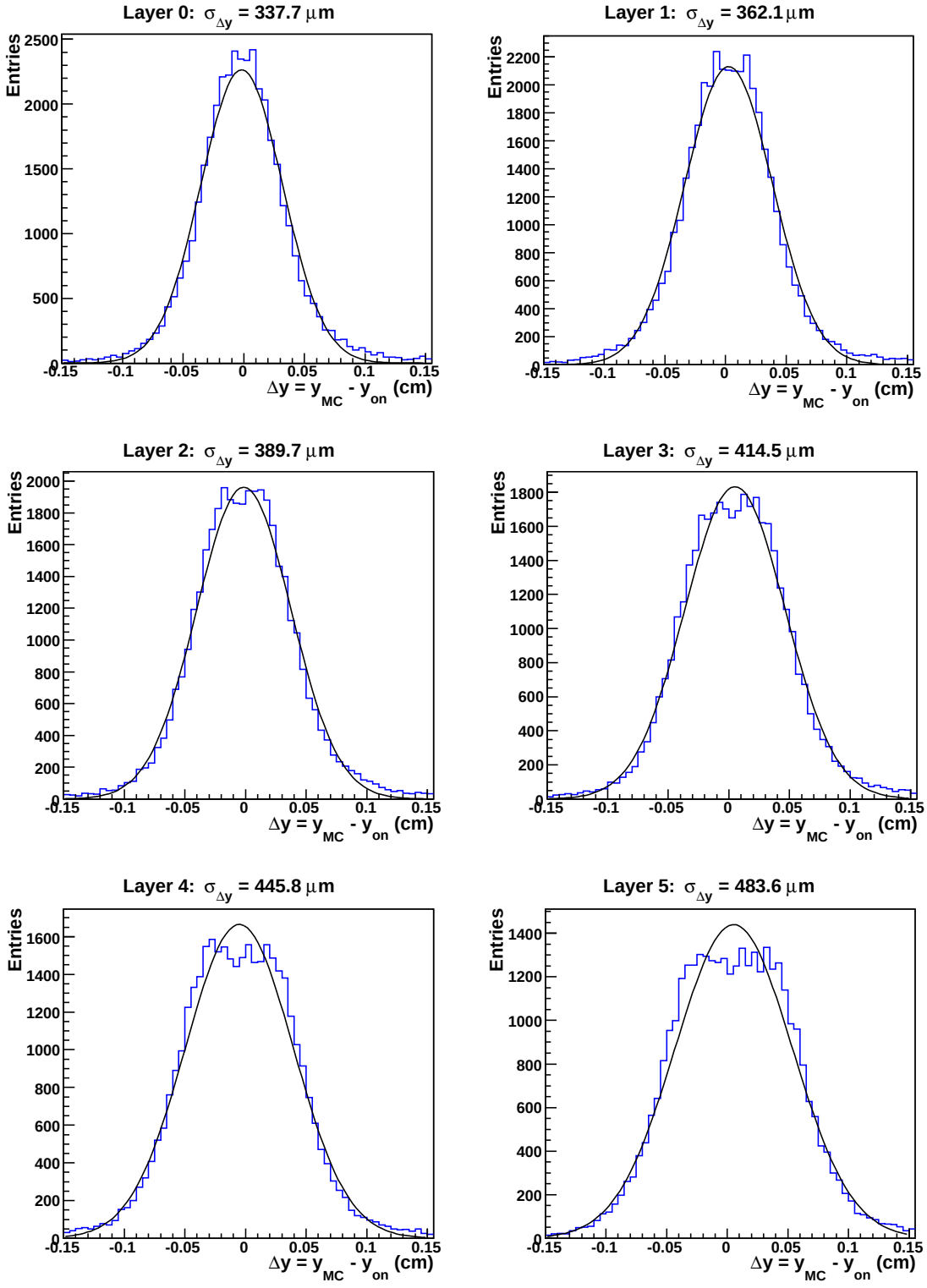

Figure B.1: *Residuals of Monte Carlo tracks and online tracklets before adjusting the LUTs.*

B.2 Position Resolution After Adjustment of Look Up Tables

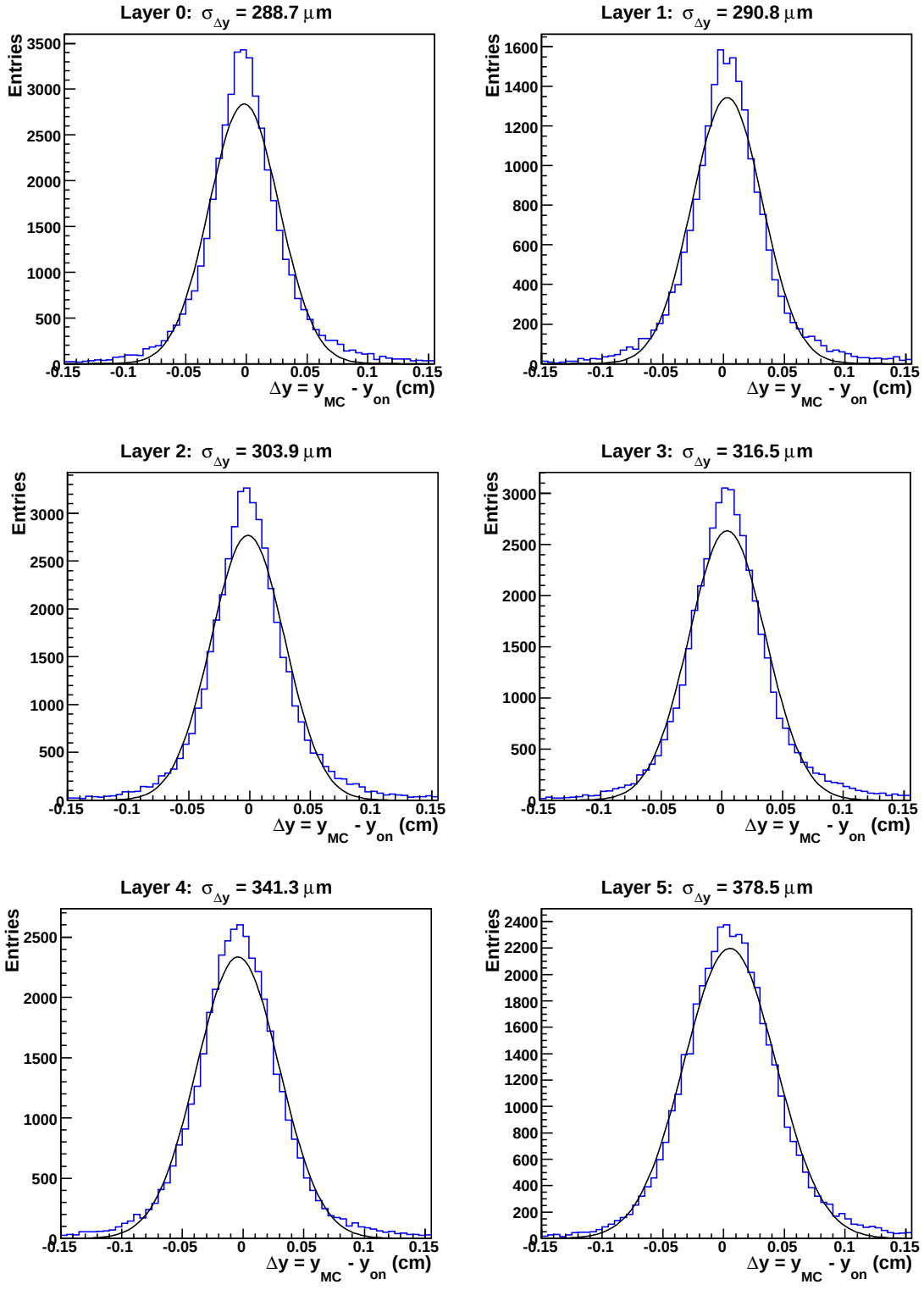

Figure B.2: *Residuals of Monte Carlo tracks and online tracklets after adjusting the LUTs.*

B.3 Monte Carlo Fit

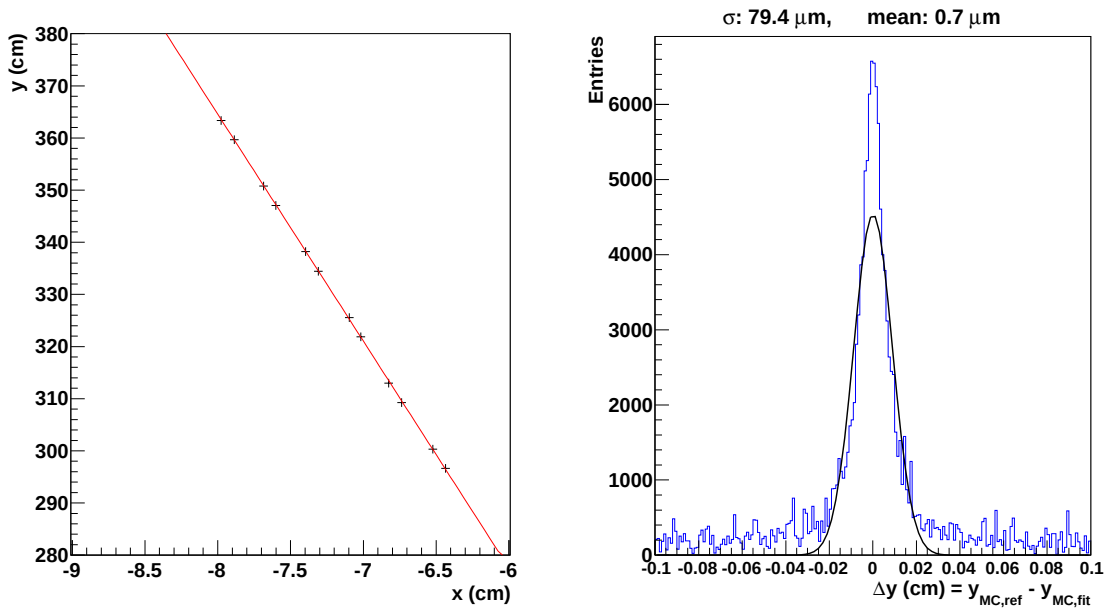

Figure B.3: *Left panel: fit through the 12 Monte Carlo references. Right panel: distribution of the residuals between the references and the fit. Though Monte Carlo information should be very precise, strong deviations can be observed. The fit possibly leads to erroneous results so that a direct line between two references is the better choice.*

Layer:	L0	L1	L2	L3	L4	L5
Deviation (μm) :	109	33	91	90	33	108

Table B.1: *Deviations between the Monte Carlo references and the straight line fit for single layers.*

C. Angular Resolution Plots

C.1 Angular Resolution before Tilted Pad Correction

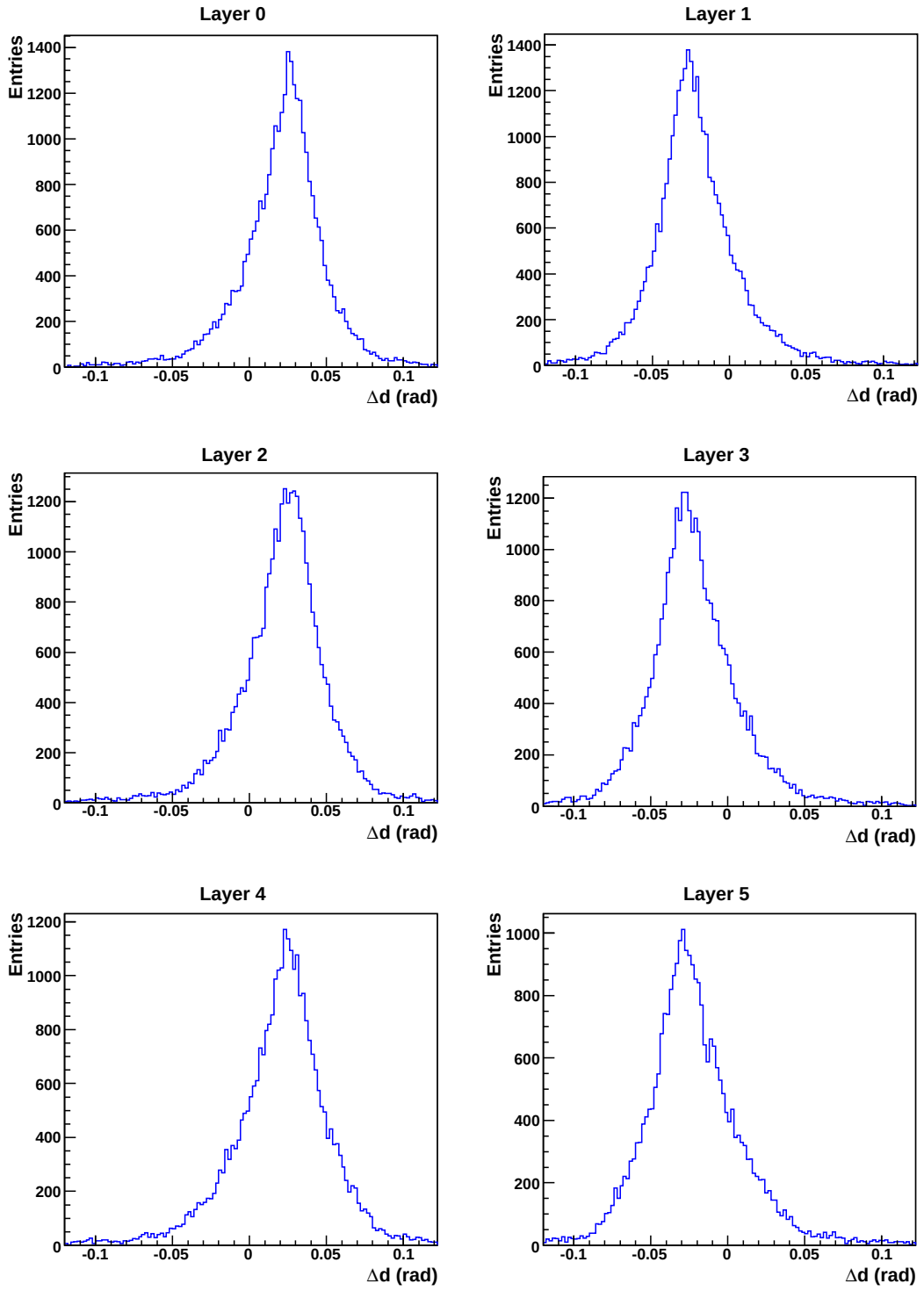

Figure C.1: *Residuals of Monte Carlo track and online tracklet slope before the correction of the tilted pads.*

C.2 Angular Resolution after Tilted Pad Correction

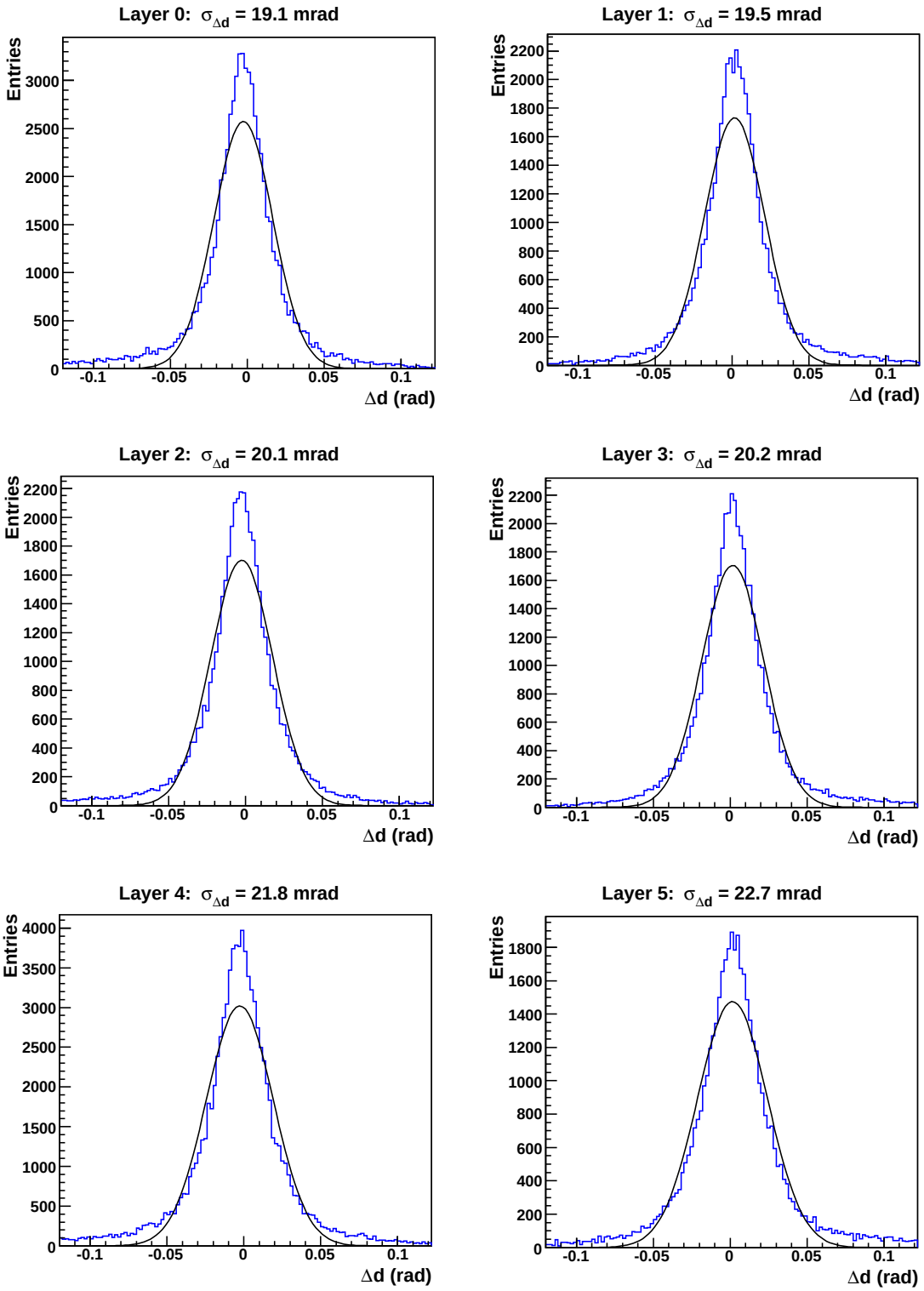

Figure C.2: *Residuals between Monte Carlo track and online tracklet slope after the correction of the tilted pads.*

C.3 Distribution of Residuals Plotted vs. the MC Angle

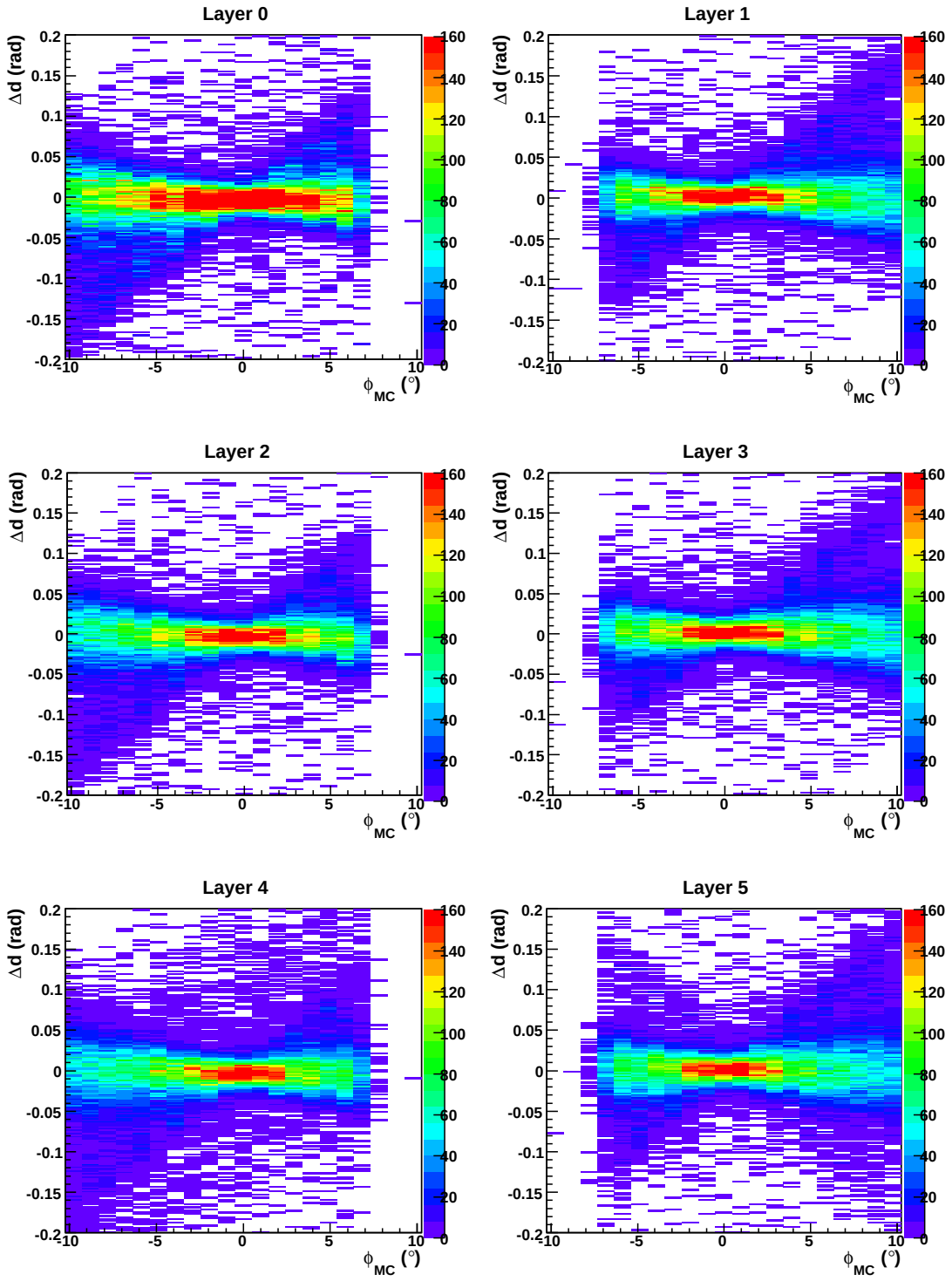

Figure C.3: *Residuals between Monte Carlo track and online tracklet slope after the correction of the tilted pads plotted vs. the Monte Carlo track angle ϕ. The shifting in opposite direction for consecutive layers occurs because of the tilted pad correction of the Monte Carlo track which was originally created for an angle interval of $10° \leq \phi \leq 10°$ (see section 7.3.1).*

Bibliography

[A+03] C. Adler et al. The Star Collaboration. *Phys. Rev. Lett.*, 90:082302, 2003.

[A+05] V. Angelov et al. *ALICE TRAP User Manual*. 2005.

[A+08a] K. Aamodt et al. *The ALICE Experiment at the CERN LHC*. The ALICE Collaboration, 2008.

[A+08b] C. Amsler et al. Particle Data Group. *Physics Letters* ***B667***, 1, 2008. `http://pdg.lbl.gov/` (updated for the 2010 edition).

[Adr] A. Adronic. *Transition Radiation Detector Study*. Gesellschaft für Schwerionenforschung, Darmstadt, Germany.

[Alb10] B. Albrecht. *Gain Calibration of ALICE TRD Modules Using Cosmic Ray Data*. Westfälische Wilhelms-Universität Münster, diploma thesis, 2010.

[ali09] *Official Hompage of the ALICE-TRD-Project*. `http://www-alice.gsi.de/trd/tdr/index.html`, September 2009.

[alp10] *Official Website of the Stanford Linear Acceleration Center*. `http://www-project.slac.stanford.edu/e158/running-unification.html`, January 2010.

[Ams07] C. Amsler. *Kern- und Teilchenphysik*. vdf Hochschulverlag AG an der ETH Zürich, 2007.

[Ang06] V. Angelov. Design and Performance of the ALICE TRD Front-end Electronics. *Nuclear Instruments and Methodes in Physics Research Section A*, 563:317–320, 2006.

[B+04] O. Brüning et al. LHC Design Report. *Reports - CERN*, Volume I, chapter 21, 2004.

[Bar06] T. Barnes. The XYZs of Charmonium at BES. *Int.J.Mod.Phys.*, A21:5583–5591, 2006.

[Bat07] B. Bathen. *Aufbau eines Triggers für Tests der ALICE-TRD-Supermodule mit kosmischer Strahlung*. Westfälische Wilhelms-Universität Münster, diploma thesis, 2007.

[BMS07] P. Braun-Munzinger and J. Stachel. The Quest for the Quark Gluon Plasma. *NATURE*, 448:302–309, July 2007.

[BRR08] W. Blum, W. Riegler, and L. Rolandi. *Particle Detection with Drift Chambers*. Springer, 4^{th} edition, 2008.

[cer09] *Official Hompage of CERN*. `http://www.cern.de/`, September 2009.

[dC03] J. de Cuveland. *Entwicklung der globalen Spurrekonstruktionseinheit für den ALICE-Übergangsstrahlungsdetektor am LHC (CERN)*. Fakultät für Physik und Astronomie Ruprecht-Karls-Universität Heidelberg, diploma thesis, 2003.

[E+05] D. Evans et al. The ALICE Central Trigger System. *Real Time Conference*, 14th:IEEE–NPSS, 2005.

[Ems10] D. Emschermann. *Construction and Performance of the ALICE Transition Radiation Detector*. The Combined Faculties for the Natural Sciences and for Mathematics of the Ruperto-Carola Universität of Heidelberg, Germany, dissertation, 2010.

[Gut02] M. Gutfleisch. *Digitales Frontend und Preprozessor im TRAP1 Chip des TRD Triggers für das ALICE Experiment am LHC (CERN)*. Fakultät für Physik und Astronomie Ruprecht-Karls-Universität Heidelberg, diploma thesis, 2002.

[Gut06] M. Gutfleisch. *Local Signal Processing of the ALICE Transition Radiation Detector at LHC (CERN)*. Naturwissenschaftlich-Mathematische Gesamtfakultät der Ruprecht-Karls-Universität Heidelberg, dissertation, 2006.

[HM96] J. W. Harris and B. Müller. The Search for the Quark Gluon Plasma. *Annu. Rev. Nucl. Part. Sci.*, 46:71–107, 1996.

[KL03] F. Karsch and E. Laermann. *Thermodynamics and in-Medium Hadron Properties from Lattice QCD*. Fakultät für Physik, Universität Bielefeld, 2003.

[Kle02] K. Kleinknecht. *Detektoren für Teichenstrahlung*. Teubner, Stuttgart, 3rd edition, 2002.

[Kle08] J. Klein. *Commissioning of and Preparations for Physics with the Transition Radiation Detector in A Large Ion Collider Experiment at CERN*. Fakultät für Physik und Astronomie Ruprecht-Karls-Universität Heidelberg, diploma thesis, 2008.

[Kle09] J. Klein. *Personal Communication*. 2009.

[lhc09] *LHC - The Guide*. CERN Communication Group / CERN Brochure, 2009. `http://cdsweb.cern.ch`.

[Lor03] Falko Lorenz. *Lineare Algebra I*. Spektrum Akademischer Verlag Heidelberg, 4^{th} edition, 2003.

[nob10] *Official Website of the Nobel Foundation*. `http://nobelprize.org/`, January 2010.

[P+09] B. Povh et al. *Teilchen und Kerne - Eine Einführung in die physikalischen Konzepte*. Springer Berlin Heidelberg, 8^{th} edition, 2009.

[rhi09] *Offical Hompage of RHIC at BNL*. `http://www.bnl.gov/rhic/`, September 2009.

[roo10] *Aliroot Class Index*. `http://aliceinfo.cern.ch/static/aliroot-new/html/roothtml/ClassIndex.html`, February 2010.

[RS09] K. Reygers and K. Schweda. *High-Energy Nuclear Collisions with ALICE at the LHC*. Lecture, Graduate Days Heidelberg, 2009. `http://gsfp.physi.uni-heidelberg.de/graddays/index.php?m=2&s=7`.

[S+06] P. Senger et al. The CBM Experiment at FAIR. *J. Phys.: Conf. Ser.*, 50:357–360, 2006.

[Sic09] E. Sicking. *Alignment of the ALICE TRD Modules Using Cosmic Ray Data.* Westfälische Wilhelms-Universität Münster, diploma thesis, 2009.

[SPR90] B. Sinha, S. Paland, and S. Raha. *Quark-Gluon Plasma.* Springer-Verlag, 1990.

[trd01] *ALICE Technical DesignReport of the Transition Radiation Detector.* 2001. `http://www-alice.gsi.de/trd/tdr/index.html`.

[Wes09] U. Westerhoff. *The FEE Server Control Engine of the ALICE-TRD.* Westfälische Wilhelms-Universität Münster, diploma thesis, 2009.

[Wul09] S. Wulff. *Position Resolution and Zero Suppression of the ALICE TRD.* Westfälische Wilhelms-Universität Münster, diploma thesis, 2009.

[WW06] C. Weinheimer and J. P. Wessels. *Skript zur Vorlesung Kern und Teilchenphysik I.* Institut für Kernphysik, Westfälische Wilhelms-Universität Münster, 2006.

[WW07] C. Weinheimer and J. P. Wessels. *Skript zur Vorlesung Kern und Teilchenphysik II.* Institut für Kernphysik, Westfälische Wilhelms-Universität Münster, 2007.

[YHM05] K. Yagi, T. Hatsuda, and Y. Miake. *Quark-Gluon Plasma - From Big Bang to Little Bang.* Cambridge University Press, 2005.

Danksagung

Das Gelingen dieser Arbeit wurde nur dadurch ermöglicht, dass ich große Unterstützung von vielen Seiten auf unterschiedlichste Art und Weise erfahren habe. Hiermit möchte ich mich dafür bedanken.

Zunächst gilt der Dank meiner Familie, denn insbesondere durch die finanzielle und moralische Unterstützung meiner Eltern Christine und August in den letzten fünf Jahren wurde dieses Studium erst ermöglicht. Des weiteren möchte ich mich bei meinem Bruder Stefan bedanken, der mir den Einstieg ins Studium durch viele Hilfestellungen erleichtert hat.

Für die Aufnahme in die Arbeitsgruppe und das interessante Thema meiner Diplomarbeit möchte ich mich bei Herrn Prof. Dr. Johannes P. Wessels bedanken. Es war ein großes Erlebnis, in den letzten zwei Jahren aktiv an einem Jahrhundertexperiment mitzuarbeiten und dabei das Glück zu haben, den erneuten Start des LHC im November 2009 'live' am CERN zu erleben. Des weiteren bedanke ich mich für die Möglichkeit der Teilnahme an interessanten Veranstaltungen wie der ALICE Week im Juni 2009 in Genf oder dem Besuch der Graduate School im Oktober 2009 in Heidelberg.

Für die exzellente Betreuung während meiner Arbeit möchte ich mich bei Dr. Thomas Dietel bedanken, der mir viele Hilfestellungen, insbesondere in physikalischen Fragen, gegeben hat.

Jochen Klein danke ich für die Bereitstellung des MCM Simulators, ohne den meine Diplomarbeit nicht realisierbar gewesen wäre, sowie für die ausdauernde und kompetente Beantwortung vieler Fragen per E-mail. Bei Dr. Matus Kalisky möchte ich mich für die stets freundliche Art bedanken mit der er meine zahlreichen Aliroot Probleme gelöst hat. Des weiteren möchte ich mich bei Uwe Westerhoff bedanken, der immer ein offenes Ohr bei computertechnischen Fragen hatte.

Für die kritischen Korrekturen und nützlichen Anregungen im Vorfeld der Abgabe möchte ich mich bei Dr. Thomas Dietel, Dr. Matus Kalisky, Dr. Christian Klein-Bösing, Dr. David Emschermann, Henriette Gatz, Björn Albrecht und ganz besonders bei meiner Mutter Christine, die es auf sich genommen hat, in die Welt der Quarks und Gluonen einzutauchen, ganz herzlich bedanken.

Für die schöne Zeit in den letzten zwei Jahren möchte ich mich bei meinen Bürokollegen Henriette Gatz und Björn Albrecht bedanken. Nicht nur die angenehme Atmosphäre in unserem gemütlichen Röntgenlabor, sondern auch die Harmonie beim manchmal an den Nerven zehrenden Supermodulbau, haben zum allgemeinen Erfolg beigetragen.

Für die angenehme Gesamtatmosphäre in der Arbeitsgruppe möchte ich allen Teilnehmern und Ehemaligen der AG noch einmal danken: Björn Albrecht, Jonas Anielski, Bastian Bathen, Dr. Christoph Baumann, Cyrano Bergmann, Dr. Thomas Dietel, Dr. David Emschermann, Henriette Gatz, Holger Gottschlag, Helge Grimm, Markus Heide, Norbert Heine, Dr. Matus Kalisky, Sebastian Klamor, Dr. Melanie Klein-Bösing, Dr. Christian Klein-Bösing, Stefan Korsten, Michael Kowalik, Friederike Poppenborg, Markus Rammler, PD Dr. Klaus Reygers, Baldo Sahlmüller, Eva Sicking, Anton Sperling, Wolfgang Verhoeven,

Don Vernekohl, Prof. Dr. Johannes P. Wessels, Uwe Westerhoff, Martin Wilde, Alexander Wilk und Svenja Wulff.

Zum Schluss möchte ich meiner Freundin Maike, die mich stets mit einem unglaublichen Maß an Ausdauer und Verständinis bei meiner Arbeit unterstützt sowie motiviert hat, einen besonderen Dank aussprechen.

Eigenständigkeitserklärung

Ich versichere, diese Arbeit selbständig verfasst und keine anderen als die angegebenen Hilfsmittel und Quellen benutzt zu haben.

Münster, 17. Februar 2010

Matthias Walter